

AD720386

Semi-Annual Technical Report No. 2

(for period Aug. 1, 1970 to Feb. 1, 1971)

Title: Steerable Volume and Surface Spin Waves
in Ferrimagnetic Films

Contract No.: DAHCL5 70 C 0190
ARPA Order No.: 1512
Program Code No.: D10

Name of Contractor: Massachusetts Institute of Technology
Cambridge, Mass. 02139

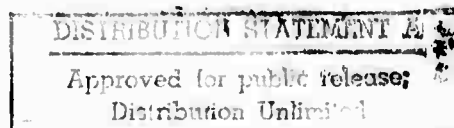
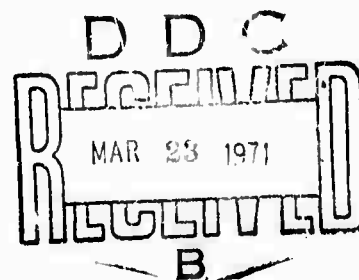
Principal Investigator: F.R. Morgenthau
(617) 864-6900 Ext. 4623

Effective Date of Contract: Feb. 2, 1970
Contract Expiration Date: Feb. 1, 1973

Total Amount of Contract: \$420,000.
through Feb. 1, 1973

Funds Allotted
through Feb. 1, 1971 \$140,000.

Sponsored by
Advanced Research Projects Agency
ARPA Order No. 1512



Reproduced by
NATIONAL TECHNICAL
INFORMATION SERVICE
Springfield, Va. 22151

183

**BEST
AVAILABLE COPY**

BLANK PAGE

28808500

The work reported in this document was made possible, in part, through support extended the Massachusetts Institute of Technology by the Advanced Research Projects Agency. The initial phase of the research was conducted under Contract SD-90; the final phase under Contract DAHC 15-70-C-0190.

ACCESSION FOR	
CFSTI	WHITE SECTION <input checked="" type="checkbox"/>
DOC	BUFF SECTION <input type="checkbox"/>
UNANNOUNCED	<input type="checkbox"/>
JUSTIFICATION	
BY	
DISTRIBUTION/AVAILABILITY CODES	
DIST.	AVAIL. and/or SPECIAL
A	

ABSTRACT

This report describes in detail the technical progress made in studies of strong infrared light scattering from coherent spin waves during the second six months of a three year interdisciplinary research program titled: "Steerable Volume and Surface Spin Waves in Ferromagnetic Films". One major goal of the program is the growth of yttrium-iron garnet (YIG), single crystals of high quality in both thin film and bulk form. Another is the development of novel techniques for controlling and studying energy propagation characteristics of volume and surface spin waves. One promising technique for accomplishing the latter involves the use of optical techniques to probe the dynamics of spin wave propagation. Since YIG is opaque to visible light but transparent in the infrared, this form of radiation has been employed in these experiments.

Coherent light scattering from coherent microwave spin waves in yttrium iron garnet (YIG) is studied theoretically and experimentally. The method is then utilized, in conjunction with standard microwave techniques, to probe the propagation of spin waves and magnetoelastic waves, in spatially-and/or-temporally-varying magnetic fields.

The dispersion of magnetoelastic waves propagating parallel to saturation magnetization when the latter is in an arbitrary crystallographic direction, first presented by Morgenthaler, is rederived. For this important case, spin wave defocussing is reduced and, when properly employed, allows variable delay of magnetically injected spin/longitudinal elastic waves, and conversion from longitudinal elastic waves to spin waves in spatially varying fields to be studied. Frequency shifts, and pulse compression of longitudinal elastic/spin waves subjected to

pulsed magnetic fields are also reported, as are some preliminary experiments on the spatial conversion of shear/longitudinal elastic waves via spin wave coupling.

We also report the first direct observation of strong Bragg scattered infrared light (1150 nm wavelength) from coherent microwave spin waves. The latter were generated in YIG through efficient spatial conversion of injected longitudinal elastic waves. The maximum scattered light intensity is found to be at least five times stronger than that of the longitudinal elastic waves of comparable power. In contrast to elastic wave scattering, spin wave light scattering is unique in that the diffracted light intensity is observed to depend on the incident light polarization and whether the diffracted light is upshifted or downshifted in frequency. These characteristics are in complete agreement with a revised theory that is found to be necessary after a critical review of previous work. The revision is shown to be capable of interpreting adequately not only our experiments but also observations that previous authors have reported as "anomalous."

I INTRODUCTION

The Microwave and Quantum Magnetism Group and the Crystal Physics Laboratory, both within the M.I.T. Center for Materials Science and Engineering, have undertaken a three year interdisciplinary program in the area of "microwave magneto-ultrasonics" aimed at further developing several novel concepts which may lead to new and/or improved solid state devices employing electromagnetic/spin/elastic wave coupling. Device possibilities include multi-tapped delay lines, magnetoelastic beam switches and pulse compression filters. In particular, the research program will concentrate on the growth and exploitation of improved single crystal yttrium iron garnet substrates in which volume and surface spin wave propagating at microwave frequencies can be magnetically steered and/or otherwise controlled.

In order to produce crystals of yttrium iron garnet of the quality needed for the research envisioned in this program, two major constraints must be dealt with. First, the crystals must be of the necessary high quality to avoid introducing extraneous effects due to grain boundaries and strain inhomogeneities. The chemical purity is of major importance since rare earth impurities drastically increase spin wave relaxation rates. Second, the growth technique should permit ready fabrication of the types of structures desired, such as multi-layer configurations and thin slabs. Consequently, both chemical vapor deposition (CVD) techniques and top seeded solution (TSS) growth appear attractive and both will be employed throughout the entire contract period. Thin films and bulk crystal substrates will be evaluated optically, magnetically and acoustically for purity, homogeneity and low losses. Promising specimens

will be used for magnetostatic wave and exchange dominated spin wave propagation experiments at microwave frequencies.

A surface spin wave propagating parallel to an air-crystal boundary of a thin film has its energy largely confined within some characteristic distance that under certain conditions should be magnetically controllable. In one instance causing the energy to be closely confined to the surface and in another allowing it to spread out and fill the entire film. Volume spin waves are also subject to magnetic control. For example, beam steering is possible due to dipole-dipole interactions that in turn can be influenced through directional changes in the magnetizing field.

A high power (50 mw) He-Ne laser operating continuously at 1.15μ has been obtained for use in producing Bragg scattering from elastic and spin-elastic microwave packets within YIG crystals. This high resolution system which is now operational forms the basis for studies of spin-elastic conversion in spatial and/or temporal gradients of magnetic field.

The doctoral thesis of Benedict Hu has been completed and forms the basis of this report.

Dr. A. Linz has been assigned responsibility for overseeing the top-seeded solution crystal growth and chemical vapor deposition program, Professor D.J. Epstein for crystal evaluation with respect to magnetic properties and Professor F.R. Morgenthaler for microwave spin wave propagation studies; as principal investigator the latter has overall responsibility for coordinating the various phases of the research.

STUDIES OF MAGNETOSTATIC WAVES AND MAGNETOELASTIC WAVES
IN YIG USING OPTICAL PROBING AND MICROWAVE TECHNIQUES

by

Hung-Liang Hu

The material which follows is identical in content to a thesis submitted to the Department of Electrical Engineering, Massachusetts Institute of Technology, on January 29, 1971, in partial fulfillment of the requirements for the degree of Doctor of Philosophy in Electrical Engineering. This thesis is also available as Microwave and Quantum Magnetism Group Technical Report No. 25, February, 1971.

TABLE OF CONTENTS

	Page
LIST OF SYMBOLS	6
LIST OF FIGURES	14
INTRODUCTION	18
CHAPTER I SMALL SIGNAL EQUATIONS OF MOTION OF A MAGNETOELASTIC FERROMAGNET	22
1.1 Small Signal Equations of Motion	22
1.2 Small Signal Power Energy Conservation Theorem	25
CHAPTER II PROPAGATION OF Z-DIRECTED MAGNETOELASTIC WAVES IN A GENERAL CRYSTALLOGRAPHIC DIRECTION	28
2.1 The Euler Angles	28
2.2 Eigenvalues and Eigenmodes of Spin Waves Propagating Along an Arbitrary Crystallographic Direction	33
2.3 Dispersion of Z-Directed Magnetoelastic Waves in an Elastically Isotropic but Magnetoelastic Anisotropic "Cubic" Medium	37
CHAPTER III EXPERIMENTAL RESULTS OF Z-DIRECTED MAGNETOELASTIC WAVES USING MICROWAVE TECHNIQUES	48
3.1 Experimental Setup	49
3.2 Experiments with Spin Wave Injections	51
3.3 Experiments with Acoustically Injected Longitudinal Elastic/Spin Waves	62
3.4 Preliminary Results on Longitudinal/Shear Elastic Conversion via Spin Waves in Spatially Varying Fields	76
CHAPTER IV THEORY OF LIGHT DIFFRACTION FROM COHERENT ELASTIC AND SPIN WAVES	83
4.1 Introduction	83
4.2 The Macroscopic Theory of Light Diffraction	85

	Page
4.3 Characteristics of Light Diffraction from Coherent Elastic Waves	95
4.4 Characteristics of Light Diffraction from Coherent Spin Waves	105
CHAPTER V EXPERIMENTAL RESULTS OF LIGHT DIFFRACTION FROM COHERENT ELASTIC AND/OR SPIN WAVES IN YIG	113
5.1 Setup for Light Diffraction Experiments	114
5.2 Infrared Bragg Scattering from Shear Elastic/Spin Waves	122
5.3 Strong Infrared Bragg Scattering from Coherent Spin Waves	132
5.4 Measurements of Temporal Longitudinal Elastic/Spin Wave Conversion Efficiencies	143
Appendix I Effective Anisotropy Fields and Small Anisotropy Tensor N_{an} for Cubic Crystals	148
Appendix II The First Order Magnetoelastic Constants for an Arbitrarily Oriented Coordinate System in Cubic Crystals	152
Appendix III Dielectric Tensor of a "Cubic" Magnetic Medium	163
REFERENCES	168
BIOGRAPHICAL NOTE	174

BLANK PAGE

TABLE OF CONTENTS

	Page
ABSTRACT	2
ACKNOWLEDGEMENTS	3
TABLE OF CONTENTS	4
LIST OF SYMBOLS	6
LIST OF FIGURES	14
INTRODUCTION	18
CHAPTER I SMALL SIGNAL EQUATIONS OF MOTION OF A MAGNETOELASTIC FERROMAGNET	22
1.1 Small Signal Equations of Motion	22
1.2 Small Signal Power Energy Conservation Theorem	25
CHAPTER II PROPAGATION OF Z-DIRECTED MAGNETO- ELASTIC WAVES IN A GENERAL CRYSTALLO- GRAPHIC DIRECTION	28
2.1 The Euler Angles	28
2.2 Eigenvalues and Eigenmodes of Spin Waves Propagating Along an Arbitrary Crystallo- graphic Direction	33
2.3 Dispersion of Z-Directed Magnetoelastic Waves in an Elastically Isotropic but Magnetoelastic Anisotropic "Cubic" Medium	37
CHAPTER III EXPERIMENTAL RESULTS OF Z-DIRECTED MAGNETOELASTIC WAVES USING MICROWAVE TECHNIQUES	48
3.1 Experimental Setup	49
3.2 Experiments with Spin Wave Injections	51
3.3 Experiments with Acoustically Injected Longitudinal Elastic/Spin Waves	62
3.4 Preliminary Results on Longitudinal/Shear Elastic Conversion via Spin Waves in Spatially Varying Fields	76

	Page
CHAPTER IV THEORY OF LIGHT DIFFRACTION FROM COHERENT ELASTIC AND SPIN WAVES . . .	83
4.1 Introduction 	83
4.2 The Macroscopic Theory of Light Diffraction 	85
4.3 Characteristics of Light Diffraction from Coherent Elastic Waves 	95
4.4 Characteristics of Light Diffraction from Coherent Spin Waves 	105
CHAPTER V EXPERIMENTAL RESULTS OF LIGHT DIFFRACTION FROM COHERENT ELASTIC AND/OR SPIN WAVES IN YIG 	113
5.1 Setup for Light Diffraction Experiments	114
5.2 Infrared Bragg Scattering from Shear Elastic/Spin Waves 	122
5.3 Strong Infrared Bragg Scattering from Coherent Spin Waves 	132
5.4 Measurements of Temporal Longitudinal Elastic/Spin Wave Conversion Efficiencies	143
Appendix I Effective Anisotropy Fields and Small Anisotropy Tensor N^{an} for Cubic Crystals	148
Appendix II The First Order Magnetoelastic Constants for an Arbitrarily Oriented Coordinate System in Cubic Crystals 	152
Appendix III Dielectric Tensor of a "Cubic" Magnetic Medium 	163
REFERENCES 	168
BIOGRAPHICAL NOTE 	174

LIST OF SYMBOLS

(other ad hoc notation is explained in the text where it occurs)

Symbol	Definition	Place of symbol or first occurrence
a	= half length of major or minor axis of the elliptical spin wave polarization	Eqs. (2.16) and (2.17)
a	= height of the light beam cross section	Fig. 4.2 and Eq. (4.14)
A	= $\omega_3^i + (N_{11} + \frac{k_1^2}{k^2}) \omega_M + \lambda_e k^2 \omega_M$	Eq. (2.11b)
b	= half length of major or minor axis of the elliptical spin wave polarization	Eqs. (2.16) and (2.17)
b_{fijk}	= first order (in strain) magnetoelastic constants	Eq. (A2.1)
b_{ijk}	= small signal first order magnetoelastic constants	Eqs. (1.3d) and (A2.8)
b_1, b_2	= non-zero first order magnetoelastic constants of cubic crystals	Eq. (A2.6)
b_ℓ, b_s	= z-directed longitudinal and shear magnetoelastic frequency splittings, respectively	Eq. (2.37)
b_ℓ^2, b_s^2	= z-directed longitudinal and shear magnetoelastic couplings, respectively	Eq. (2.28)
B_{ij}	= dielectric impermeability tensor	Eq. (4.22)
δB_{ij}	= small change of dielectric impermeability	Eq. (4.23)
B	= $\omega_3^i + (N_{22} + \frac{k_2^2}{k^2}) \omega_M + \lambda_e k^2 \omega_M$	Eq. (2.11b)
c_{ijkl}	= second order elastic constants	Eq. (1.4)
c_{11}, c_{12}, c_{44}	= non-zero second order elastic constants of cubic crystals	Eq. (1.4)
c	= velocity of light in free space	Eq. (4.1)

Symbol	Definition	Place of symbol or first occurrence
c	= width of the light beam cross section	Fig. 4.2 and Eq. (4.14)
c	= a proportionality constant	Eq. (4.31b)
C	= $\omega_M (N_{12} + k_1 k_2 / k^2)$	Eq. (2.11d)
D_0	= mass density of the medium	Eq. (1.4)
D	= diameter of a YIG rod	Eq. (3.1a)
\vec{e}	= rf electric field vector	Eq. (1.1)
\vec{E}	= optical electric field vector	Eq. (4.1)
\vec{E}^i	= electric field of the incident light	Eq. (4.7a)
\vec{E}_0^i, \vec{E}_0^d	= electric fields of the incident and diffracted light, respectively	Eq. (4.11) and Eq. (4.30).
$E(\vec{r}')$	= profile of the light beam	Eq. (4.11)
E_v^i, E_H^i	= vertically polarized (along x-axis) and horizontally polarized (along z-axis) electric fields of the incident light, respectively	Fig. 4.2 and Eq. (4.30)
$E_{v\pm}^d, E_{H\pm}^d$	= vertically polarized (along x-axis) and horizontally polarized (along z-axis) electric fields of the diffracted light, respectively; the subscript (\pm) denotes whether the diffracted light is upshifted (+) or downshifted (-) in frequency with respect to the incident light	Fig. 4.2 and Eq. (4.30).
\vec{f}'	= magnetoelastic force density (related to \vec{h}')	Eq. (1.4)
\vec{f}^{me}	= small signal magnetoelastic force density	Eq. (1.5)
f	= $\frac{\omega}{2\pi}$ frequency	
$f, f_{k\mu}$	= "linear" magneto optic coefficients	Eqs. (4.40c) and (A3.9)
g_{ijkl}, g_{mn}	= "quadratic" magneto optic coefficients	Eqs. (4.40b) and (A3.13)

Symbol	Definition	Place of symbol or first occurrence
\vec{h}'	= small signal effective magnetic field	Eq. (1.2)
$\vec{h}^{an}, \vec{h}^{ex}, \vec{h}^{me}$	= small signal effective magnetic anisotropy, exchange and magnetoelastic fields, respectively	Eq. (1.2)
\vec{h}	= small signal Maxwellian magnetic field	Eq. (1.1a)
\vec{H}	= optical magnetic field vector	Eq. (4.1)
$\vec{H}_i(\vec{r}), H_i(z)$	= internal bias magnetic fields	Eq. (1.3a)
\vec{H}_o, H_o	= external bias magnetic fields	Eq. (1.3a)
$H^{dem} = -N_M M$	= demagnetizing field along the static magnetization direction	Eq. (1.3a)
H_3^{an}, H_M^{an}	= effective static anisotropy fields along the static magnetization direction (z-axis or x_3 -axis)	Eqs. (1.3a) and (A1.5c)
$H_c^\ell (H_c^s)$	= the value of the applied field for which a longitudinal (shear) magnetoelastic crossover point is in the mid-point of the long axis of an axially magnetized YIG rod or bar	Section 3.3a
$H'(z)$	= spatial field gradient at coordinate z	Eq. (3.3)
$H_{crit}^{\ell}, H_{crit}^s$	= critical spatial field gradients for longitudinal and shear magnetoelastic coupling, respectively	Eq. (3.2)
\dot{H}_{crit}^ℓ	= critical temporal field gradient for longitudinal magnetoelastic coupling	Fig. 5.13
HT	= height of a YIG bar	Eq. (3.1b)
\vec{j}^{eff}	= effective current density	Eq. (4.2b)
$\vec{k}(k)$	= wavevector (wavenumber) of the elastic waves, spin waves, or elastic/spin waves	Eqs. (2.7) and (2.21)
$\vec{k}_L(k_L)$	= wavevector (wavenumber) of the incident light	Eq. (4.7)

Symbol	Definition	Place of symbol or first occurrence
$\vec{k}_L' (k_L')$	= wavevector (wavenumber) of the diffracted light	Eqs. (4.12) and (4.13)
K_1, K_2	= magnetic anisotropy constants of cubic crystals	Eqs. (A1.1) and (2.15)
L	= length of a YIG rod or bar	Eq. (3.1a)
$L_{\text{cros}}(S_{\text{cros}})$	longitudinal (shear) magnetoelastic crossover point	Fig. 3.2
$\vec{m}(\vec{r}, t)$	= small signal magnetization vector ($\vec{m}, \vec{M} \approx 0$)	Eq. (1.1c)
m	= small signal magnetization amplitude	Eq. (4.41)
M	= saturation magnetization	Eqs. (1.2) and (4.1)
n	= index of refraction in an isotropic medium	Section 4.1 and Eq. (4.20)
n_i, n_d	= index of refraction pertaining to the incident and diffracted light polarization, respectively	Eqs. (4.6) and (4.7)
N_{ij}^{an}	= small signal anisotropy tensor	Eqs. (1.3b) and (A1.6)
$N_{ij}'^{\text{an}}$	= small signal effective anisotropy tensor	Eq. (A1.9)
P_a	= acoustic power density	Eq. (4.36)
P_A	= power of a circular acoustic beam	Eq. (4.37)
\vec{P}	= polarization	Eq. (4.1)
\vec{P}^{eff}	= effective polarization	Eq. (4.3b)
P_{ijkl}, P_{mn}	= photoelastic constants	Eqs. (4.23) and (4.24)
P_{eff}	= effective photoelastic constants	Eq. (4.36)
\vec{r}	= position vector from an origin to the observation point	Eq. (4.6) and Fig. 4.1

Symbol	Definition	Place of symbol or first occurrence
\vec{r}'	= position vector from an origin to the illuminated volume	Eq. (4.6) and Fig. 4.1
$\vec{i}_r, \vec{i}_{r'}$ $\vec{i}_{ \vec{r}-\vec{r}' }$	= unit vectors	Fig. 4.1
\vec{S}_{total}	= small signal total Poynting vector	Eq. (1.10)
$\vec{S}_{elas}, \vec{S}^m, \vec{S}^{me}$	= small signal Poynting vectors of elastic, magnetic and magnetoelastic waves, respectively	Eqs. (1.11) and (1.13)
S_{kl}, S_n	= symmetrical strain tensor	Eqs. (4.23), (4.24) and (A2.1)
$S_{cros}(L_{cros})$	shear (longitudinal) magnetoelastic crossover point	Fig. 3.2
t	= time	Eqs. (1.1) and (4.1)
t'	= retarded time	Eq. (4.6)
\vec{T}, \vec{T}^t	= transformation matrix and its transpose	Eqs. (2.4) and (2.2)
T_{ijkl}	= $2i T_{EL} + j T_{SL} + 2k T_{ES} + l T_{SS}$	Eq. (3.4)
T_{EL}, T_{ES}	= time taken by a longitudinal and shear elastic wave packet to travel the length of a YIG rod	Eq. (3.4)
T_{SL}, T_{SS}	= round trip time of flight of a longitudinal and shear elastic/spin wave from and back to the turning point	Eq. (3.4)
T	= turning point	Fig. 3.2
v_g	= group velocity	Eq. (3.5)
v_k	= group velocity of spin waves	Fig. 2.5
v_p	= group velocity of (longitudinal or shear) elastic waves	Eq. (3.3)
v_l, v_s	= group velocities of longitudinal and shear elastic waves, respectively	Eq. (2.26) and Fig. 2.5

Symbol	Definition	Place of symbol or first occurrence
w', w	= width and effective width of the acoustic or spin wave in the plane of incidence, respectively	Eqs. (4.14) and (4.21)
WD	= width of a YIG bar	Eq. (3.1b)
w_{total}	= small signal total energy density	Eq. (1.12)
$w_{an}, w_m, w_{me}, w_{elas}$	= small signal anisotropy, magnetic, magnetoelastic and elastic energy density, respectively	Eqs. (1.3b), (1.6), (1.8) and (1.7)
W_{an}, W_{me}	= anisotropy and magnetoelastic energy density, respectively	Eqs. (A1.1) and (A2.1)
$\vec{x}, (x_1, x_2, x_3), (x, y, z)$	= a coordinate system transformed from the "cubic-edge" coordinate system through the Euler Angles (φ, θ, ψ)	Eq. (2.1) and Fig. 2.1
$z_{cr}, z_{cr}^l, z_{cr}^s$	= coordinate of either longitudinal or shear magnetoelastic crossover point; coordinates of longitudinal and shear magnetoelastic crossover points, respectively;	Eq. (3.6) and Fig. 3.2
z_{tp}	= coordinate of the turning point	Eq. (3.3)
$\alpha_x (= \frac{M_x}{M}), \alpha_y (= \frac{M_y}{M}), \alpha_z (= \frac{M_z}{M})$	= the direction cosines of the magnetization	Eqs. (4.40b), (4.40c) and (4.41)
α	= spin wave loss in db/ μ sec	Eqs. (3.7) and (3.11)
α	= the angle between the diffracted light beam and the wavefronts of elastic or spin waves	Eq. (4.15) and Fig. 4.2
β	= the angle between the diffracted light beam and the plane of incidence (y-z plane)	Eq. (4.15)
γ	= gyromagnetic ratio	Eq. (1.2)

Symbol	Definition	Place of symbol or first occurrence
$\delta\epsilon_{ij}^{\text{eff}}$ ($=4\pi\delta\chi_{ij}^{\text{eff}}$)	= small change of the effective dielectric tensor	Eq. (4.12b)
$\delta\chi_{ij}^{\text{eff}}$ ($=\frac{\delta\epsilon_{ij}^{\text{eff}}}{4\pi}$)	= small change of the effective dielectric susceptibility tensor	Eq. (4.8)
$\delta\epsilon_{ij}$	= an abbreviated $\delta\epsilon_{ij}^{\text{eff}}$	Eq. (4.21)
Δg	= $g_{11} - g_{12} - 2g_{44}$	Eq. (4.46b)
ϵ	= permittivity	Eq. (1.1)
ϵ	= dielectric constant	Eq. (4.1)
$\vec{\epsilon}^{\text{eff}}$	= effective dielectric tensor	Eq. (4.3c)
$\vec{\epsilon}$	= an abbreviated $\vec{\epsilon}^{\text{eff}}$	Eq. (4.22b)
η	= spatial or temporal magnon-phonon conversion efficiency	Eq. (3.6)
η^{ℓ}	= spatial magnon-longitudinal phonon conversion efficiency	Eq. (3.7)
$\eta_{S\rightarrow L}$	= the efficiency of conversion from shear elastic waves to longitudinal elastic waves via spin wave coupling	Eq. (3.11)
θ_B	= incidence angle or Bragg angle	Eqs. (4.15), (4.20) and Fig. 4.2
λ_e	= exchange constant	Eq. (1.3c)
λ	= wavelength of light in free space	Section 4.1
Λ	= wavelength of spin or elastic waves	Section 4.1 and Eq. (4.19)
μ_0	= free space permeability	Eq. (1.1)
μ	= permeability of the medium	Section 4.2

Symbol	Definition	Place of symbol or first occurrence
$\vec{\xi}, (\xi, \eta, \zeta)$	= the coordinate system in which the axes are along the cubic edges of cubic crystals	Eq. (2.1) and Fig. 2.1
$\vec{\rho}$	= small signal elastic displacement vector	Eq. (1.4)
(φ, θ, ψ)	= the Euler Angles	Eq. (2.2) and Fig. 2.1
$\vec{\chi}^{\text{eff}}$	= effective dielectric susceptibility tensor	Eq. (4.3a)
$\omega = 2\pi f$	= microwave angular frequency	Eq. (2.21)
ω_k	= spin wave angular frequency	Eq. (2.7)
ω_M	= $-\gamma\mu_0 M$	Eq. (1.2)
ω_3^i	= $-\gamma\mu_0 H_i$	Eq. (2.10a)
ω_1	= $A \cos^2 \psi + B \sin^2 \psi - C \sin^2 2\psi$	Eq. (2.18)
ω_2	= $A \cos^2 \psi - B \sin^2 \psi + C \sin^2 2\psi$	Eq. (2.18)
ω_ℓ, ω_s	= angular frequencies of longitudinal and shear elastic waves, respectively.	Eq. (2.26)
ω_L, ω_L'	= angular frequencies of the incident and diffracted light, respectively	Eqs. (4.7) and (4.13)

LIST OF FIGURES

Fig. No.		Page
2.1	The Euler Angles	31
2.2	Dispersion diagram for spin waves.	36
2.3	Longitudinal and shear magnetoelastic couplings of z-directed waves in a {100} plane.	43
2.4	Longitudinal and shear magnetoelastic couplings of z-directed waves in a {110} plane.	45
2.5	Dispersion diagram for z-directed magnetoelastic waves; the spin/longitudinal and spin/shear wave splittings (b_l and b_s) are shown very much exaggerated. The quantities v_l , v_s and v_k are, respectively, group velocities of longitudinal elastic, shear elastic and spin waves; the branch numbers are referred to in the text.	47
3.1	Block diagram of L-band microwave circuitry.	50
3.2	Internal field profiles of a YIG rod and a YIG bar, showing turning points (T) and crossover points (L_{cros} and S_{cros}). The distances between these points are very much exaggerated.	52
3.3	Measured time delay of the first longitudinal (L01) and shear (S01) echoes versus dc magnetic bias fields at 1.5 GHz.	55
3.4	Magnetoelastic echoes affected by a pulsed magnetic bias field. The first pulse in each lower trace is due to leakage; the second and third are, respectively, the longitudinal (L01) and shear (S01) magnetoelastic echoes (time scale 1 μ sec/cm). A full explanation of cases (a) - (e) is given in the text.	57
3.5	A typical magnetoelastic echo pattern observed with one-port fine wire excitation. The first pulse in the trace is due to leakage; the other two pulses are due to the longitudinal and shear magnetoelastic coupling (time scale 1 μ sec/cm). A full explanation is given in the text.	59
3.6	An echo pattern of Fig. 3.5, reconstructed from theoretical considerations.	61
3.7	Delay of elastically injected longitudinal elastic/spin wave packet and group velocity at the bar center as a function of applied magnetic field for a "22.50" YIG bar which measures 4 mm x 4 mm x 12 mm.	64

Fig. No.		Page
3.8	The distortion of a longitudinal elastic/spin wave packet, which is excited and detected by a ZnO transducer, as a function of external applied magnetic field (time scale $0.1 \mu\text{sec/cm}$).	65
3.9	Magnetoelastic (magnon-phonon) conversion efficiency versus inverse spatial magnetic field gradient obtained with spin wave injection.	68
3.10	Magnetoelastic (magnon-phonon) conversion efficiency versus inverse spatial magnetic field gradient obtained with acoustic wave injection.	71
3.11	Pulse compression of longitudinal elastic/spin waves subjected to pulsed magnetic fields. The static magnetic field here is high enough so that there are crossover points inside the YIG bar (i. e., $H_0 > H_c$). Horizontal sweeps are from left to right with scale $0.5 \mu\text{sec/cm}$ (frequency 1.5 GHz).	74
3.12	Pulse compression of longitudinal elastic/spin waves subjected to pulsed magnetic fields, when $H_0 < H_c$. Horizontal sweeps are from left to right with scale $0.5 \mu\text{sec/cm}$ (frequency 1.5 GHz).	75
3.13	Arrangement used to observe spatial conversion from shear elastic waves to longitudinal elastic waves via spin wave coupling.	78
3.14	Total delay time (τ_t) and spatial conversion efficiency (η_{S+L}) from shear elastic waves to longitudinal elastic waves via spin wave coupling as a function of field gradient at the longitudinal crossover point.	79
3.15	Oscillograms showing the spatial conversion from shear elastic waves to longitudinal elastic waves via spin wave coupling. The horizontal traces are from left to right (time scale $1 \mu\text{sec/cm}$).	80
4.1	Radiation from an illuminated volume.	98
4.2	Geometry of light diffraction.	93
4.3	Bragg condition for $\vec{k}'_L = \vec{k}_L + \vec{k}$	93
4.4	Geometry of the photoelastic interaction.	100
4.5	Geometry of the photoelastic interaction and orientation of the long axis (z-axis) of the sample.	102

Fig. No.		Page
4.6	The geometry of light diffraction from spin waves; the internal field profile H_i of the bar is also indicated.	107
4.7	Light diffraction from coherent magnetostatic waves.	110
5.1a	Block diagram of the optical experimental setup.	115
5.1b	Optical experimental setup.	120
5.2	Diffacted light pulses from a 1.3 GHz shear elastic wave pulse propagating along a $\langle 100 \rangle$ direction and polarized along a $\langle 110 \rangle$ direction in YIG. The graph was recorded with the signal from the PAR boxcar integrator. The insert is the scope trace.	124
5.3	Diffacted light intensity (in arbitrary units) of shear elastic/spin waves as a function of external magnetic field; the light beam is incident near the mid-point of the long axis. The insert is the scope trace swept from right to left when $H_0 \cong H_C$, indicating small group velocity dispersion. A full explanation is given in the text.	126
5.4	Diffacted light intensity (in arbitrary units) of shear elastic/spin waves as a function of external magnetic field; the light beam is incident near the mid-point of the long axis. The insert is the scope trace swept from right to left when $H_0 \cong H_C$, indicating the peak diffacted light intensity (marked "spin" on the curve) and a slight decrease of the group velocity.	128
5.5	Diffacted light intensity of shear elastic/spin waves as a function of external magnetic fields, illustrating the effect of homogeneity of the applied field.	130
5.6	Diffacted light intensity of shear elastic/spin waves as a function of external magnetic fields, illustrating the effect of homogeneity of the applied field.	131
5.7	Diffacted light pulses from a 1.5 GHz longitudinal elastic wave pulse propagating along a "22.50" YIG bar. The graph was recorded with the signals from the PAR boxcar integrator. The insert is the scope trace.	135

Fig. No.		Page
5.8	Scope traces indicated with signals from the microwave circuitry and the photomultiplier as a function of external magnetic field. The upper and lower traces are synchronized; the upper traces are from the microwave receiver and the lower traces are from the photomultiplier. The diffracted light signal is polarized at $\pi/2$ with respect to the incident light (E_H^i, E_V^d). In (a), the upper trace indicates the first leakage pulse, and two longitudinal elastic echoes whose amplitudes saturate the receiver. In (b), the longitudinal echoes are strongly attenuated due to the magnetoelastic coupling. In (c), the longitudinal echoes are still attenuated; the lower trace now indicates a <u>strong</u> diffracted light signal from coherent spin waves (compare the diffracted light pulse with that in Fig. 5.7).	138
5.9	Scattered light intensity (in arbitrary units) of spin waves and longitudinal elastic waves as a function of external magnetic field. The insert is the oscilloscope trace showing the peak intensity of the diffracted light pulse (compare with the diffracted light pulse of the scope trace in Fig. 5.7).	140
5.10	Diffracted light intensity as a function of input microwave power.	141
5.11	Diffracted light intensity (E_V^i, E_{H+}^d) from coherent spin waves as a function of the timing of the pulsed bias field; the spin waves are generated through temporal conversion from longitudinal elastic waves (time scale 0.5 μ sec/cm). A full explanation is given in the text.	144
5.12	(a) diffracted light pulses from longitudinal elastic waves (E_V^i, E_V^d) (time scale 0.5 μ sec/cm). (b) to (f) - an expanded version of Fig. 5.11 (E_V^i, E_{H+}^d) (time scale 0.2 μ sec/cm).	146
5.13	Magnetoelastic (phonon \rightarrow magnon) conversion efficiency versus inverse temporal field gradient. \dot{H}_{crit}^l	147

INTRODUCTION

In the recent past, the propagation of magnetoelastic waves in low loss, saturated ferrimagnetic crystals has been a subject of great interest because of their potential uses in compact microwave signal processing devices. For example, frequency filtering, variable delay, gating, pulse compression and expansion are all possible operations. However, their practical development requires additional information about the spin wave channel of power flow, together with its coupling to the well understood elastic wave channel. In 1961, Schlömann⁸³ predicted that spin waves could be excited in non-uniform magnetic bias fields. Shortly afterwards, Eshbach⁸⁴ reported, on experiments with a normally magnetized yttrium iron garnet (YIG) disk in which the magnetic field is non-uniform, the excitation of spin waves by rf magnetic fields. He further indicated that the excited spin waves travel toward lower magnetic fields with increasing wavenumbers and eventually convert into shear elastic waves. Since then, extensive studies in YIG have been carried out on the shear elastic/spin waves propagating in both the spatially varying magnetic fields^{9, 10, 11} and temporally varying magnetic fields.^{8, 18, 20} It was later found that when the applied field is not along the propagation direction of the shear elastic/spin waves, the losses increase tremendously. This led to work on the stability of spin wave trajectories. These studies were, however, handicapped by the lack of a powerful experimental tool. Light probing appears to be a convenient and potentially powerful method, since the technique has already been widely developed to investigate elastic waves. However, in the case of YIG, which has a transparent window between 1.1 and 6

microns, the technique is of much reduced power due to the comparatively weak light sources and low sensitivity detectors available in this wavelength range. Besides, in contrast to the exhaustive work already done on elastic waves, very little^{56, 74-79} has been done with optical spin wave interactions. Accordingly, one of the prime goals of this thesis is to provide improved understanding of such interactions.

A study of the coupling of the longitudinal elastic waves and spin waves is also a major topic, since in practice it is easier to fabricate an efficient longitudinal piezoelectric transducer than a shear one. The lack of prior experimental investigations in this case is attributable to the fact that in a cubic crystal the coupling vanishes identically whenever the wave propagation is simultaneously parallel to the magnetization vector and any one of the three commonly employed principal $\langle 100, 110, 111 \rangle$ crystallographic directions, along which the elastic waves propagate as pure modes. Transverse³⁰ or obliquely magnetized¹⁴ YIG rods of appropriate orientations do provide the longitudinal coupling but the defocussing effects¹³ limit this approach.

Morgenthaler,¹⁵ in view of the fact that YIG is nearly elastically isotropic, first proposed that the longitudinal magnetoelastic coupling for waves propagating along the dc magnetization vector may be obtained if the propagation direction is not chosen along any one of the principal directions $\langle 100, 110, 111 \rangle$ but rather along a direction chosen to optimize the longitudinal magnetoelastic coupling. He found that the direction is in a $\{110\}$ plane at an angle of 25.52° from a $\langle 100 \rangle$ axis. Subsequently in our experiments,¹² using a rod oriented in a $\{100\}$ plane at (22.5°) from the $\langle 100 \rangle$ axis which provides about 90% of the maximum frequency splitting, we have indeed observed the spin/longitudinal elastic wave

propagation. Similar observations were also reported by Lewis,⁸⁵ who used a YIG rod oriented in a {100} plane at 20° from the $\langle 100 \rangle$ axis. This opened up the possibility of studying not only the various phenomena of longitudinal elastic/spin waves in spatially and/or temporally varying fields, similar to the shear wave case, but also the conversion of longitudinal elastic waves to shear waves, and vice versa, via spin wave coupling. This is the second topic to which this thesis is devoted.

In Chapter I, the equations of motion for the coupled magnetic and elastic system are reviewed, in order to provide all the necessary equations needed in the following chapter. In Chapter II, Morgenthaler's results are rederived and summarized. In Chapter III, extensive experimental studies of longitudinal and shear elastic/spin waves, in spatially and/or temporally varying magnetic fields, are described. Topics include variable delay of magnetically injected spin/longitudinal elastic waves, and conversion from the longitudinal elastic to spin waves in spatially varying fields. Frequency shifts, and pulse compression of the longitudinal elastic/spin waves subjected to pulsed magnetic fields have also been obtained. Some preliminary results on shear/longitudinal elastic wave spatial conversion via spin wave coupling are presented and discussed.

In Chapter IV, a review of light diffraction is given. It is then followed by a new theory⁷⁸ describing the phenomena of coherent light diffraction from coherent spin waves. The theory, in contrast to prior work of Auld and Wilson,⁵⁶ has appropriately taken into account all the terms linear in the small signal spin amplitudes for the perturbed dielectric tensor; the latter is the one that gives rise to the light scattering from spin or elastic waves. As a result, the theory predicts

that the intensity of the light diffracted from spin waves, unlike that from elastic waves, depends on the incident light polarization and whether the diffracted light is upshifted or downshifted in frequency. This appears to explain satisfactorily not only our experiments described in Chapter V but also observations that previous authors^{57, 58} reported as "anomalous."

In Chapter V, experimental work on light diffraction from elastic and/or spin waves is reported. Smith's work^{58, 74} on light diffracted from shear elastic/spin waves was repeated here, but, unlike his work in which he used large microwave power input and therefore non-linear interaction probably occurred, the microwave power we used was much reduced and within the linear interaction. From the experiments, we showed that the anomaly he reported indeed comes from the interaction of light and spin waves.

In section 5.3, we report the first direct observation of strong Bragg scattered infrared light (1150 nm) from microwave coherent spin waves.⁷⁸ The experiments utilized coherent spin waves generated through efficient space-gradient conversion from longitudinal elastic waves; the spin waves have negligible change of wavenumber, are converted more rapidly (therefore with less loss) and the scattered light can easily be distinguished from that due to longitudinal elastic waves. The scattered light intensity is found to be dependent on the incident light polarization and the sign of frequency shift, again in accord with our theory.

Finally, light scattering from spin waves has been used to measure the temporal conversion efficiency of longitudinal elastic waves to spin waves.

CHAPTER I

SMALL SIGNAL EQUATIONS OF MOTION OF A MAGNETOELASTIC FERROMAGNET

In this chapter, small signal equations of motion for the electro-magnetic, spin, and elastic system in a lossless magnetoelastic ferromagnet are reviewed briefly so as to provide all the necessary equations used in the later chapters. Conservation theorems for small signal power flow are also discussed. For more detailed, in-depth discussion one may refer to many excellent articles.¹⁻⁶

1.1 Small Signal Equations of Motion⁴⁻⁶

In a lossless saturated ferromagnet insulator, small signal equations of motion governing the magnetization vector and elastic displacement of the medium are described in terms of the interaction among electro-magnetic, spin, and elastic systems.

For the electromagnetic system Maxwell's equations are:

$$\nabla \times \vec{h} - \epsilon \frac{\partial \vec{e}}{\partial t} = 0 \quad (1.1a)$$

$$\nabla \times \vec{e} + \mu_0 \frac{\partial}{\partial t} (\vec{h} + \vec{m}) = 0 \quad (1.1b)$$

$$\nabla \cdot (\vec{h} + \vec{m}) = 0 \quad (1.1c)$$

$$\nabla \cdot (\epsilon \vec{e}) = 0 \quad (1.1d)$$

where the conductivity has been assumed to be zero, the permittivity ϵ is assumed to be a strain independent scalar, and the dilational variation of the small signal magnetization \vec{m} is neglected.^{5, 6}

The vectors \vec{h} , \vec{e} are the small signal Maxwellian magnetic and electric field vectors and μ_0 is the free space permeability.

The linearized torque equation for the small signal magnetization \vec{m} is given by:

$$\frac{\partial \vec{m}(\vec{r}, t)}{\partial t} = -\omega_M \vec{i}_M \times \left(\frac{-\vec{H}_i \cdot \vec{i}_M}{M} \vec{m} + \vec{h} + \vec{h}' \right) \quad (1.2)$$

where $\vec{M} = i_M M$ is the static magnetization vector, $\vec{m}(\vec{r}, t)$ the small deviation from equilibrium (and $\vec{m} \cdot \vec{M} = 0$), $\omega_M = -\gamma \mu_0 M$ and γ gyromagnetic ratio (negative for electron), $\vec{H}_i(\vec{r})$ the total static magnetic field (applied \vec{H}_0 , anisotropy \vec{H}_M^{an} , plus demagnetizing $-N_M \vec{M}$) inside the medium and \vec{h} Maxwellian rf field; the vector \vec{h}' is an effective field which gives rise to torque density from magnetic anisotropy \vec{h}^{an} , exchange \vec{h}^{ex} , magnetostriction \vec{h}^{me} and anything else. The effective magnetic field components have been discussed in great detail by Morgenthaler.^{5, 6} In the simplest case, where isotropic exchange interaction is assumed and high order interactions neglected, they can be written as (with the static magnetization vector in the +z direction):

$$H_i = H_0 - N_M M + H_M^{\text{an}} \quad (1.3a)$$

$$h_i^{\text{an}} = -\frac{1}{\mu_0} \frac{\partial w_{\text{an}}}{\partial m_i} = \sum_{j=1}^2 (-N_{ij}^{\text{an}} m_j) \quad (i = 1, 2) \quad (1.3b)$$

$$N_{ij}^{\text{an}} = N_{ji}^{\text{an}} \quad (i \neq j)$$

$$h_i^{\text{ex}} = \lambda_e \nabla^2 m_i \quad (i = 1, 2) \quad (1.3c)$$

$$h_i^{\text{me}} = -\frac{1}{\mu_0} \frac{\partial w_{\text{me}}}{\partial m_i} = -\frac{1}{\mu_0} \sum_{k=1}^3 b_{ijk} \frac{\partial \rho_i}{\partial x_k} \quad (1.3d)$$

$$b_{ijk} = b_{ikj} \quad (i = 1, 2; j, k = 1, 2, 3)$$

The quantity N_{ij}^{an} is the small signal anisotropy tensor, λ_e the isotropic

exchange constant, w_{me} the small signal magnetoelastic energy density, w_{an} the small signal anisotropy energy density, $\vec{\rho}$ the displacement vector, and b_{ijk} the first order (in strain) magnetoelastic tensor. The small signal anisotropy tensor and the first order magnetoelastic tensor are discussed in detail, respectively, in Appendix I and Appendix II.

For the elastic subsystem, use of the linearized Newton force law gives:

$$D_0 \frac{\partial^2 \rho_i}{\partial t^2} = \sum_{j,k,\ell=1}^3 \frac{\partial}{\partial x_j} \left(c_{ijkl} \frac{\partial \rho_k}{\partial x_\ell} \right) + f'_i \quad (i = 1, 2, 3) \quad (1.4)$$

where D_0 is the mass density of the medium, c_{ijkl} second order elastic constant tensor, and \vec{f}' the magnetoelastic force density (related to \vec{h}') that includes first order electromagnetic and interaction forces. In the cubic ferrimagnetic YIG, terms such as the magnetic body force are negligible; therefore f' is dominated by the linear magnetoelastic coupling and can be well approximated as:

$$f'_i \cong f_i^{me} = \sum_{j=1}^3 \frac{\partial}{\partial x_j} \left(\frac{\partial w_{me}}{\partial \left(\frac{\partial \rho_i}{\partial x_j} \right)} \right) = \sum_{j,k=1}^3 b_{kij} \frac{\partial m_k}{\partial x_j} \quad (1.5)$$

Equations (1.1), (1.2), and (1.4) are a set of time-dependent coupled differential equations, and in general are very complicated to solve. Since in this thesis we are primarily concerned with the magnetoelastic region of the spectrum, values of the wavenumber k are on the order of 10^4 cm^{-1} . In this range electromagnetic effects are small and the electric field \vec{e} in Eq. (1.1a) can be neglected to the first approximation. This results in the so-called "magnetostatic approximation",⁷ which we will use throughout the thesis.

1.2 Small Signal Power Energy Conservation Theorem^{5, 6, 8}

The contributions to the small signal energy density of the system described by Eq. (1.2) arise from magnetic, elastic, and magnetoelastic terms. The magnetic energy results from Zeeman, anisotropy, exchange, and dipolar contributions.

$$w_m = \frac{1}{2} \mu_0 \left(\frac{H_i}{M} \right) |\vec{m}|^2 + \frac{1}{2} \mu_0 \sum_{i,j=1}^2 N_{ij}^{an} m_i m_j + \frac{1}{2} \mu_0 \lambda_e (|\nabla m_x|^2 + |\nabla m_y|^2) + \frac{1}{2} \mu_0 |\vec{h}|^2 \quad (1.6)$$

The elastic term contains the kinetic and potential energies

$$w_{elas} = \frac{1}{2} D_0 \left| \frac{\partial \vec{\rho}}{\partial t} \right|^2 + \frac{1}{2} \sum_{i,j,k,\ell=1}^3 c_{ijkl} \frac{\partial \rho_i}{\partial x_j} \frac{\partial \rho_k}{\partial x_\ell} \quad (1.7)$$

The magnetoelastic component is

$$w_{me} = \sum_{i=1}^2 \sum_{j,k=1}^3 b_{ijk} m_i \frac{\partial \rho_j}{\partial x_k} \quad (1.8)$$

Notice that the energy associated with the small signal electric field \vec{e} is of higher order and is not included here. In the Poynting vector, however, the electromagnetic term is of first order and must be taken into account. Therefore Maxwell's equations (1.1) give rise to the small signal electromagnetic Poynting theorem

$$\nabla \cdot (\vec{e} \times \vec{h}) + \frac{\partial}{\partial t} \left(\frac{1}{2} \epsilon |\vec{e}|^2 + \frac{1}{2} \mu_0 |\vec{h}|^2 \right) = -\mu_0 \vec{h} \cdot \frac{\partial \vec{m}}{\partial t} \quad (1.9)$$

and (1.4) to the small signal elastic Poynting theorem

$$\nabla \cdot \vec{S}^{elas} + \frac{\partial}{\partial t} w_{elas} = \vec{f} \cdot \frac{\partial \vec{\rho}}{\partial t} \quad (1.10)$$

where

$$S_j^{\text{elas}} = - \sum_{i,k,\ell=1}^3 c_{ijkl} \frac{\partial \rho_k}{\partial x_\ell} \frac{\partial \rho_i}{\partial t} \quad (1.11)$$

In addition to the above two Poynting theorems governing the electromagnetic and elastic energy subsystems, one may also introduce other Poynting theorems^{1, 2, 5} for a material and a magnetoelastic subsystem. These conservation theorems will not be discussed here because no use of them will be made later.

Finally the Poynting theorem for the total system is found by summing the contributions of all the subsystems. In a time-varying but spatially uniform magnetic bias field, the result is:^{5, 6}

$$\nabla \cdot \vec{S}^{\text{total}} + \frac{\partial w_{\text{total}}}{\partial t} = \frac{1}{2} \mu_0 \left(\frac{|\vec{m}|^2}{M} \right) \frac{\partial H_i}{\partial t} \quad (1.12)$$

where

$$\vec{S}^{\text{total}} = (\vec{e} \times \vec{h}) + \vec{S}^{\text{elas}} + \vec{S}^{\text{m}} + \vec{S}^{\text{me}} \quad (1.13)$$

$$w_{\text{total}} = w_{\text{an}} + w_{\text{elas}} + w_{\text{me}} \quad (1.14)$$

The other small signal conservation law, namely the Stress-Momentum Conservation, has been discussed by Morgenthaler^{5, 6} and will not be repeated here. It is sufficient to summarize the conclusions that one may draw from these conservation laws. In a time-varying but spatially uniform magnetic bias field the propagation of either magnetostatic or magnetoelastic waves occurs at constant wavenumber and constant average small signal momentum but with variable frequency, average power and average energy. On the other hand, in a time invariant but spatially varying magnetic bias field the propagation of the waves occurs at constant frequency, average power and average energy

-27-

but with variable wavenumber, and average small signal momentum.^{6, 8}

CHAPTER II

PROPAGATION OF Z-DIRECTED MAGNETOELASTIC WAVES IN A GENERAL CRYSTALLOGRAPHIC DIRECTION

In the past, numerous studies of shear elastic/spin wave interactions in single crystal YIG have been reported;^{9, 10, 11} comparatively few seem to have been reported of the longitudinal elastic/spin wave coupling, and none until the recent work of Morgenthaler et al.¹² for the important case of wave propagation parallel to the magnetization vector (z-directed magnetoelastic waves). This dearth of experiments is attributable to the fact that whereas in a cubic crystal the shear magnetoelastic coupling is present regardless of the crystal orientation, this is not true for the longitudinal magnetoelastic coupling. In fact, the latter vanishes identically whenever the wave propagation is simultaneously parallel to the magnetization vector and any one of the three commonly employed principal crystallographic directions $\langle 100, 110, 111 \rangle$. Transversely magnetized rods of appropriate orientations can provide longitudinal magnetoelastic coupling but do not appear to be very useful because of strong defocusing effects.¹³ Although slight tilting of a $\langle 100 \rangle$ rod with respect to the magnetic field (magnetization vector) does allow the observation of a longitudinal elastic/spin wave interaction,¹⁴ defocusing fields limit this approach;¹³ in addition, such experiments are not easily analyzed.

Morgenthaler¹⁵ first pointed out that these problems may be overcome if the waves are allowed to propagate along the magnetization vector (z-directed) when the latter is parallel to some non-principal crystallographic direction chosen so as to optimize the longitudinal magnetoelastic coupling. Although in this case the acoustic branch

elastic waves are in general neither purely longitudinal nor transverse (shear), the elastic anisotropy of YIG given by¹⁶

$$1 - \frac{2c_{44}}{c_{11} - c_{12}} = 0.053$$

is small enough so that they may be approximated as pure modes. Subsequently we¹² reported the first experimental observations of longitudinal elastic/spin wave interaction. These detailed experimental results will be given in Chapter III.

In this chapter we will rederive the dispersion relations of magneto-elastic waves propagating in an arbitrary crystallographic direction assuming elastic isotropy but magnetoelastic anisotropy. This greatly simplifies the mathematical calculation and also provides a very good approximation insofar as longitudinal elastic/spin wave and/or degenerate shear elastic/spin wave interactions are concerned. However, in the case where two non-degenerate shear elastic modes are involved, the calculation of shear elastic/spin wave coupling neglecting elastic anisotropy is quite poor owing to the comparable magnitude of elastic and magnetoelastic frequency splittings.

We begin by studying the frequency spectrum of the uncoupled spin waves propagating in an arbitrary crystallographic direction. After introducing magnetoelastic coupling and obtaining the dispersion relations of z-directed magnetoelastic waves, we look for the particular crystallographic direction which will give the maximum value of the square of the longitudinal magnetoelastic splitting of frequencies (henceforth referred to as longitudinal magnetoelastic coupling). This direction turns out to lie in a {110} plane, at an angle of (25.52°) from

a $\langle 100 \rangle$ axis. However, the experiments to be described in the next chapter were done using a different crystallographic direction, i. e., in a $\{100\}$ plane at an angle of (22.5°) from a $\langle 100 \rangle$ axis. In this direction the longitudinal magnetoelastic coupling is approximately 80% of the maximum value. The latter direction was chosen because, for simplicity, the derivation was first carried out for the magnetization \vec{M} constrained to lie in a $\{100\}$ plane; in this case (22.5°) is the optimum angle. Finally it is shown that the longitudinal magnetoelastic coupling is proportional to $(b_1 - b_2)^2$ (b_1 and b_2 being the ordinary magnetoelastic constants), and therefore vanishes identically in the case of magneto-elastic isotropy, i. e., $b_1 = b_2$.

2.1 The Euler Angles¹⁷

Throughout the entire thesis, we always use a coordinate system $((x, y, z)$ or $(x_1, x_2, x_3))$ in which the magnetization vector \vec{M} is along the positive z -axis (or x_3 -axis as the case may be). This coordinate system is then related to the usual coordinate system (ξ, η, ζ) in which the cubic edges are chosen as the coordinate axes by the Euler Angles (φ, θ, ψ) . The latter are defined in Fig. 2.1 as:

$$\begin{aligned}\vec{x} &= R_{z'}(\psi) R_{y''}(\theta) R_{\zeta}(\varphi) \vec{\xi} \\ \text{where } \vec{x} &= (x, y, z) \text{ or } (x_1, x_2, x_3) \\ \vec{\xi} &= (\xi, \eta, \zeta)\end{aligned}$$

The operator $R_{\zeta}(\varphi)$ denotes a rotation through φ about the ζ -axis, and thus gives rise to a coordinate system (x'', y'', z'') ; the operator $R_{y''}(\theta)$ denotes a rotation through θ about the y'' -axis and thereby transforms to a coordinate system (x', y', z') ; finally, the operator $R_{z'}(\psi)$, a rotation

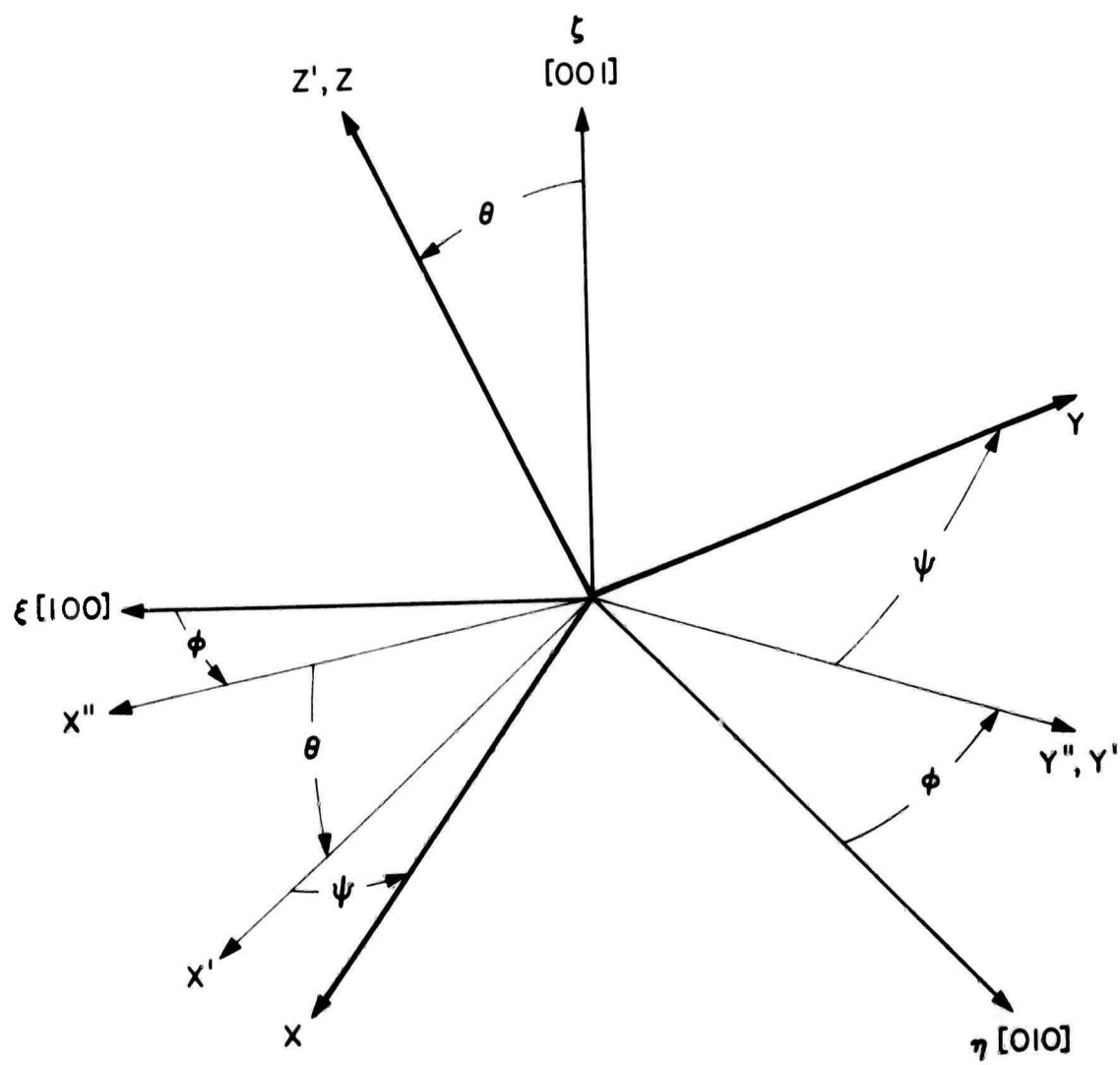


Fig. 2.1 The Euler Angles

through ψ about the z' -axis takes one to the coordinate system (x, y, z) .

Corresponding to these three operators, one defines a transformation matrix \tilde{T}^t as:

$$\vec{x} = \tilde{T}^t(\varphi, \theta, \psi) \vec{\xi} \quad (2.1)$$

where

$$\begin{aligned} \tilde{T}^t(\varphi, \theta, \psi) &= R_{z'}(\psi) R_{y''}(\theta) R_z(\varphi) \\ &= \begin{bmatrix} \cos\psi & \sin\psi & 0 \\ -\sin\psi & \cos\psi & 0 \\ 0 & 0 & 1 \end{bmatrix} \begin{bmatrix} \cos\theta & 0 & -\sin\theta \\ 0 & 1 & 0 \\ \sin\theta & 0 & \cos\theta \end{bmatrix} \begin{bmatrix} \cos\varphi & \sin\varphi & 0 \\ -\sin\varphi & \cos\varphi & 0 \\ 0 & 0 & 1 \end{bmatrix} \\ &= \begin{bmatrix} \cos\psi \cos\theta \cos\varphi - \sin\psi \sin\varphi & \cos\psi \cos\theta \sin\varphi + \sin\psi \cos\varphi & -\cos\psi \sin\theta \\ -\cos\psi \sin\varphi - \sin\psi \cos\theta \cos\varphi & +\cos\psi \cos\varphi - \sin\psi \cos\theta \sin\varphi & \sin\psi \sin\theta \\ \sin\theta \cos\varphi & \sin\theta \sin\varphi & \cos\theta \end{bmatrix} \end{aligned} \quad (2.2)$$

Since \tilde{T}^t is orthonormal, the inverse of \tilde{T}^t is equivalent to the transpose of \tilde{T}^t , i.e., \tilde{T} .

$$\vec{\xi} = \tilde{T}(\varphi, \theta, \psi) \vec{x} \quad (2.3)$$

where for $\psi = 0$:

$$\tilde{T}(\varphi, \theta, 0) = \begin{bmatrix} \cos\theta \cos\varphi & -\sin\varphi & \sin\theta \cos\varphi \\ \cos\theta \sin\varphi & \cos\varphi & \sin\theta \sin\varphi \\ -\sin\theta & 0 & \cos\theta \end{bmatrix} \quad (2.4)$$

and in general for $\psi \neq 0$:

$$\begin{aligned} \tilde{T}(\varphi, \theta, \psi) &= \\ &= \begin{bmatrix} \cos\psi \cos\theta \cos\varphi - \sin\psi \sin\varphi & -\sin\psi \cos\theta \cos\varphi - \cos\psi \sin\varphi & \sin\theta \cos\varphi \\ \cos\psi \cos\theta \sin\varphi + \sin\psi \cos\varphi & -\sin\psi \cos\theta \sin\varphi + \cos\psi \cos\varphi & \sin\theta \sin\varphi \\ -\cos\psi \sin\theta & \sin\psi \sin\theta & \cos\theta \end{bmatrix} \end{aligned} \quad (2.5)$$

2.2 Eigenvalues and Eigenmodes of Spin Waves Propagating along an Arbitrary Crystallographic Direction

In this section, the magnetoelastic interaction is neglected so that one may concentrate on the spin waves. From Eq. (1.2), one may write (neglecting \vec{h}^{me})

$$\frac{\partial m_1}{\partial t} = -\omega_M \times \left(\frac{H_i}{M} m_2 - h_2 - h_2^{an} - h_2^{ex} \right) \quad (2.6a)$$

$$\frac{\partial m_2}{\partial t} = -\omega_M \times \left(-\frac{H_i}{M} m_1 + h_1 + h_1^{an} + h_1^{ex} \right) \quad (2.6b)$$

The magnetization \vec{M} is along the positive x_3 -axis (or z -axis) and the coordinate system (x_1, x_2, x_3) used here is related to the "cubic-edge" coordinate system (ξ, η, ζ) by the Euler Angle $(\varphi, \theta, 0)$ (i. e., with $\psi = 0$). The quantities H_i , h_i^{an} and h_i^{ex} are given before in Eq. (1.3) (with $N_M \rightarrow N_3$ and $H_M^{an} \rightarrow H_3^{an}$). The Maxwellian field \vec{h} can be found through Eqs. (1.1). Since we are concerned here only with the eigenvalue problem, we assume:

$$\vec{m}(\vec{r}, t) = \text{Re} \left[\vec{m} e^{j(\omega_k t - \vec{k} \cdot \vec{r})} \right] \quad (2.7a)$$

$$\vec{h}(\vec{r}, t) = \text{Re} \left[\vec{h} e^{j(\omega_k t - \vec{k} \cdot \vec{r})} \right] \quad (2.7b)$$

$$\vec{e}(\vec{r}, t) = \text{Re} \left[\vec{e} e^{j(\omega_k t - \vec{k} \cdot \vec{r})} \right] \quad (2.7c)$$

where ω_k is the angular frequency and $\vec{k} = (k_1, k_2, k_3)$ the wavevector.

Substituting Eqs. (2.7) into Eqs. (1.1) and (2.6), while using the "magnetostatic approximation" mentioned earlier, one obtains:

$$h_i = - \frac{(\vec{m} \cdot \vec{k})}{k^2} k_i = - \frac{(m_1 k_1 + m_2 k_2)}{k^2} k_i \quad (i = 1, 2) \quad (2.8)$$

$$\frac{\partial m_1}{\partial t} = -\omega_M(N_{21} + \frac{k_1 k_2}{k^2})m_1 - \left[\omega_3^i + (N_{22} + \frac{k_2^2}{k^2})\omega_M + \lambda k^2 \omega_M \right] m_2 \quad (2.9a)$$

$$\frac{\partial m_2}{\partial t} = \left[\omega_3^i + (N_{11} + \frac{k_1^2}{k^2})\omega_M + \lambda k^2 \omega_M \right] m_1 + \omega_M(N_{12} + \frac{k_1 k_2}{k^2})m_2 \quad (2.9b)$$

where

$$\omega_3^i = -\gamma\mu_O H_i = -\gamma\mu_O (H_O - N_3 M + H_3^{an}) \quad (2.10a)$$

In Appendix I, both H_3^{an} and N_{ij}^{an} are derived in terms of the Euler Angles $(\varphi, \theta, 0)$ and the anisotropy constant K_1 . Furthermore, it is shown there that one may write

$$\omega_3^i = -\gamma\mu_O H_i = -\gamma\mu_O (H_O - N_3 M) \quad (2.10b)$$

provided that N_{ij}^{an} is replaced by $N_{ij}'^{an}$ defined in Appendix I. We rewrite Eq. (2.10) into a matrix form:

$$\frac{d}{dt} \begin{bmatrix} m_1 \\ m_2 \end{bmatrix} = \begin{bmatrix} -C & -B \\ A & C \end{bmatrix} \begin{bmatrix} m_1 \\ m_2 \end{bmatrix} \quad (2.11a)$$

$$\text{where} \quad A = \omega_3^i + (N_{11} + \frac{k_1^2}{k^2})\omega_M + \lambda_e k^2 \omega_M \quad (2.11b)$$

$$B = \omega_3^i + (N_{22} + \frac{k_2^2}{k^2})\omega_M + \lambda_e k^2 \omega_M \quad (2.11c)$$

$$C = \omega_M(N_{12} + \frac{k_1 k_2}{k^2}) \quad (2.11d)$$

In order to find the major and minor axes of the elliptical spin polarization, it is helpful to introduce the third Euler Angle ψ , i. e., a rotation through ψ about the z-axis. We thus write:

$$\begin{bmatrix} m_1 \\ m_2 \end{bmatrix} = \begin{bmatrix} \cos\psi & -\sin\psi \\ \sin\psi & \cos\psi \end{bmatrix} \begin{bmatrix} m_1^p \\ m_2^p \end{bmatrix} \quad (2.12)$$

where m_1^p and m_2^p are along the major and minor axes of the ellipse.

Substituting Eq. (2.12) into (2.11a), one obtains:

$$\begin{aligned} \frac{d}{dt} \begin{bmatrix} m_1^p \\ m_2^p \end{bmatrix} &= \begin{bmatrix} \cos\psi & +\sin\psi \\ -\sin\psi & \cos\psi \end{bmatrix} \begin{bmatrix} -C & -B \\ A & C \end{bmatrix} \begin{bmatrix} \cos\psi & -\sin\psi \\ \sin\psi & \cos\psi \end{bmatrix} \begin{bmatrix} m_1^p \\ m_2^p \end{bmatrix} \\ &= \begin{bmatrix} -C \cos 2\psi - \frac{1}{2} \sin 2\psi (A - B) & -(A \cos^2 \psi + B \sin^2 \psi - C \sin 2\psi) \\ A \sin^2 \psi + B \cos^2 \psi + C \sin 2\psi & C \cos 2\psi + \frac{1}{2} \sin 2\psi (A - B) \end{bmatrix} \begin{bmatrix} m_1^p \\ m_2^p \end{bmatrix} \end{aligned} \quad (2.13)$$

We now demand that the diagonal elements of the above matrix be equal to zero. Thus:

$$\tan 2\psi = \frac{2C}{B-A} = \frac{2\left(N_{12} + \frac{k_1 k_2}{k^2}\right)}{(N_{22} - N_{11}) + \left(\frac{k_2^2}{k^2} - \frac{k_1^2}{k^2}\right)} \quad (2.14)$$

where, from Appendix I,

$$N_{11} = \frac{2K_1}{\mu_o M^2} \left[-\frac{3}{2} \sin^2 2\theta \left(1 - \frac{1}{4} \sin^2 2\varphi \right) \right] \quad (2.15a)$$

$$N_{22} = \frac{2K_1}{\mu_o M^2} \left[-\frac{3}{2} \sin^2 \theta \sin^2 2\varphi \right] \quad (2.15b)$$

$$N_{12} = \frac{2K_1}{\mu_o M^2} \left[-\frac{3}{8} \sin \theta \sin 2\theta \sin 4\varphi \right] \quad (2.15c)$$

From Eqs. (2.14) and (2.15), one realizes that the angle ψ in general is a complicated function of θ, φ , and the direction of propagation $\vec{k}/|\vec{k}|$.

Solving Eq. (2.13) subject to the condition of Eq. (2.14), one obtains

$$\vec{m}^P = \vec{i}_1 a \cos(\omega_k t - \vec{k} \cdot \vec{r}) + \vec{i}_2 b \sin(\omega_k t - \vec{k} \cdot \vec{r}) \quad (2.16)$$

where

$$\frac{a}{b} = \left(\frac{\omega_1}{\omega_2} \right)^{\frac{1}{2}} \quad (2.17)$$

and

$$\omega_1 = A \cos^2 \psi + B \sin^2 \psi - C \sin 2\psi \quad (2.18a)$$

$$\omega_2 = A \sin^2 \psi + B \cos^2 \psi + C \sin 2\psi \quad (2.18b)$$

$$\omega_k^2 = \omega_1 \omega_2 = AB - C^2 \quad (2.18c)$$

A plot of ω_k vs k (with k_1 and k_2 as parameters) is shown in Fig. 2.2. It can be shown that the lower bound of the spin wave manifold is the z-directed waves (i.e., $k_1 = k_2 = 0$). For YIG, $N_{11}\omega_M$, $N_{22}\omega_M$ and $N_{12}\omega_M$ are usually small compared to ω_3^i at microwave frequencies. Therefore one may deduce from Eq. (2.18c) that the upper bound of the spin wave manifold is approximately the waves with wavevector \vec{k} perpendicular to the dc magnetization \vec{M} .

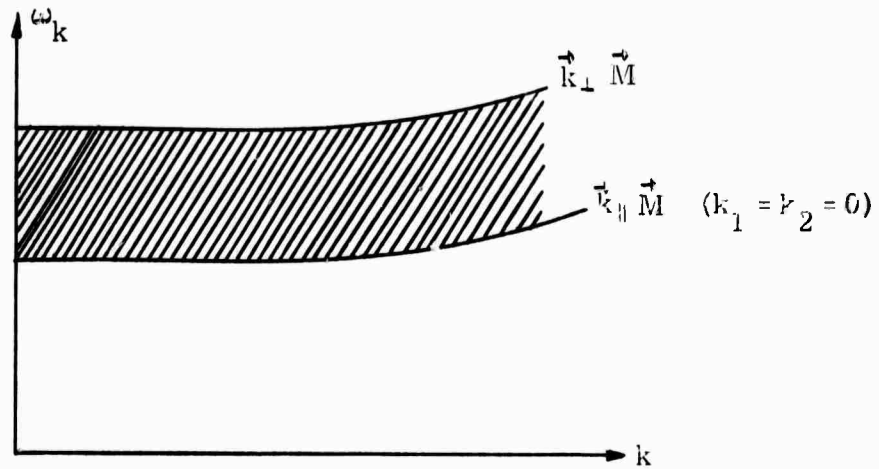


Fig. 2.2 Dispersion diagram for spin waves.

2.3 Dispersion of z-Directed Magnetoelastic Waves in an Elastically Isotropic but Magnetoelastic Anisotropic "Cubic" Medium

We assume here that the coordinate system (x_1, x_2, x_3) used here has been transformed through the Euler Angle (φ, θ, ψ) from the "cubic-edge" coordinate system (ξ, η, ζ) , so that the dc magnetization is along the z-axis and the major and minor axes of the elliptical spin wave polarization are along the x_1 and x_2 axes. Then from Eqs. (1.2) and (1.3), the coupled spin wave equations of motion are written as:

$$\frac{\partial m_1}{\partial t} = -\omega_1 m_2 + \sum_{j,k=1}^3 \frac{\omega_M}{\mu_0} b_{2jk} \frac{\partial \rho_j}{\partial x_k} \quad (2.19a)$$

$$\frac{\partial m_2}{\partial t} = \omega_2 m_1 - \sum_{j,k=1}^3 \frac{\omega_M}{\mu_0} b_{1jk} \frac{\partial \rho_j}{\partial x_k} \quad (2.19b)$$

where ω_1 and ω_2 are given by Eq. (2.18) and b_{ijk} are given in Appendix II.

For the isotropic elastic case, we can write from Eq. (1.4)

$$\begin{aligned} D_0 \frac{\partial^2 \rho_i}{\partial t^2} = & c_{44} \nabla^2 \rho_i + (c_{12} + c_{44}) \frac{\partial}{\partial x_i} \left(\frac{\partial \rho_1}{\partial x_1} + \frac{\partial \rho_2}{\partial x_2} + \frac{\partial \rho_3}{\partial x_3} \right) \\ & + \sum_{j,k=1}^3 b_{kij} \frac{\partial m_k}{\partial x_j} \quad (i = 1, 2, 3) \end{aligned} \quad (2.20)$$

where c_{11} , c_{12} and c_{44} are the elastic constants and $c_{11} \cong c_{12} + 2c_{44}$ for YIG.

As in Eq. (2.7) we assume

$$\vec{m}(\vec{r}, t) = \text{Re} \left[\underline{\vec{m}} e^{j(\omega t - \vec{k} \cdot \vec{r})} \right] \quad (2.21a)$$

$$\vec{\rho}(\vec{r}, t) = \text{Re} \left[\underline{\vec{\rho}} e^{j(\omega t - \vec{k} \cdot \vec{r})} \right] \quad (2.21b)$$

where $\vec{k} = (k_1, k_2, k_3)$.

Substituting Eqs. (2.21) into Eqs. (2.19), we obtain:

$j\omega$	ω_2	$\sum_{k=1}^3 j \frac{\omega_M}{\mu_0} b_{21k} k_k$	$\sum_{k=1}^3 j \frac{\omega_M}{\mu_0} b_{22k} k_k$	$\sum_{k=1}^3 j \frac{\omega_M}{\mu_0} b_{23k} k_k$	\underline{m}_1
ω_1	$-j\omega$	$\sum_{k=1}^3 j \frac{\omega_M}{\mu_0} b_{11k} k_k$	$\sum_{k=1}^3 j \frac{\omega_M}{\mu_0} b_{12k} k_k$	$\sum_{k=1}^3 j \frac{\omega_M}{\mu_0} b_{13k} k_k$	\underline{m}_2
$\sum_{j=1}^3 j b_{11j} k_j$	$\sum_{j=1}^3 j b_{21j} k_j$	$-D_0 \omega^2 + c_{44} k^2$ $+(c_{12} + c_{44}) k_1^2$	$(c_{12} + c_{44}) k_1 k_2$	$(c_{12} + c_{44}) k_1 k_2$	$\underline{\rho}_1$
$\sum_{j=1}^3 j b_{12j} k_j$	$\sum_{j=1}^3 j b_{22j} k_j$	$(c_{12} + c_{44}) k_1 k_2$	$-D_0 \omega^2 + c_{44} k^2$ $+(c_{12} + c_{44}) k_2^2$	$(c_{12} + c_{44}) k_2 k_3$	$\underline{\rho}_2$
$\sum_{j=1}^3 j b_{13j} k_j$	$\sum_{j=1}^3 j b_{23j} k_j$	$(c_{12} + c_{44}) k_1 k_3$	$(c_{12} + c_{44}) k_2 k_3$	$-D_0 \omega^2 + c_{44} k^2$ $+(c_{12} + c_{44}) k_3^2$	$\underline{\rho}_3$

= 0

(2.22)

The eigenvalues can be found by equating the determinant of the square matrix in Eq. (2.22) to zero. Here we are interested only in z-directed waves; therefore $k_1 = k_2 = 0$, but $k_3 = k$, and

$$\det \begin{bmatrix} j\omega & \omega_2 & j \frac{\omega_M}{\mu_0} b_{213} k & j \frac{\omega_M}{\mu_0} b_{223} k & j \frac{\omega_M}{\mu_0} b_{233} k \\ \omega_1 & -j\omega & j \frac{\omega_M}{\mu_0} b_{113} k & j \frac{\omega_M}{\mu_0} b_{123} k & j \frac{\omega_M}{\mu_0} b_{133} k \\ j b_{113} k & j b_{213} k & -D_0 \omega^2 + c_{44} k^2 & 0 & 0 \\ j b_{123} k & j b_{223} k & 0 & -D_0 \omega^2 + c_{44} k^2 & 0 \\ j b_{133} k & j b_{233} k & 0 & 0 & -D_0 \omega^2 + c_{11} k^2 \end{bmatrix} = 0$$

(2.23)

Recall an identity of determinants

$$\det \begin{bmatrix} W & X \\ Y & Z \end{bmatrix} = \det (W - XZ^{-1}Y) \det Z \quad (2.24)$$

where W and Z in the diagonal must be square matrices. Using (2.24) one obtains:

$$\begin{aligned} & (\omega^2 - \omega_1 \omega_2) (\omega^2 - \omega_\ell^2) (\omega^2 - \omega_s^2)^2 \\ &= \frac{\omega_M^2 k^2}{D_o \mu_o} (\omega^2 - \omega_s^2) \{ (\omega^2 - \omega_s^2) (\omega_1 b_{133}^2 + \omega_2 b_{233}^2) + (\omega^2 - \omega_\ell^2) \cdot \\ & \quad [\omega_1 (b_{113}^2 + b_{123}^2) + \omega_2 (b_{213}^2 + b_{223}^2)] \} + \left(\frac{\omega_M^2 k^2}{D_o \mu_o} \right)^2 \cdot \quad (2.25) \\ & \quad \{ (\omega^2 - \omega_s^2) [(b_{133} b_{213} - b_{113} b_{233})^2 + (b_{233} b_{133} - b_{233} b_{123})^2] \\ & \quad + (\omega^2 - \omega_\ell^2) (b_{123} b_{213} - b_{113} b_{223})^2 \} \end{aligned}$$

where

$$\omega_\ell = v_\ell k = \sqrt{\frac{c_{11}}{D_o}} k \quad (2.26a)$$

$$\omega_s = v_s k = \sqrt{\frac{c_{44}}{D_o}} k \quad (2.26b)$$

Note that the term containing $\left(\frac{\omega_M^2 k^2}{D_o \mu_o} \right)^2$ in Eq. (2.25) is of fourth power of the magnetoelastic constants b_{ijk} and usually negligible. For YIG, even near the region where either $\omega \cong \omega_\ell$ (longitudinal crossover) or $\omega \cong \omega_s$ (shear crossover) the value of this term is at most 5% of that of other terms at microwave frequencies. From Eq. (2.25), one therefore has:

$$(\omega^2 - \omega_k^2)(\omega^2 - \omega_\ell^2)(\omega^2 - \omega_s^2) = (\omega^2 - \omega_s^2)\omega_\ell \omega_k b_\ell^2 + (\omega^2 - \omega_\ell^2)\omega_s \omega_k b_s^2 \quad (2.27)$$

where

$$b_\ell^2 = \frac{\omega_M k^2}{D_0 \mu_0} \frac{1}{\omega_\ell \omega_k} (\omega_1 b_{133}^2 + \omega_2 b_{233}^2) \quad (2.28a)$$

$$b_s^2 = \frac{\omega_M k^2}{D_0 \mu_0} \frac{1}{\omega_s \omega_k} [\omega_1 (b_{113}^2 + b_{123}^2) + \omega_2 (b_{213}^2 + b_{223}^2)] \quad (2.28b)$$

Notice in Eq. (2.27) that when $\omega \cong \omega_\ell$, i.e., near the longitudinal crossover, the term containing b_ℓ^2 is dominant on the right-hand side, while when $\omega \cong \omega_s$, i.e., near the shear crossover, the term containing b_s^2 is. The quantities b_ℓ^2 and b_s^2 are, therefore, defined as the longitudinal and shear magnetoelastic couplings, respectively.

Now let us proceed to maximize the longitudinal magnetoelastic coupling b_ℓ^2 by choosing an appropriate propagation direction with respect to the crystallographic axis (i.e., a particular set of the Euler Angles (φ, θ, ψ) where ψ is a function of (φ, θ) given in Eq. (2.14)). In general, this problem is quite involved. However, the simple approximation $\frac{\omega_1}{\omega_2} \cong 1$ may be made for z-directed waves in YIG at microwave frequencies. The ratio $\frac{\omega_1}{\omega_2}$ is the square of the ellipticity of the spin waves (Eq.(2.17)) which, for the z-directed waves, is due to the anisotropy field alone and therefore very close to 1. Using this approximation one obtains:

$$\omega_k \cong \omega_1 \cong \omega_2 \quad (2.29)$$

The quantities b_ℓ^2 and b_s^2 can be rewritten as:

$$b_\ell^2 = \frac{\omega_M k^2}{D_0 \mu_0} \frac{1}{\omega_\ell} (b_{133}^2 + b_{233}^2) \quad (2.30a)$$

$$b_s^2 \cong \frac{\omega_M k^2}{D_o \mu_o} \frac{1}{\omega_s} [(b_{113}^2 + b_{123}^2) + (b_{213}^2 + b_{223}^2)] \quad (2.30b)$$

Thus we are left with the problem of maximizing $b_\ell^2 = \frac{\omega_M k^2}{D_o \mu_o} \frac{1}{\omega_\ell} (b_{133}^2 + b_{233}^2)$ which, according to Appendix II, (A2.14), is independent of ψ , i. e., of rotations around the dc magnetization (z-axis). From (A2.14) in Appendix II we have:

$$b_\ell^2 = \left(\frac{\omega_M k^2}{D_o \mu_o} \frac{1}{\omega_\ell} \right) b_{\text{eff}}^2 \quad (2.31a)$$

where

$$b_{\text{eff}}^2 = \frac{(b_2 - b_1)^2}{M^2} \left[\frac{1}{4} \sin^2 4\theta + \sin^2 2\varphi \left(\frac{1}{2} \sin^2 \theta \sin 2\theta \sin 4\theta + \frac{1}{4} \sin^2 2\varphi \sin^4 \theta \sin^2 2\theta \right) + \frac{1}{4} \sin^6 \theta \sin^2 4\varphi \right] \quad (2.31b)$$

A numerical analysis to maximize b_{eff}^2 in Eq. (2.31b) by choosing angles (φ, θ) gives:

$$(b_{\text{eff}}^2)_{\text{max}} = 1.26 \times \frac{(b_2 - b_1)^2}{4M^2} \quad (2.32a)$$

when

$$(\varphi)_{\text{max}} = 45^\circ \quad (2.32b)$$

$$(\theta)_{\text{max}} = 25.52^\circ \quad (2.32c)$$

From Eqs. (2.32b) and (2.32c), one realizes that the propagation direction that optimizes the longitudinal magnetoelastic coupling for z-directed waves is in a {110} plane $((\varphi)_{\text{max}} = 45^\circ)$ at 25.52° from a $\langle 100 \rangle$ axis; the coupling is independent of the magnetic anisotropy (within the approximation of small spin wave ellipticity) and directly proportional to the $(b_1 - b_2)^2$, which is a measure of magnetoelastic anisotropy. When $b_1 = b_2$, corresponding to magnetoelastic isotropy, then the coupling vanishes identically.

Let us conclude this chapter by working out explicitly both the longitudinal and shear magnetoelastic coupling in the {100} and {110} planes.

First of all, we rewrite the angle ψ in Eq. (2.14) in terms of (φ, θ) explicitly from Eq. (2.15) and under the condition of z-directed waves ($\vec{k} = \vec{i}_3 k$) as:

$$\tan 2\psi = \frac{\cos \theta \sin 4\varphi}{4 \cos^2 \theta - \sin^2 2\varphi (1 + \cos^2 \theta)} \quad (2.33)$$

Then we have for

$$(1) \quad \{100\} \text{ plane } (\varphi = 0)$$

From Eq. (2.33), $\psi = 0$, letting $\omega \approx \omega_\ell$ or $\omega \approx \omega_s$ in the appropriate places, and obtaining b_{ijk} 's from Appendix II, Table 2A.2; the result is:

$$(\omega - \omega_k)(\omega - \omega_\ell)(\omega - \omega_s) = \frac{1}{4} [(\omega - \omega_s) b_\ell^2 + (\omega - \omega_\ell) b_s^2] \quad (2.34)$$

where

$$b_\ell^2(\varphi=0, \theta) = \frac{(b_2 - b_1)^2 \sin^2 4\varphi \omega_M \omega}{4 c_{11} \mu_0 M^2} \quad (2.35a)$$

$$b_s^2(\varphi=0, \theta) = \frac{\{b_2^2 + [b_2 + (b_1 - b_2) \sin^2 2\theta]^2\} \omega_M \omega}{c_{44} \mu_0 M^2} \quad (2.35b)$$

and use has been made of:

$$\frac{\omega}{c_{11}} \approx \frac{k^2}{D_o \omega_\ell} \quad (2.36a)$$

and

$$\frac{\omega}{c_{44}} \approx \frac{k^2}{D_o \omega_s} \quad (2.36b)$$

A plot of $b_\ell^2(0, \theta)$ and $b_s^2(0, \theta)$ is shown in Fig. 2.3 where values of b_1 and b_2 for YIG at room temperature are used for Fig. 2.3b. Notice the

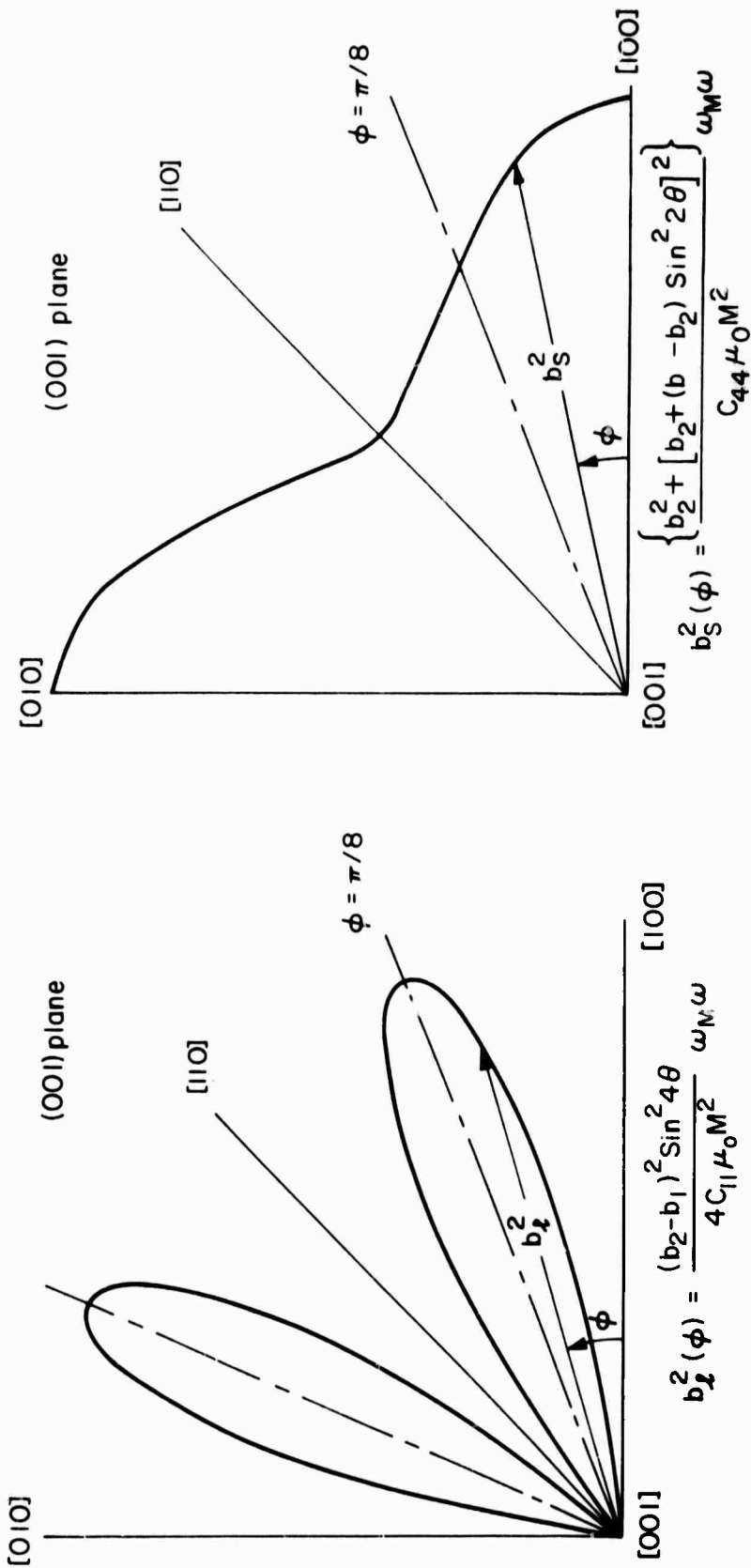


Fig. 2.3 Longitudinal and shear magnetoelastic couplings of z-directed waves in a $\{100\}$ plane.

maximum b_ℓ^2 in the {100} plane occurs at $\sin^2 4\theta = 1$ or $\theta = \frac{\pi}{8}$ (22.5° from a $\langle 100 \rangle$ axis) and the value of b_ℓ^2 in this case is 80% of the absolute maximum $(b_\ell^2)_{\max}$ in Eq. (2.32a). Because of availability, this " 22.5° " direction is chosen in the experiments described in Chapter III. For shear magnetoelastic coupling, the minimum value in the {100} plane occurs at $\sin^2 2\theta = 1$ or $\theta = \frac{\pi}{4}$ ($\langle 110 \rangle$ direction). The numerical values of b_ℓ (longitudinal magnetoelastic frequency splittings) and b_s (shear magnetoelastic frequency splittings) for YIG at room temperature in the " 22.5° " direction are given by:

$$2\pi b_\ell(0, \frac{\pi}{8}) = 5.53\sqrt{f} \quad (\text{MHz}) \quad (2.37a)$$

$$2\pi b_s(0, \frac{\pi}{8}) = 45.5\sqrt{f} \quad (\text{MHz}) \quad (2.37b)$$

where f is the frequency (in GHz).

$$(2) \quad \{110\} \text{ plane} \quad (\varphi = \frac{\pi}{4})$$

From Eq. (2.33), $\psi = 0$, letting $\omega \cong \omega_\ell$ or $\omega \cong \omega_s$ in the appropriate places and obtaining b_{ijk} 's from Appendix II, Table 2A.2; the result is:

$$(\omega - \omega_k)(\omega - \omega_\ell)(\omega - \omega_s) = \frac{1}{4}[(\omega - \omega_s)b_\ell^2 + (\omega - \omega_\ell)b_s^2] \quad (2.38)$$

where

$$b_\ell^2(\varphi = \frac{\pi}{4}, \theta) = \frac{(b_2 - b_1)^2 \omega_M \omega}{4 c_{11} \mu_0 M^2} (\sin 4\theta + \sin^2 \theta \sin 2\theta)^2 \quad (2.39a)$$

$$b_s^2(\varphi = \frac{\pi}{4}, \theta) = \frac{\omega_M \omega}{c_{44} \mu_0 M^2} [(b_2 + \frac{3}{4}(b_1 - b_2) \sin^2 2\theta)^2 + (b_2 + (b_1 - b_2) \sin^2 \theta)^2] \quad (2.39b)$$

A plot of $b_\ell^2(\frac{\pi}{4}, \theta)$ and $b_s^2(\frac{\pi}{4}, \theta)$ is shown in Fig. 2.4, where values of b_1 and b_2 for YIG at room temperature are used for Fig. 2.4b. The

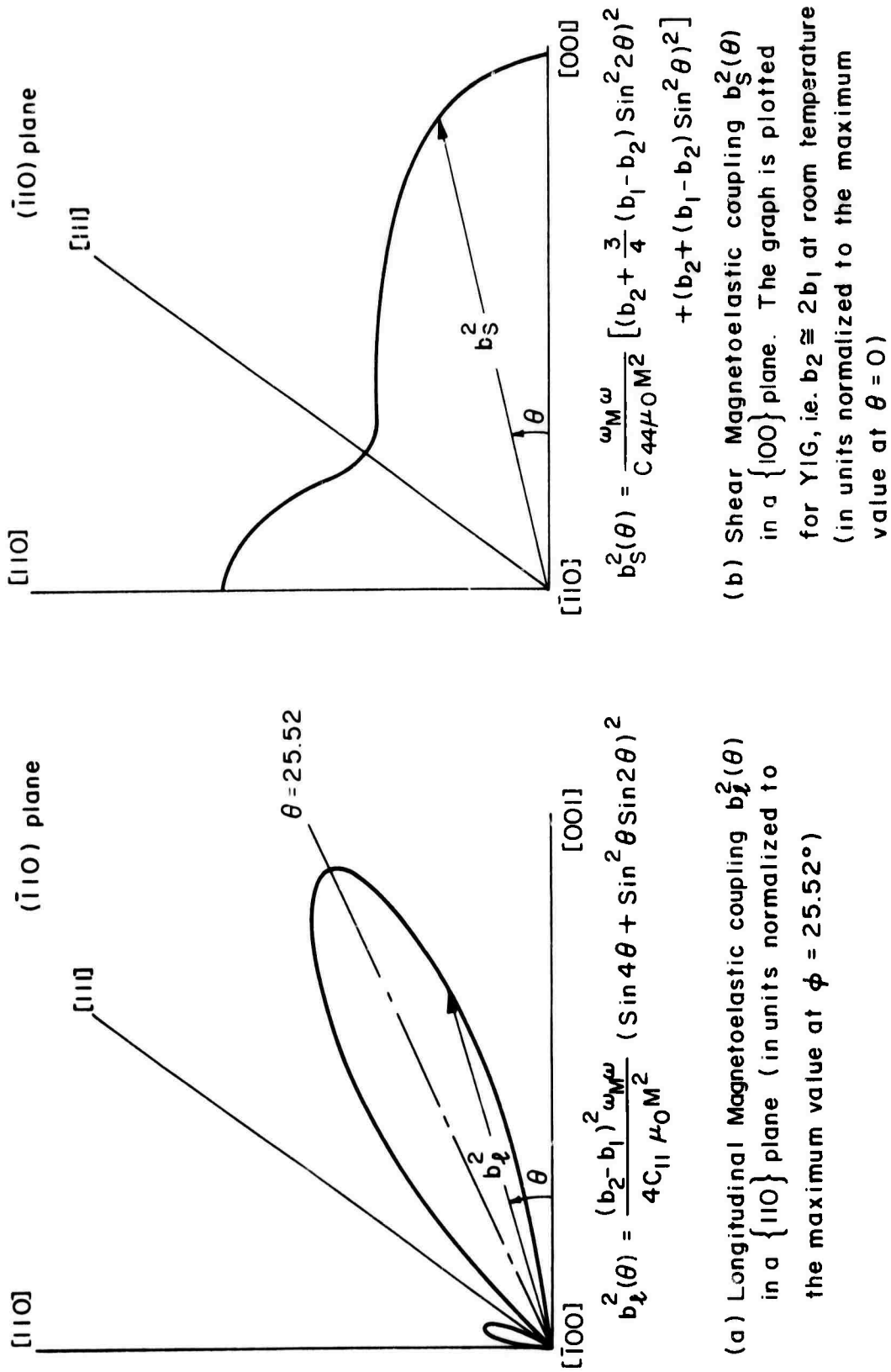


Fig. 2.4 Longitudinal and shear magnetoelastic couplings of z-directed waves in a $\{110\}$ plane.

numerical values of b_ℓ and b_s for YIG at room temperature at $\theta = 25.52^\circ$ are given by:

$$2\pi b_\ell(\frac{\pi}{4}, 25.52^\circ) = 6.20\sqrt{f} \quad (\text{MHz}) \quad (2.40a)$$

$$2\pi b_s(\frac{\pi}{4}, 25.52^\circ) = 36.1\sqrt{f} \quad (\text{MHz}) \quad (2.40b)$$

Finally, the dispersion of z-directed waves (Eqs. (2.34) or (2.37)) is shown in Fig. (2.5), where both longitudinal and shear magnetoelastic splittings are indicated. Note from Fig. (2.4) or Eq. (2.31b) that the longitudinal magnetoelastic coupling (or frequency splittings) vanishes identically when the propagation direction of z-directed waves is along any of the three principal crystallographic directions $\langle 100, 110, 111 \rangle$.

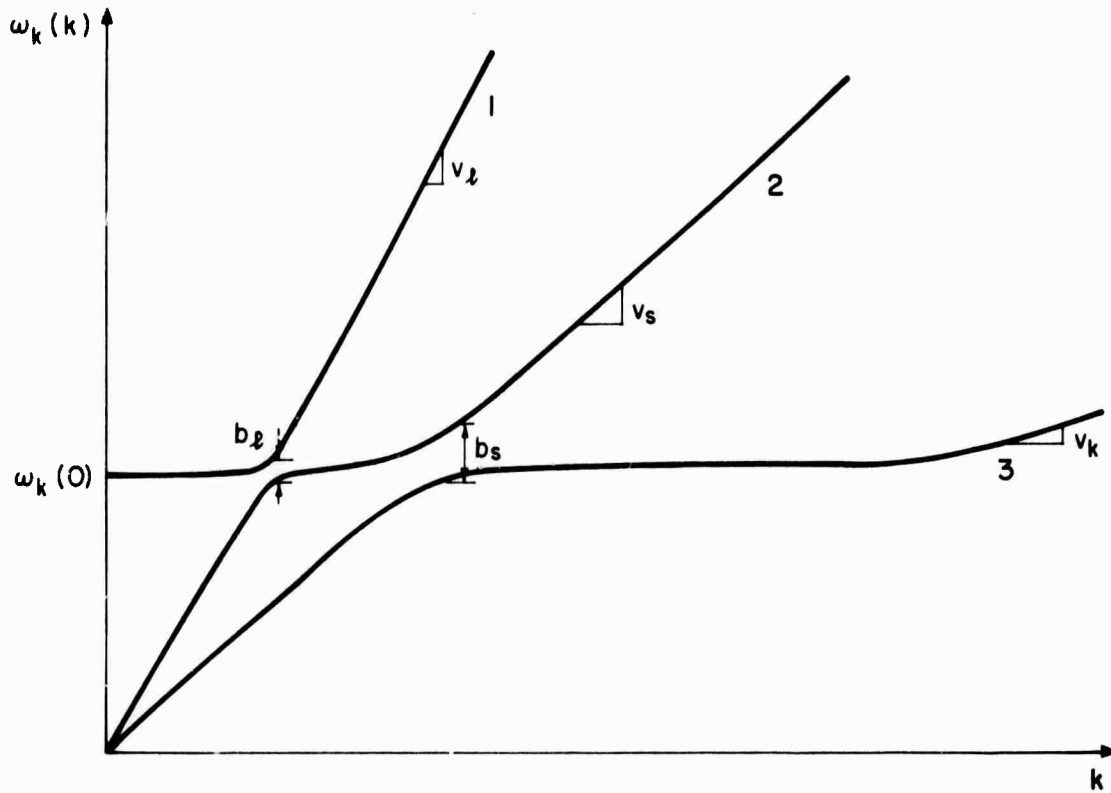


Fig. 2.5 Dispersion diagram for z -directed magnetoelastic waves; the spin/longitudinal and spin/shear wave splittings (b_ℓ and b_s) are shown very much exaggerated. The quantities v_ℓ , v_s and v_k are, respectively, group velocities of longitudinal elastic, shear elastic and spin waves; the branch numbers are referred to in the text.

CHAPTER III

EXPERIMENTAL RESULTS OF Z-DIRECTED MAGNETOELASTIC WAVES USING MICROWAVE TECHNIQUES

In this chapter, microwave experimental results are reported for both longitudinal and shear elastic/spin waves propagating in spatially and/or temporally varying magnetic fields. The calculations made in the last chapter are used to interpret the results.

In the past, a number of authors have studied shear elastic/spin waves in YIG using either spatially^{10, 11} or temporally varying magnetic fields.^{8, 18} Here similar studies on the previously-unexplored longitudinal elastic/spin waves were carried out. (Some results have been reported.^{12, 19}) Both magnetic injection from "fine wire"¹⁰ and acoustic injection from piezoelectric transducers were employed. Variable delay and conversion of longitudinal elastic/spin waves in spatially varying fields are reported. Frequency shifts and pulse compression of the longitudinal elastic/spin waves subjected to pulsed magnetic fields have also been obtained. Finally, some preliminary experiments on shear/longitudinal elastic wave spatial conversion via spin waves are presented and discussed. Results of laser probing of magnetoelastic waves through infra-red Bragg scattering are reported later in Chapter V.

In all the experiments described here, either a YIG rod or a rectangular bar, with the symmetry (or long) axis oriented in a {100} plane at an angle of (22.5°) from a $\langle 100 \rangle$ direction, hereon referred to as the " 22.5° " direction, was used. From the results of the last chapter it is shown that this crystallographic direction provides nearly

80% of the maximum z-directed longitudinal magnetoelastic coupling (nearly 90% of the maximum longitudinal magnetoelastic splittings in frequency).

3.1 Experimental Setup

Static bias magnetic fields were provided by an electromagnet and the pulsed magnetic fields were produced by means of a coil wound around the sample and driven by a current pulser. All experiments were done at room temperature.

The L-band microwave apparatus used is identical to that of Rezende²⁰ and is shown in Fig. 3.1. It consists basically of a signal generator (Alfred 650 main frame and 651A rf head, 1-2 GHz) followed by two attenuators (HP 354A and Alfred E101) in tandem, and a PIN modulator (HP 8731B). The PIN modulator is capable of producing rf pulses as short as 100 nsec. A circulator (Sperry D52L21) was used when reflection measurements were made. A stub tuner (Weinschel DS109) which follows the circulator for matching load impedances was taken out of the circuitry when short rf pulses were employed. The receiver system consists of either a narrow-band superheterodyne or a wide-band system. The former is composed of a local oscillator (GR 1021-P2), a balanced mixer/preamplifier (LEL LAC-3-60-12-50, bandwidth 12 MHz) and a 60 MHz IF amplifier (LEL IMM-2-7480, bandwidth 10 MHz). The wide-band system is formed by a transistor amplifier (Avantek AM-1000-0, G = 25 db, NF = 6 db), followed by a TWT amplifier (HP 489A, G = 35 db, NF = 30 db), and finally a tunnel diode detector (Aerotech D104B). The output of the tunnel diode is amplified by 40 db before being fed into a Tektronix 585 scope.

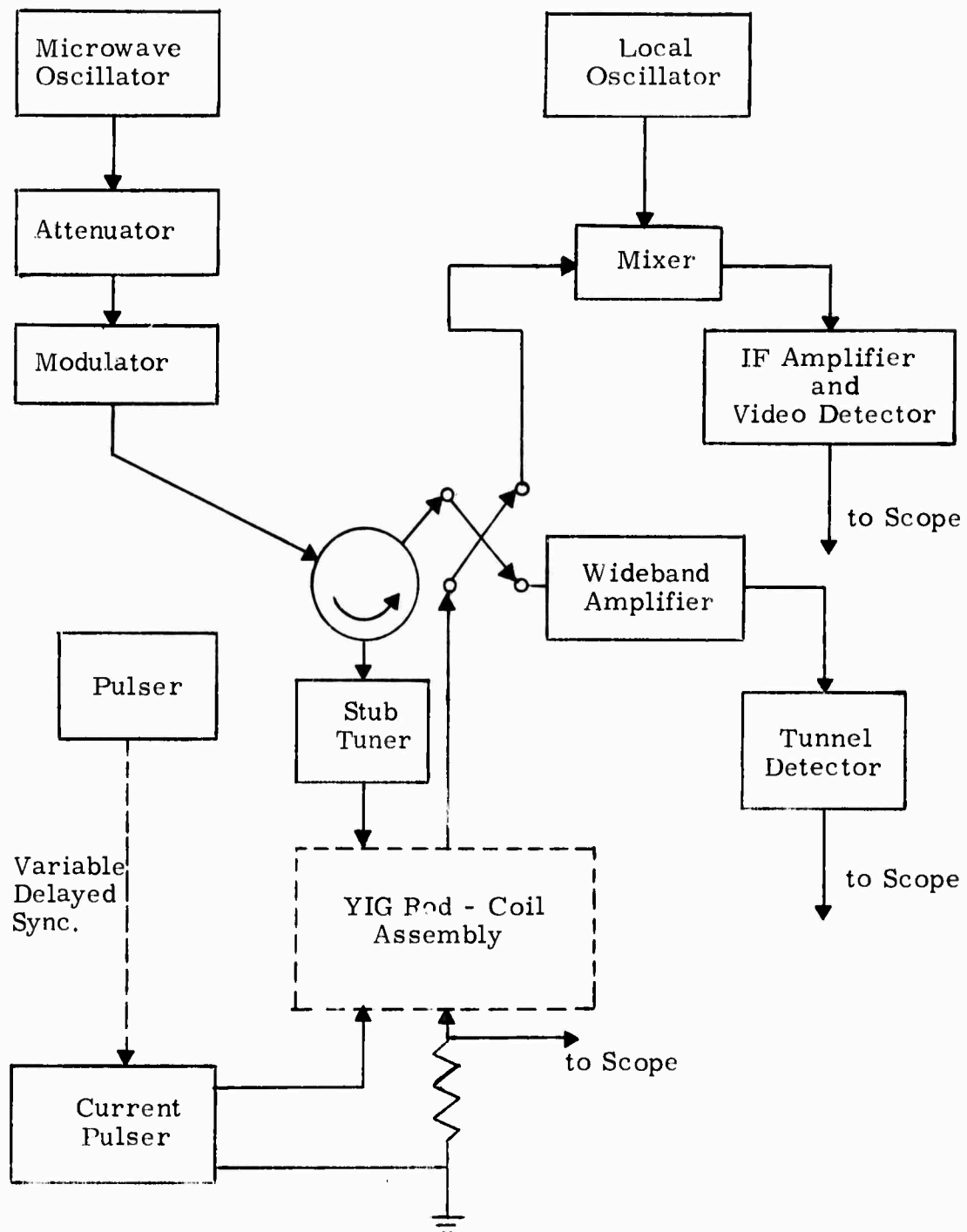


Fig. 3.1 Block diagram of L-band microwave circuitry.

3.2 Experiments with Spin Wave Injections

The propagation of shear elastic/spin waves in an axially magnetized YIG rod has been studied theoretically by Schlömann and Joseph,¹¹ Auld et al.,²⁴ and experimentally by Eshbach and Strauss.⁹¹⁰ The internal field $H_i(z)$ in a YIG rod or a rectangular bar is nonuniform and given before by Eq. (1.3a):

$$H_i(z) = H_0 + H_3^{\text{an}} + H^{\text{dem}} \quad (1.3a)$$

where H_0 is the externally applied field, H_3^{an} is the effective anisotropy field and H^{dem} is the demagnetizing field. The variation of the latter along the axis of the rod or the long axis of the rectangular bar is given, respectively, to first order in M/H_0 by the Sommerfeld formula²² for the rod:

$$H^{\text{dem}} = -\frac{M}{2} \left\{ 2 - \frac{L-z}{[(L-z)^2 + \frac{D^2}{4}]^{\frac{1}{2}}} - \frac{z}{[z^2 + \frac{D^2}{4}]^{\frac{1}{2}}} \right\} \quad (3.1a)$$

where $z = 0$ is taken at one of the end faces, L is the length of the rod, and D the diameter, and for the bar:²³

$$H^{\text{dem}} = -\frac{M}{\pi} [\cot^{-1} f(0, 0, z) + \cot^{-1} f(0, 0, -z)] \quad (3.1b)$$

with

$$f(0, 0, z) = \frac{[(WD)^2 + (HT)^2 + (L-2z)^2](L-2z)}{2(WD) \times (HT)}$$

where $z = 0$ is taken at the center of the long axis, L is the length of the long axis of the bar and HT , WD the transverse dimensions. The axial internal field profiles in each case are shown in Fig. 3.2.

3.2a Spin/Longitudinal Elastic Wave Conversion¹²

The room temperature experiments were carried out at 1.5 GHz

using a single crystal YIG rod ($L = 0.99$ cm, $D = 0.3$ cm) with its symmetry axis oriented along the " 22.5° " direction and both end surfaces optically polished; fine wire excitation was used. The results are best explained with the use of the dispersion curve shown in Fig. 2.5 and the internal field profile shown in Fig. 3.2a. Within a certain range of values of the applied field, there exists a point on the axis, the internal field of which corresponds to $\frac{d\omega}{dk} = 0$ in the spin wave dispersion curve. This is the so-called "turning point" marked T in Fig. 3.2a, and is given by $H_i(z_{tp}) = \omega / |\gamma\mu_0|$; the quantity ω is the frequency of the input microwave power. The pulsed rf magnetic field generated by the input fine wire couples electromagnetic energy to spin wave energy at the turning point via magnetostatic waves,²⁴ giving rise to a spin wave packet (branch 1 with $k \rightarrow 0$ in Fig. 2.5). This wave packet then travels from the turning point toward the end of the rod with constant frequency and increasing wave number, accelerating as it encounters lower bias field values. As the wave packet reaches the region of coupling with longitudinal elastic waves (longitudinal crossover point marked L_{cros} in Fig. 3.2a), a fraction of the energy is converted into phonon form (i.e., stays on branch 1 in Fig. 2.5) and the rest stays in the magnon state (branch 2). According to Schlömann and Joseph,¹³ the fraction of energy which stays in the magnon state decreases when the ratio between the field gradient at the crossover region $H'(z_{cros}^l)$ and the critical gradient $H_{crit}^{'l}$ increases. The latter is given by:¹²

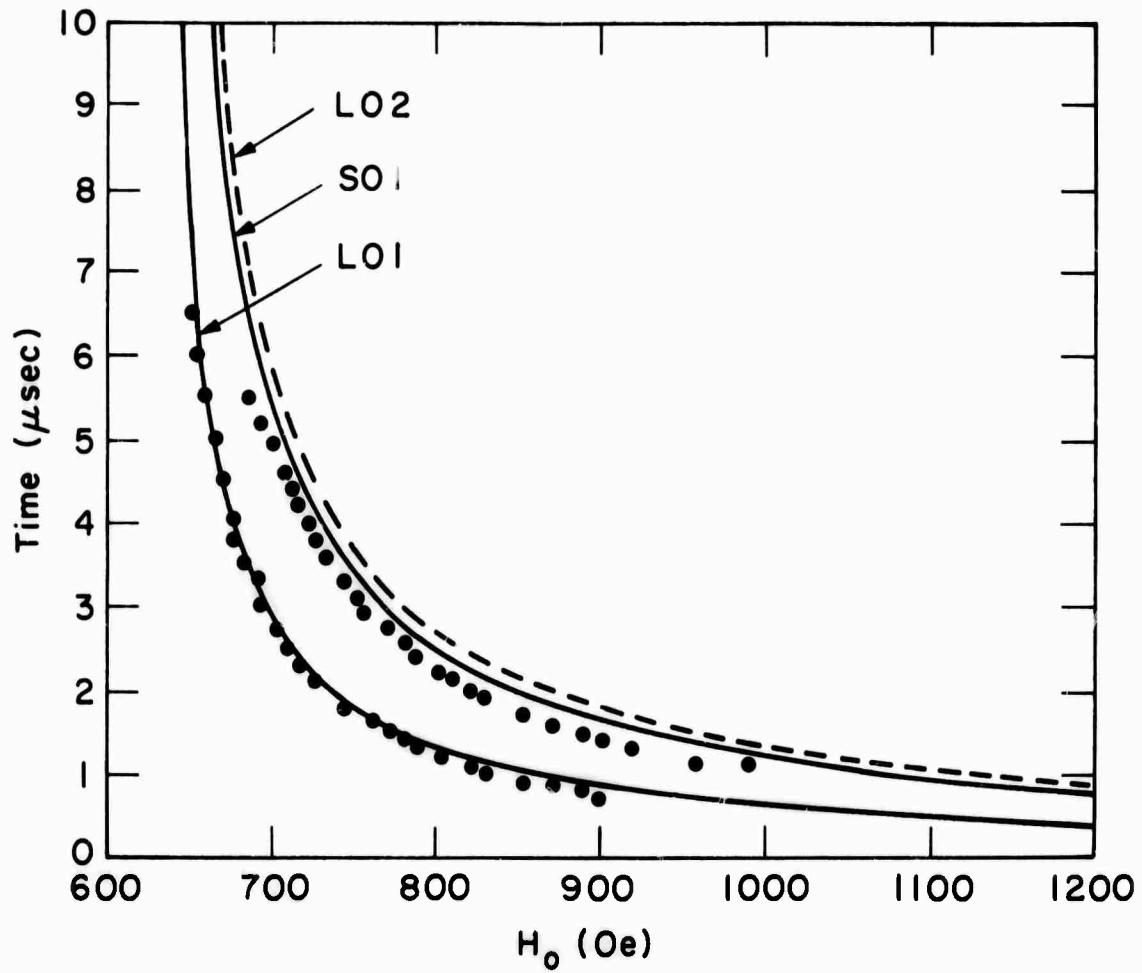
$$H_{crit}^{'l} = \frac{\pi}{2|\gamma\mu_0|} b_l^2 / v_l \quad (3.2a)$$

Similarly for the shear waves, the critical gradient $H_{crit}^{'s}$ is given by:

$$H_{\text{crit}}^{\text{'s}} = \frac{\pi}{2|\gamma\mu_0|} b_s^2 / v_s \quad (3.2b)$$

For values of the applied field such that the longitudinal crossover region is near the center of the rod (small gradient), most of the magnon energy excited at the turning point is converted into longitudinal phonon energy, which is reflected at the end of the rod and therefore returns to the turning point. The energy which remains in the magnon state is later converted almost completely (because of the large shear critical gradient) into shear elastic form (at the shear crossover region marked S_{cros} in Fig. 3.2a) to give rise to another reflected echo. If the applied field is increased so that the crossover regions move toward the rod end, the spatial field gradient at the longitudinal crossover region increases and the fraction of the energy which is scattered to branch 2 increases, resulting in a gradual trade-off between the amplitudes of the longitudinal and shear wave echoes. Over the range of echo time delay (0.8 to 6.5 sec) we have been able to employ, the spatial gradient of the field at the longitudinal crossover region varies from about the value of the critical gradient to ten times larger. This allows the measurement of the magnon-phonon conversion efficiency versus field gradient in ranges not attainable before. The results are reported in section 3.3b. Typical data of delay time τ versus dc magnetic field of the first longitudinal and shear echoes obtained at 1.5 GHz are shown in Fig. 3.3 together with the theoretical curves calculated with the assumption of zero frequency splittings at the crossover points. The latter is given by:²⁵

$$\tau = 2 \left(\frac{z_{\text{tp}}}{2} + \frac{f}{v_p |\gamma\mu_0| H'(z_{\text{tp}})} \right) \quad (3.3)$$



$[22.5^\circ]$ rod, $f = 1.5$ GHz

Fig. 3.3 Measured time delay of the first longitudinal (L01) and shear (S01) echoes versus dc magnetic bias fields at 1.5 GHz.

where v_p (phonon velocity) is either v_ℓ (longitudinal phonon velocity) or v_s (shear phonon velocity) as appropriate, z_{tp} is the distance measured from the end surface to the turning point, $f(= \frac{\omega}{2\pi})$ is the frequency of the input microwave power, and $H'(z_{tp})$ is the field gradient at the turning point T. As can be seen, the agreement is very good for the longitudinal elastic waves.

Further endorsement of the interpretation given to the observed echoes is provided by experiments with pulsed bias magnetic fields. The oscillograms of Fig. 3.4 illustrate some typical results. The lower traces represent the video-detected microwave pulses from the superheterodyne receiver and the upper traces show the current steps applied to the coil wound around the sample, and both traces are synchronous. In Fig. 3.4(a) the first longitudinal and shear echoes can be seen with delays of 2.0 and 3.6 sec, respectively, corresponding to a static applied field of 735 Oe. (Notice for this applied field strength, at the unsaturated rod end, the magnetoelastic wave is dominated by elastic wave characteristics and hence hardly affected by the unsaturated magnetic medium. However, in the neighborhood of turning point and crossover points where the medium is essentially saturated, the magnetoelastic wave is dominated by spin-wave characteristics and hence the theory is still applicable.) The insertion loss of the longitudinal echo is 50 db. Higher-order echoes from longitudinal and shear branches which are discussed in the next section can also be seen at small delays. In Fig. 3.4(b) a 10 Oe positive field step is applied when the branch 1 wave is on a return trip as a magnon (i.e., toward the point T in Fig. 3.2a) and the branch 2 wave is still in the shear elastic state (i.e., near the end surface in Fig. 3.2a; notice also that the

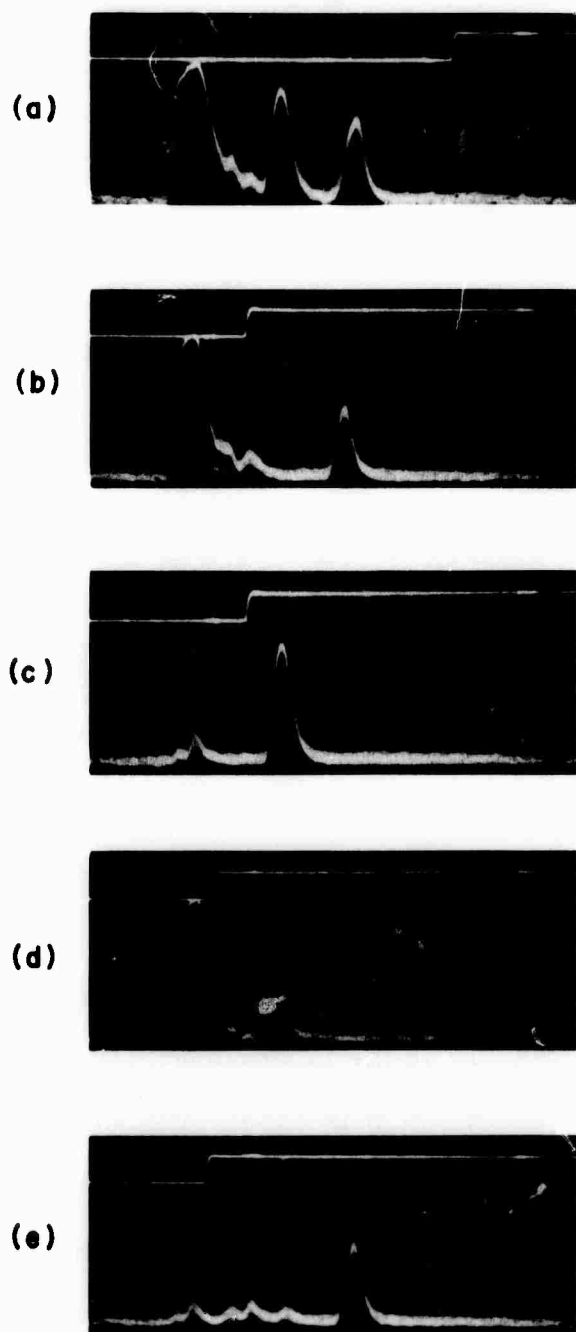


Fig. 3.4 Magnetoelastic echoes affected by a pulsed magnetic bias field. The first pulse in each lower trace is due to leakage; the second and third are, respectively, the longitudinal (L01) and shear (S01) magnetoelastic echoes (time scale 1 $\mu\text{sec}/\text{cm}$). A full explanation of cases (a) - (e) is given in the text.

receiver delays the echoes by $0.3 \mu\text{sec}$, so that the scope traces show the field steps advanced with respect to the echo time scale). The result is that the field step produces a frequency-shifted echo, because the spin waves subjected to a pulse field undergo a frequency shift with constant wavenumber,⁸ while the phonon-like branch 2 wave is virtually unaffected. In Fig. 3.4(c) the local oscillator is retuned to receive only the frequency-shifted echo. In Fig. 3.4(d) the field step is applied when the branch 1 wave is in the longitudinal elastic state (away from the point L_{cros} in Fig. 3.2(a)) and the branch 2 wave is in the magnon from (at the position between L_{cros} and S_{cros}) resulting in a frequency shift of the latter. In Fig. 3.4(e), the recovery of the frequency-shifted pulse is shown.

3.2b Identification of Echoes

In addition to the two echoes due to longitudinal and shear elastic/spin waves shown in Fig. 3.4, there are a number of echoes whose spacings change in an orderly manner as a function of the strength of the applied field H_0 . This is quite analogous to what Strauss and Eggers,²⁶ using an experimental arrangement similar to that of Spencer et al.,²⁷ have observed; they reported, in a $\langle 111 \rangle$ YIG rod, pulse sequences associated with both shear elastic and shear elastic/spin wave propagation. In our case, however, there are many more pulse sequences because of the presence of both longitudinal and shear magnetoelastic coupling. A typical echo pattern from reflection measurements, using the wide-band detection system, is shown in Fig. 3.5. Following Strauss,²⁶ let T_{ijkl} denote the arrival time of reflected echoes for an input pulse at $t = 0$. The observed pulses then arrive at the times

$$T_{ijkl} = 2i T_{EL} + j T_{SL} + 2k T_{ES} + l T_{SS} \quad (3.4)$$

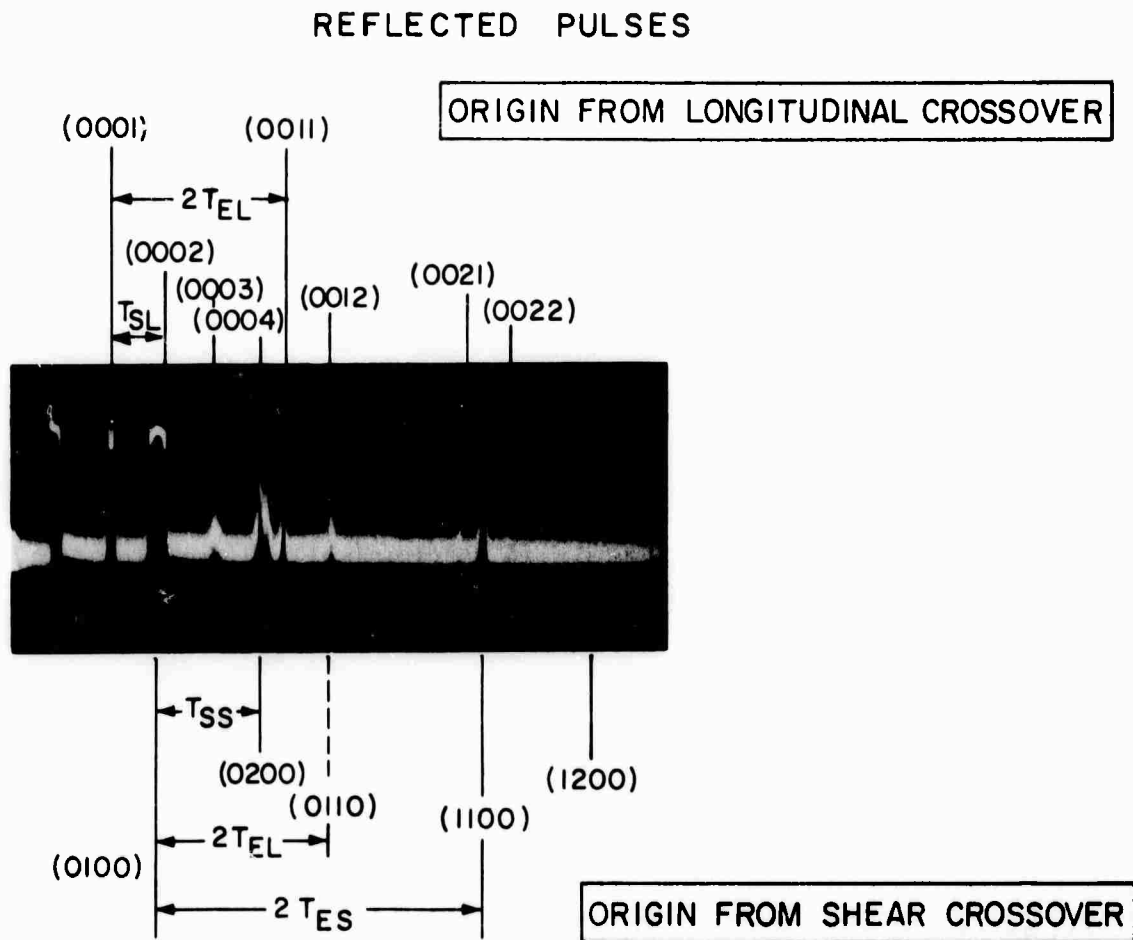


Fig. 3.5 A typical magnetoelastic echo pattern observed with one-port fine wire excitation. The first pulse in the trace is due to leakage; the other two pulses are due to the longitudinal and shear magnetoelastic coupling (time scale $1 \mu\text{sec/cm}$). A full explanation is given in the text.

where

$$i = 0, 1, 2, 3, \dots$$

$$j = 1, 2, 3, \dots$$

$$k = 0, 1, 2, 3, \dots$$

$$\ell = 1, 2, 3, \dots$$

The quantity T_{ES} is the time taken by a shear elastic wave to travel the length of the rod, T_{SS} the round trip time of flight of a shear elastic/spin wave from and back to the turning point, T_{EL} and T_{SL} the corresponding times for the longitudinal waves. There are two sequences of echoes, one originating from the longitudinal crossover point, the other the shear crossover point, as indicated in Fig. 3.5 and Fig. 3.6. Each sequence consists of a primary pulse ($j = 1$ or $\ell = 1$) followed by satellite pulses of smaller amplitudes ($j, \ell = 2, 3, \dots$). As the external magnetic field is varied at a fixed frequency, the spacing between the primary pulses remains constant (i. e., $2T_{ES}$ and $2T_{EL}$), but the spacings between the satellite pulses and the primary pulses in different sequences change. Indeed, the behavior of the pulse spacings as a function of H_0 permits the identification of the various echoes. In particular, in the sequence originating from the shear crossover point, the echo (0110) (the dashed line in Fig. 3.6) starts as a shear elastic/spin wave from the shear crossover point S_{cros} , converts to a longitudinal elastic wave at the longitudinal crossover point L_{cros} on its return trip from the end surface, and finally, after traversing the length of the rod, returns back to the turning point (Fig. 3.2(a)). Since the internal field profile is concave downward, the corresponding echo (1001) does not exist.

The echo sequence (00k ℓ) can be interpreted as due to incomplete conversion between branch 1 and branch 2 in Fig. 2.5 at the longitudinal

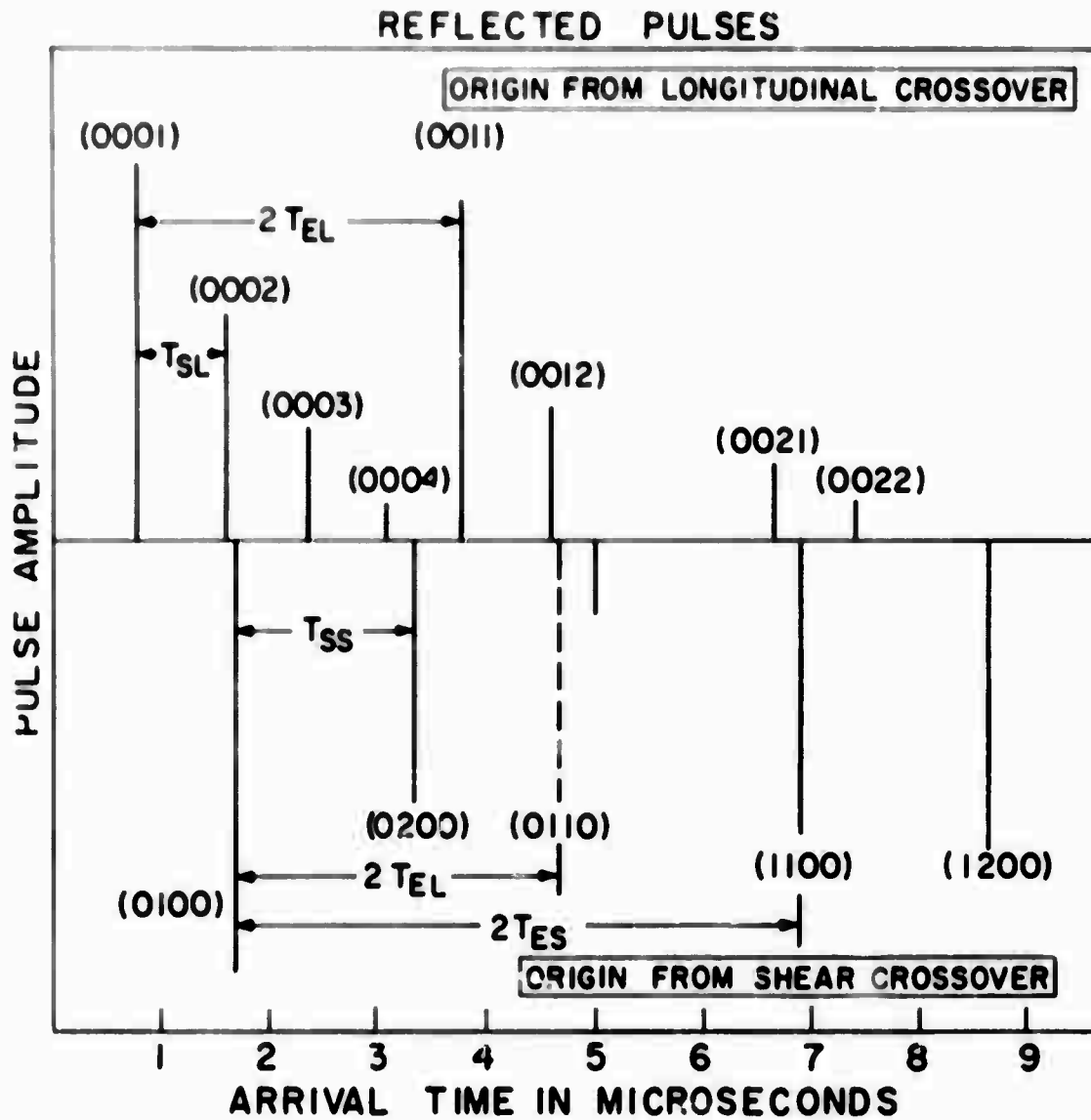


Fig. 3.6 An echo pattern of Fig. 3.5, reconstructed from theoretical considerations.

crossover point. The echo sequence (ij00) corresponds to what Strauss and Eggers²⁶ have reported. While they suggested that the origin of the sequence they observed is due to the polarization reversal of the elliptically polarized shear elastic waves at the end surface of the (111) YIG rod, we do not understand very well about the origin of the sequence (ij00) we observed in the "22.5°" YIG rod.

3.3 Experiments with Acoustically Injected Longitudinal Elastic/Spin Waves

3.3a Propagation of Longitudinal Elastic/Spin Waves in Spatially Varying Magnetic Fields

The room temperature experiments were performed using a YIG bar which measured 4 mm x 4 mm x 12 mm and had its long axis oriented along the "22.5°" direction mentioned earlier. A longitudinal elastic wave packet at 1.5 GHz, 100 nsec duration, was launched using a sputtered ZnO thin film piezoelectric transducer. For $H_0 < H_C^l$, where H_C^l is the applied field value for which the longitudinal crossover point L_{cros} in Fig. 3.2(b) is at the middle of the long axis ($z = 0$ in this case), the wave character becomes more spin-like as the wave propagates toward the center of the bar. The delay difference τ'_{SL} between the longitudinal elastic/spin waves and the longitudinal elastic wave can be calculated by:

$$\tau'_{\text{SL}} = 4 \int_0^{L/2} \frac{dz}{v_g} - \frac{2L}{v_l} \quad (3.5)$$

where the group velocity of the longitudinal elastic/spin wave v_g (of branch 1 in Fig. 2.5) can be derived from the dispersion relation in Eq. (2.34). Numerical integration of (3.5) for the YIG bar yields the curve for the delay difference and group velocity versus applied magnetic

fields shown in Fig. 3.7. Notice the extremely small range of H_0 required for the change of wave character from longitudinal elastic to spin-like, compared to that of shear waves.⁸ This is expected because the magnetoelastic coupling of the longitudinal waves is approximately two orders of magnitude smaller than that of the shear waves. Experimentally it was also observed that the longitudinal elastic/spin waves, unlike the shear ones, did not experience appreciable changes of the delay time because the change of group velocity is too abrupt to be easily observed (Fig. 3.7).²⁰ In fact, the wave packets only showed some wave-form distortion because of dispersion, as shown in Fig. 3.8. In Fig. 3.8(g) and the lower traces of Fig. 3.8(h), (i) and (j), the input power has been increased by 13 db to show the distorted wave-form. The quantity H_C^ℓ pertaining to Fig. 3.8 is estimated to be 716 Oe and is within 6% of the theoretical calculation. For $H_0 \geq H_C^\ell$, i.e., when the longitudinal crossover point is inside the bar, strong Bragg infrared light scattering from spin waves has been observed and will be described in Chapter V. For $H_0 > H_C^\ell$, branch hopping between the upper branch (branch 1 in Fig. 2.5) and lower branch (branch 2 in Fig. 2.5) takes place (Fig. 3.8, (h) to (p)). We have taken advantage of this fact to measure the spatial spin/elastic wave conversion to be described in the next section.

3.3b Spatial Longitudinal Elastic/Spin Wave Conversion Efficiencies¹⁹

In this section we present the results of direct measurements of the longitudinal elastic/spin wave conversion efficiencies at room temperature in a single crystal, axially magnetized YIG rod; the rod used here is identical to the one described in section 3.2.

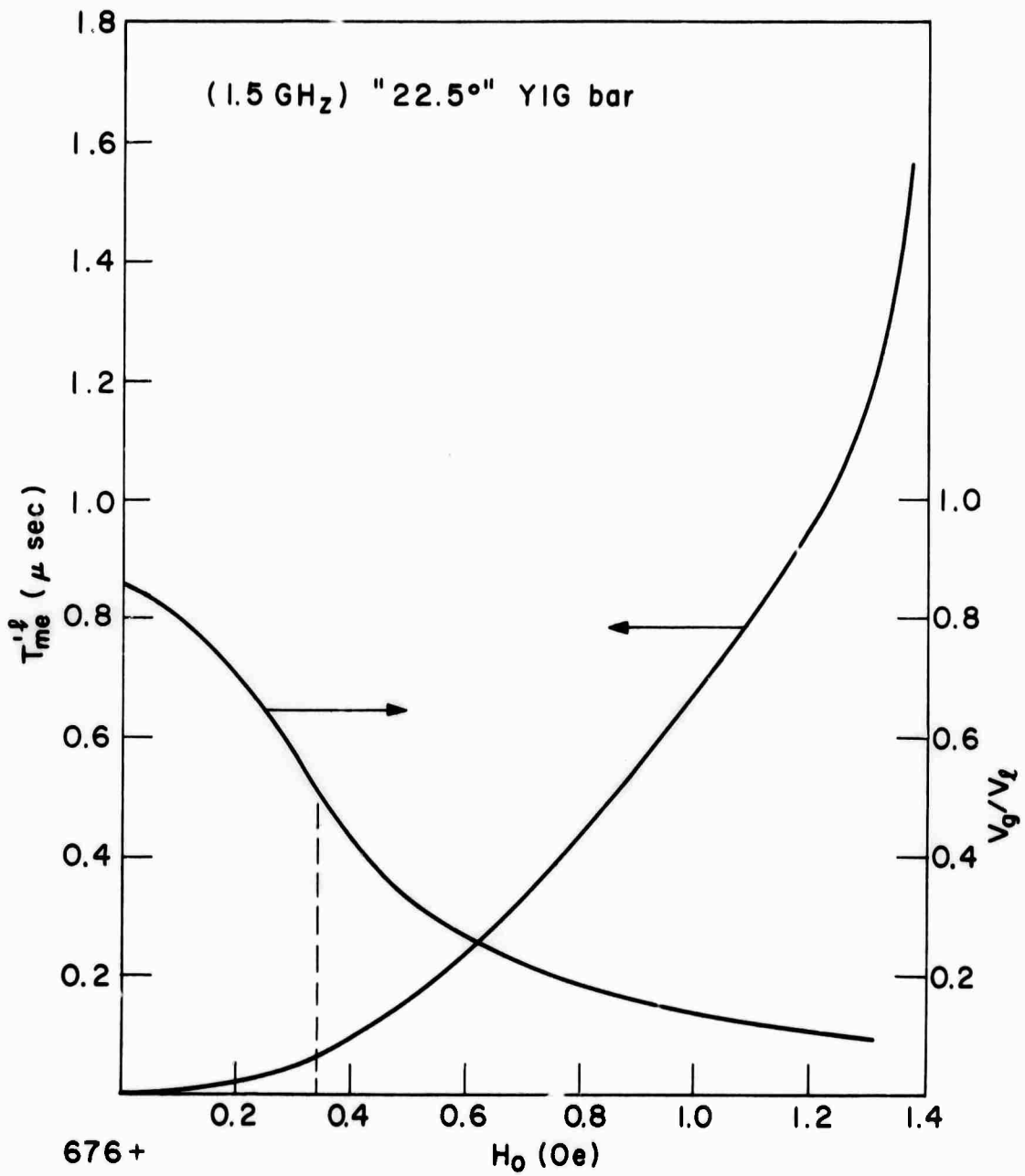


Fig. 3.7 Delay of elastically injected longitudinal elastic/spin wave packet and group velocity at the bar center as a function of applied magnetic field for a "22.5°" YIG bar which measures 4 mm x 4 mm x 12 mm.

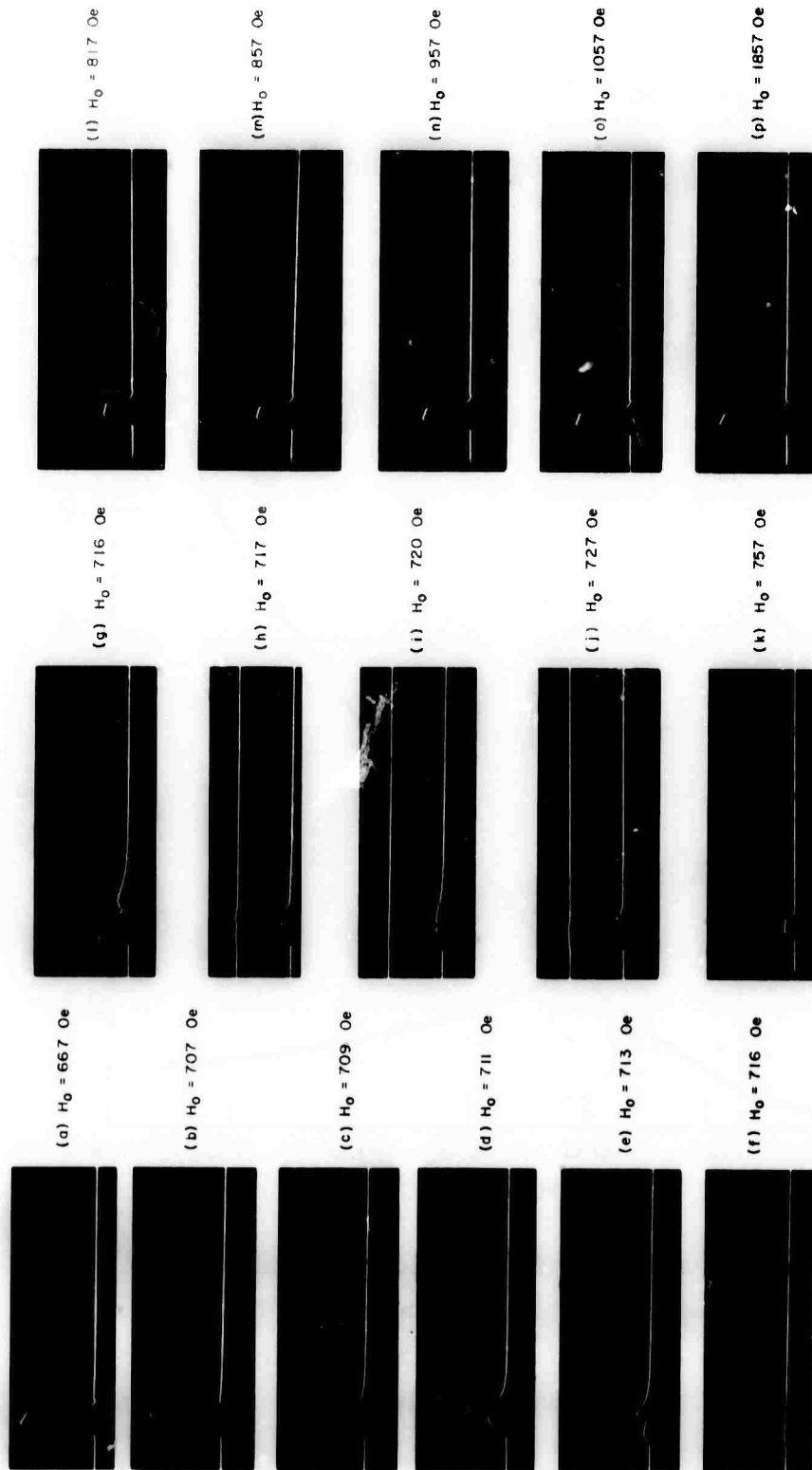


Fig. 3.8 The distortion of a longitudinal elastic/spin wave packet, which is excited and detected by a ZnO transducer, as a function of external applied magnetic field (time scale $0.1 \mu\text{sec/cm}$).

Although shear elastic/spin wave conversion has been studied theoretically by previous authors,^{11, 21} experimental investigation has been limited to the case of nearly complete conversion.^{10, 25, 28} This is due to the fact that critical field gradients H'_{crit}^s of shear elastic/spin waves (Eq. (3.2b)) in YIG are much larger than those obtainable in practice, while that, H'_{crit}^l of the longitudinal magnetoelastic splitting (Eq. (3.2a)) are much smaller and well within the reach of our experiments.

We have used two different ways to measure the conversion efficiencies, one with magnetic injections in which only the weak coupling region can be investigated, and another with acoustical injections, in which case nearly the entire range of interactions was covered; the results in both cases are in reasonable agreement with the previous theory.

I. Experiments with Magnetic Injections

The experimental arrangement is identical to that described in section 3.2a. The mechanism of the wave propagation has also been described in detail there. It is sufficient to say here that when the spin wave originating at a turning point first reaches the longitudinal cross-over point (marked L_{cros} in Fig. 3.2a), a fraction of the energy is converted into phonon form and the rest remains in the magnon state. The conversion efficiency was first studied by Schlömann and Joseph¹¹ and later also by Kirchner et al.²¹ Their results indicate that the conversion efficiency η is related to the field gradient $H'(z_{cr})$ at a crossover point in the following manner:

$$\eta = 1 - e^{-\frac{H'_{crit}}{|H'(z_{cr})|}} \quad (3.6)$$

where H'_{crit} is the critical field gradient for either longitudinal and shear waves (Eqs. (3.2)) and $H'(z_{\text{cr}})$ is the field gradient at either longitudinal (z_{cr}^{ℓ}) or shear crossover point (z_{cr}^s). In our YIG rod, at 1.5 GHz and room temperature, the critical gradients for longitudinal and shear waves are, respectively, 225 and 28,500 Oe/cm. The trade-off between the amplitudes of the longitudinal and shear wave echoes described earlier in section 3.2a can best be described in terms of longitudinal elastic/spin wave conversion efficiency η^{ℓ} in the following equation:

$$\left[\frac{(1 - \eta^{\ell})}{\eta^{\ell}} \right]^2 = \frac{P_S}{P_L} \exp[2(T_{SS} - T_{SL}) \frac{\alpha}{4.343}] \quad (3.7)$$

where P_S/P_L is the power ratio between shear and longitudinal elastic/spin wave echoes, $2T_{SS}$ and $2T_{SL}$ are, respectively, the total time spent in the magnon state for shear and longitudinal elastic/spin waves, and α is the magnon loss (in db) per unit time. We have neglected the phonon loss which is very small. Figure 3.9 shows the measured results, using $\alpha = 12 \text{ db}/\mu\text{sec}$ (full spin-wave linewidth 0.16 Oe) to fit the theoretical curve.²¹ Here the field gradients have been determined using the well-known Sommerfeld formula in Eq. (3.1a). Although the field strengths applied in the experiment were fairly low (from 650 to 1200 Oe) the assumption that the magnetization of the YIG rod is saturated by the applied fields is in reasonable agreement with the argument given previously in section 3.2a. Note that the experimental points fluctuate about the theoretical value. The fluctuation of the amplitudes of the magnetoelastic echoes, both longitudinal and shear, has been observed experimentally, but its origin is not yet understood. The trade-off between the amplitudes of the longitudinal and shear elastic/spin wave is vividly demonstrated in Fig. 3.9. However, the

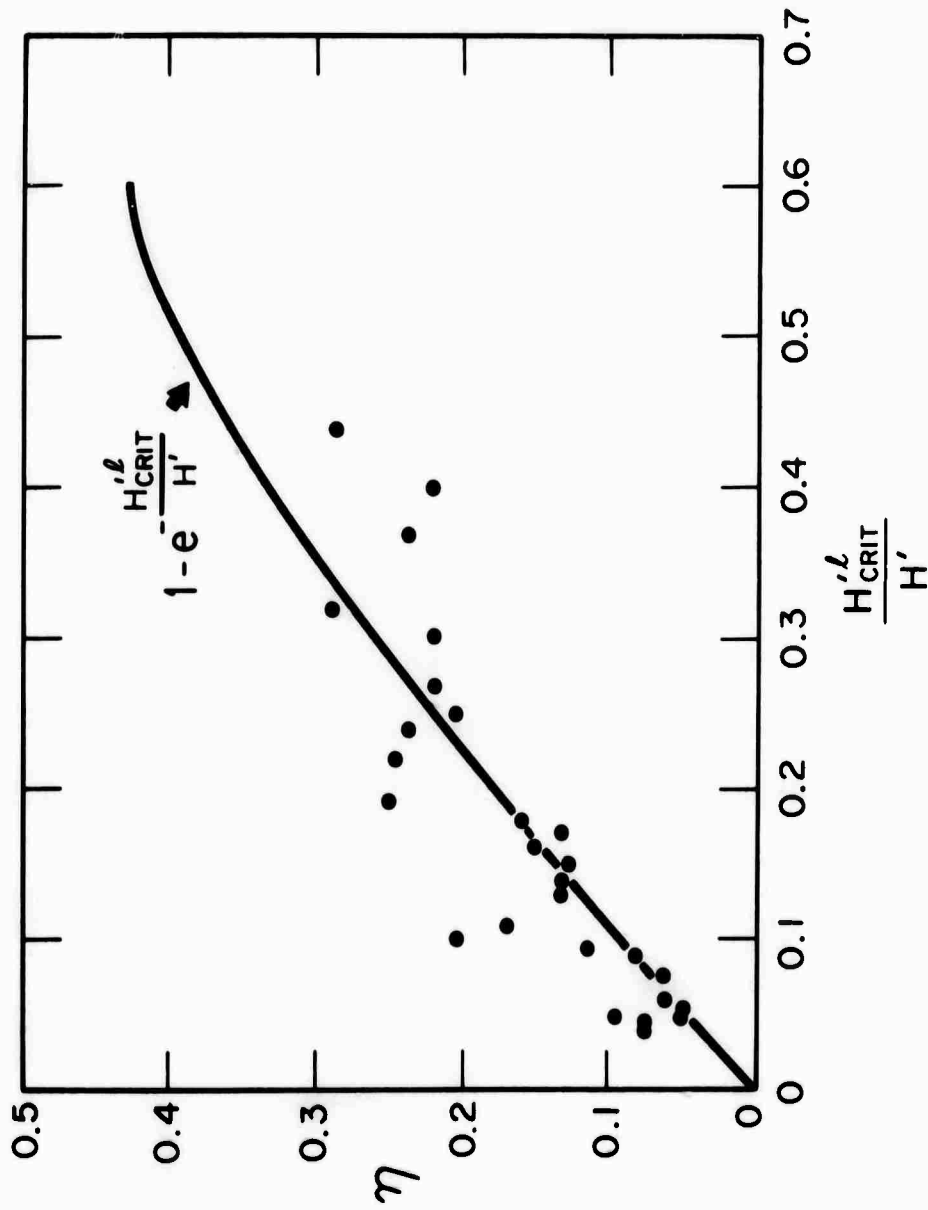


Fig. 3.9 Magnetoelastic (magnon-phonon) conversion efficiency versus inverse spatial magnetic field gradient obtained with spin wave injection.

excessive magnon loss prevents us from going to the strong coupling region in this type of experiment, because a small spatial field gradient (therefore a strong coupling) causes excessive attenuation due to long magnon delays. Nevertheless, we have managed to measure the conversion efficiency in a strong coupling region by using acoustically injected longitudinal elastic/spin waves.

II. Experiments with Acoustically Injected Longitudinal Elastic/Spin Waves

In order to obtain the conversion efficiency throughout the entire range of the interaction, experiments using acoustical injections were carried out. The room temperature experiments were also performed at 1.5 GHz using a ZnO transducer bonded to one of the two polished rod end surfaces. The longitudinal acoustic echoes were observed as a function of the strength of applied field H_0 . In both the low and high magnetic field values, where the magnetoelastic interaction is small, the amplitude of the echo is marked. As the magnetic field increases from zero to a point where the longitudinal crossover region is placed in the middle of the rod, i.e., $H_0 = H_c$, the elastic echo disappears (or rather is attenuated by more than 30 db) as a result of (almost) complete conversion into spin waves. A further increase of the magnetic field moves the crossover region toward the end of the rod, thus also increasing the spatial field gradients. The longitudinal elastic/spin wave conversion efficiency starts to decrease, as observed by the increase of the amplitude of the longitudinal elastic wave echoes (refer to traces (h) to (p) in Fig. 3.8). In addition, very weak spin/longitudinal elastic echoes were also observed. Therefore, by measuring the attenuation of the first longitudinal elastic echo as a

function of the magnetic field strength, one obtains the conversion efficiencies in nearly the entire range of the interaction. Since there are actually two longitudinal crossover points in an axially-magnetized rod, a longitudinal elastic disturbance makes conversion to spin waves at four occasions in making a round trip throughout the rod. The experimental results are plotted in Fig. 3.10, where use has been made of

$$P_o = P_i (1 - \eta^l)^4 \quad (3.8)$$

Again the field gradients have been determined using the Sommerfeld formula in Eq. (3.1a). The quantity P_i is the power of the longitudinal elastic waves in the absence of the magnetoelastic interaction and P_o is the one with interaction. The result indicated in Fig. 3.10 is in fair agreement with the theory.

3.3c Propagation of Longitudinal Elastic/Spin Waves in Temporally Varying Magnetic Fields

Frequency shifts and pulse compression of the wave packets subject to pulsed magnetic fields are discussed below.

Measurements of the frequency shifts of longitudinal elastic/spin waves subjected to both positive and negative pulsed fields were made using the axially magnetized YIG bar described earlier in section 3.3a. A polycrystal YIG bar with identical saturated magnetization was attached to one end of the single crystal YIG bar to reduce the field gradients inside the sample, while a thin film ZnO transducer was sputtered on the other polished end surfaces. Positive frequency shifts of up to 3 MHz, and negative frequency shifts of down to 1 MHz have been observed with a 95 Oe/Amp coil wound around the composite

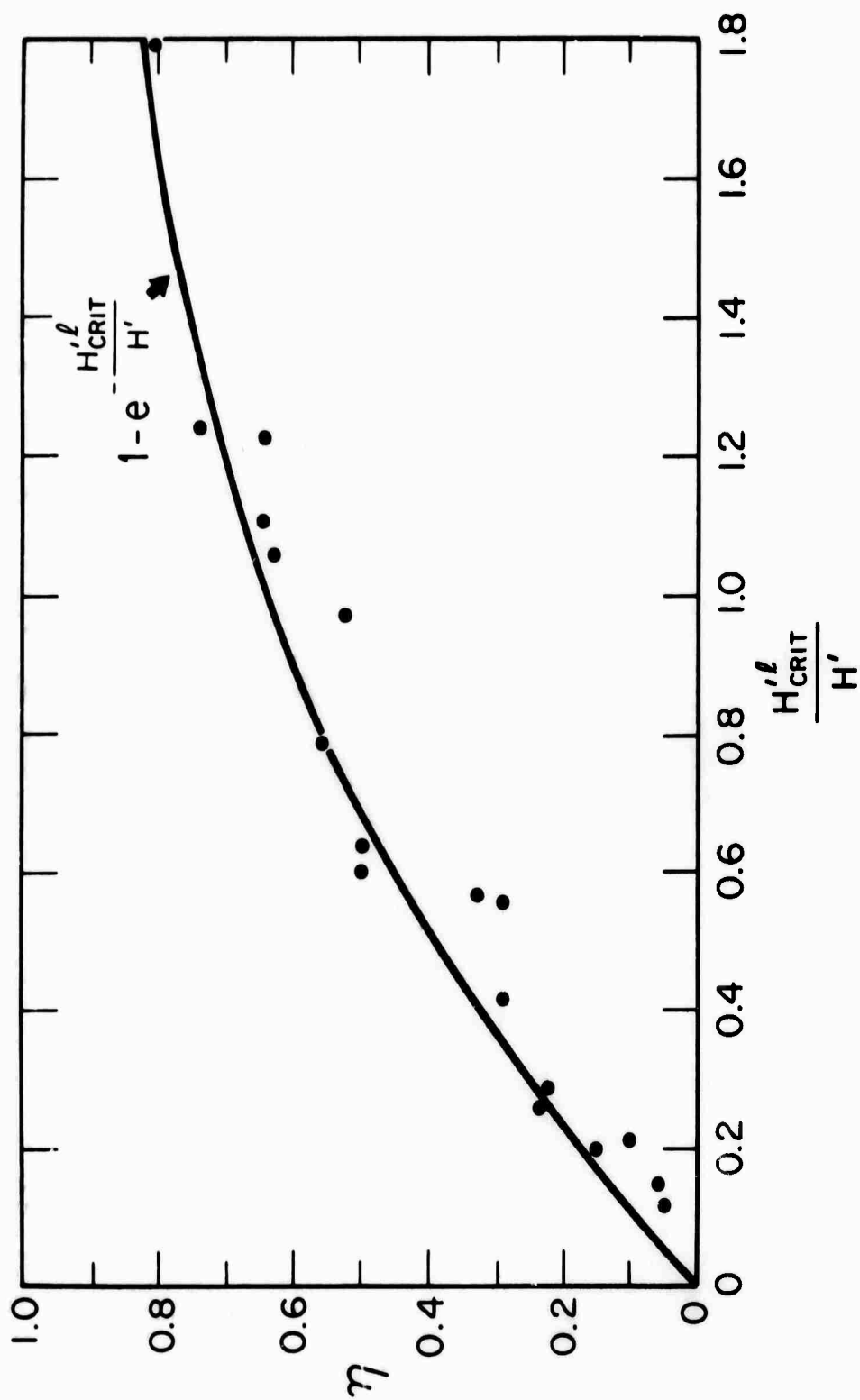


Fig. 3.10 Magnetoelastic (magnon-phonon) conversion efficiency versus inverse spatial magnetic field gradient obtained with acoustic wave injection.

structure. The frequency shifts were observed with a Tektronix IL 20 spectrum analyser used to study the first longitudinal elastic echo which was gated. The small longitudinal magnetoelastic coupling makes the frequency modulation effect of the spatially non-uniform internal fields (with this composite structure) much stronger than in the case of shear waves.¹⁸ Consequently no very meaningful quantitative data have been obtained.²⁹

Pulse expansion and pulse group velocity modulation⁸ with the longitudinal elastic/spin again was not successful. The failure is believed to be due to the same causes that complicate the frequency shift measurements, as stated above, i.e., non-uniform internal fields and the comparative smallness of the longitudinal magnetoelastic coupling.

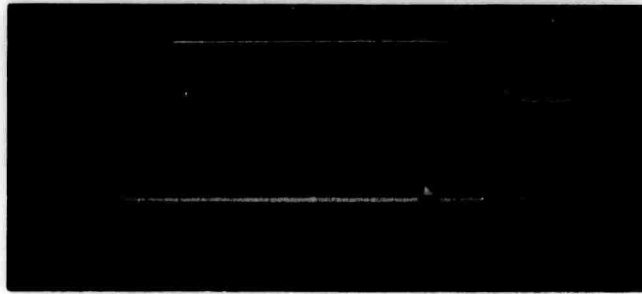
Pulse compression of up to 10 db (considerably larger than with shear waves⁸) has been achieved when the strength of the applied field is either $H_0 < H_c$ or $H_0 > H_c$. The mechanism of pulse compression with acoustic wave injections can be described in the following manner. A longitudinal elastic wave packet of spatial length ΔL_i (and duration $\Delta T_i = \Delta L_i / v_l$) is generated by the ZnO transducer at the rod end. As it propagates toward the center of the rod of increasing magnetic fields at fixed frequency but variable wavenumbers, its character becomes more spin-like, its spatial length shortens because of its decreasing group velocity, but its duration ΔT_i remains unchanged. When a negative pulsed field that opposes the dc magnetic field is applied, then the duration of the wave packet suddenly decreases (hence pulse compression) as its group velocity increases abruptly to that of longitudinal elastic waves v_l . The duration ΔT_f of the compressed pulse can be found according to:

$$\Delta T_f = \frac{v_g}{v_l} \Delta T_i \quad (3.9)$$

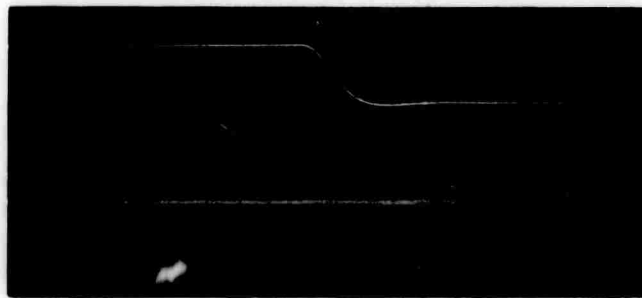
where v_g is the group velocity of the elastic/spin wave packet at the time the pulsed field is applied. Equation (3.9) can also be derived from consideration of the Fourier spectra of the wave packet in wavenumbers and frequencies. Notice that Eq. (3.9) indicates that the pulse compression ratio ($\Delta T_i/\Delta T_f$) is always larger for the case of longitudinal waves than for the shear wave case.

A typical case in which $H_0 > H_c$ is shown in Fig. 3.11. The lower trace of Fig. 3.11(a) indicates a longitudinal elastic echo which has gone through both crossover points inside the sample. The upper trace of Fig. 3.11(a) indicates a negative field pulse of 80 Oe that opposes the dc bias field. In Fig. 3.11(b), the field pulse is applied after the wave train has been reflected from the free end of the bar and returned to the crossover point between the center and the free end of the bar. In this case only the trailing edge is compressed since the trailing edge is still spin-like (on branch 1 in Fig. 2.5), while the leading edge has hopped (to branch 2 in Fig. 2.5) and is therefore elastic-like. Similarly in Fig. 3.11(c), the field pulse is applied when the waves have left the transducer for the first time and reached the crossover point between the transducer end and the center of the bar. Again the trailing edge (on branch 1 in Fig. 2.5) is more spin-like than the leading one (on branch 2 in Fig. 2.5) and therefore is compressed. This kind of compression again illustrates the small longitudinal magnetoelastic coupling and the comparatively larger effect of non-uniform internal fields on the longitudinal waves as compared to the shear waves.

When $H_0 < H_c$, a typical case is shown in Fig. 3.12. In



(a)



(b)



(c)

Fig. 3.11 Pulse compression of longitudinal elastic/spin waves subjected to pulsed magnetic fields. The static magnetic field here is high enough so that there are crossover points inside the YIG bar (i.e., $H_0 > H_c$). Horizontal sweeps are from left to right with scale $0.5 \mu\text{sec/cm}$ (frequency 1.5 GHz).

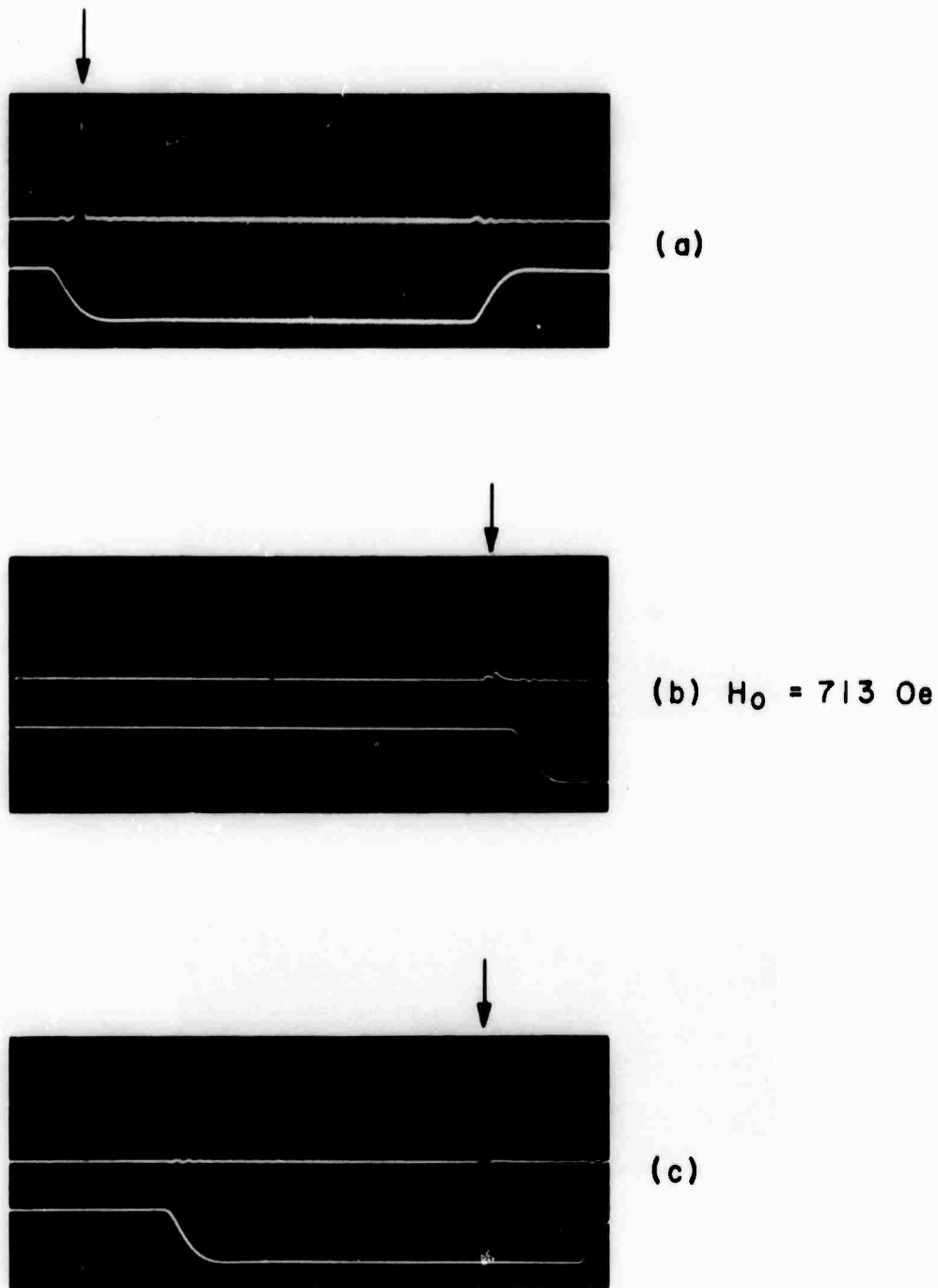


Fig. 3.12 Pulse compression of longitudinal elastic/spin waves subjected to pulsed magnetic fields, when $H_0 < H_c$. Horizontal sweeps are from left to right with scale $0.5 \mu\text{sec/cm}$ (frequency 1.5 GHz).

Fig. 3.12(a), the upper trace indicates the first longitudinal elastic echo (marked with an arrow) which emerged after passing through the length of the bar in the absence of longitudinal magnetoelastic coupling, and the lower trace shows the negative field pulse of 10 Oe that opposed the dc bias field. In Fig. 3.12(b), H_0 is increased so that the longitudinal elastic echo (marked with an arrow) has been strongly attenuated. In Fig. 3.12(c), the negative field pulse is applied just as the wave packet reaches the middle of the rod for the first time; therefore the longitudinal echo is compressed as a whole for a compression ratio of 10.

3.4 Preliminary Results on Longitudinal/Shear Elastic Wave Conversion via Spin Waves in Spatially Varying Fields

Comstock and Wigen³⁰ first proposed the spatial conversion from shear to longitudinal elastic waves, and vice versa, via spin waves in transversely magnetized rods. Morgenthaler³¹ also suggested longitudinal/shear elastic conversion via spin waves by means of time-varying magnetic fields. Experimental studies of these two cases have not yet appeared in the literature. Here we report some preliminary results on spatial longitudinal/shear elastic conversion via spin waves in axially magnetized single crystal YIG rod oriented along the " 22.5° " direction. The room temperature experimental arrangement is shown in Fig. 3.13, where a polycrystalline nickel ferrite rod with a saturation magnetization of 3000 Gauss is placed at one end of the YIG rod to obtain a monotonically increasing internal field profile. A decreasing field profile, however, exists at the end of the YIG rod near the air gap between the rods. A CdS thin film on each end of the rod served as an input shear wave and output longitudinal elastic wave transducer; the input transducer unfortunately does not have good discrimination against the

excitation of longitudinal elastic waves and therefore generates both shear and longitudinal waves at the same time. A shear elastic wave packet (and also a longitudinal one), launched at the input transducer, travels toward the center of the rod. When it reaches the shear crossover point (marked S_{cros} in Fig. 3.13 and corresponding to branch 2 in Fig. 2.5), it is nearly completely converted into spin waves; the latter then proceed to the longitudinal crossover (marked L_{cros} in Fig. 3.13), whereupon part of the energy is converted into longitudinal elastic waves (corresponding to staying in branch 2 in Fig. 2.5), which then move forward and reach the other transducer. The delay time τ_t can be deduced from Eq. (3.3) as:

$$\tau_t = \tau_E + \tau_S \quad (3.10a)$$

$$\tau_E = \frac{z_{\text{tp}}}{v_s} + \frac{L - z_{\text{tp}}}{v_l} \quad (3.10b)$$

$$\tau_S = \frac{f}{|\gamma\mu_O| H'_O(z_{\text{tp}})} \left(\frac{1}{v_s} - \frac{1}{v_l} \right) \quad (3.10c)$$

where τ_E is the time duration spent in the elastic wave state, while τ_S is the time duration spent in the spin wave state. The conversion efficiency $\eta_{S \rightarrow L}$ can be written as:

$$\begin{aligned} \eta_{S \rightarrow L} &= e^{-\tau_S \frac{\alpha}{4,343}} \left(1 - e^{-\frac{H_{\text{crit}}'^l}{|H'^l|}} \right) \left(1 - e^{-\frac{H_{\text{crit}}'^s}{|H'^s|}} \right) \\ &\cong e^{-\tau_S \frac{\alpha}{4,343}} \left(1 - e^{-\frac{H_{\text{crit}}'^l}{|H'^l|}} \right) \end{aligned} \quad (3.11)$$

where the phonon loss is neglected and α is the magnon loss (in db/nsec),

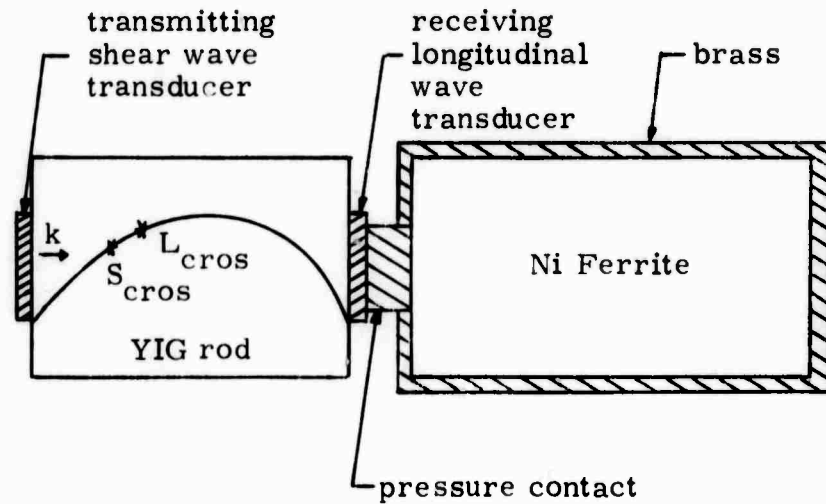


Fig. 3.13 Arrangement used to observe spatial conversion from shear elastic waves to longitudinal elastic waves via spin wave coupling.

H'^l the field gradient at the longitudinal crossover point, H'^s the corresponding shear one. Both the delay times and the conversion efficiencies as a function of H'^l are plotted in Fig. 3.14, using

$$\alpha = 5 \text{ db}/\mu\text{sec} \quad (3.13)$$

and the values of the critical field gradient are given in Eq. (3.2).

Notice that as the external field (and hence the field gradient) increases, the delay time approaches the time required for the elastic waves to traverse the length of the rod. Also there is a peak in the conversion efficiencies $\eta_{S \rightarrow L}$ corresponding to an optimum H' (or H_0). The experimental observations are shown in Fig. 3.15. Figure 3.15(a) shows the reflection echoes from the input transducer, where echoes marked L

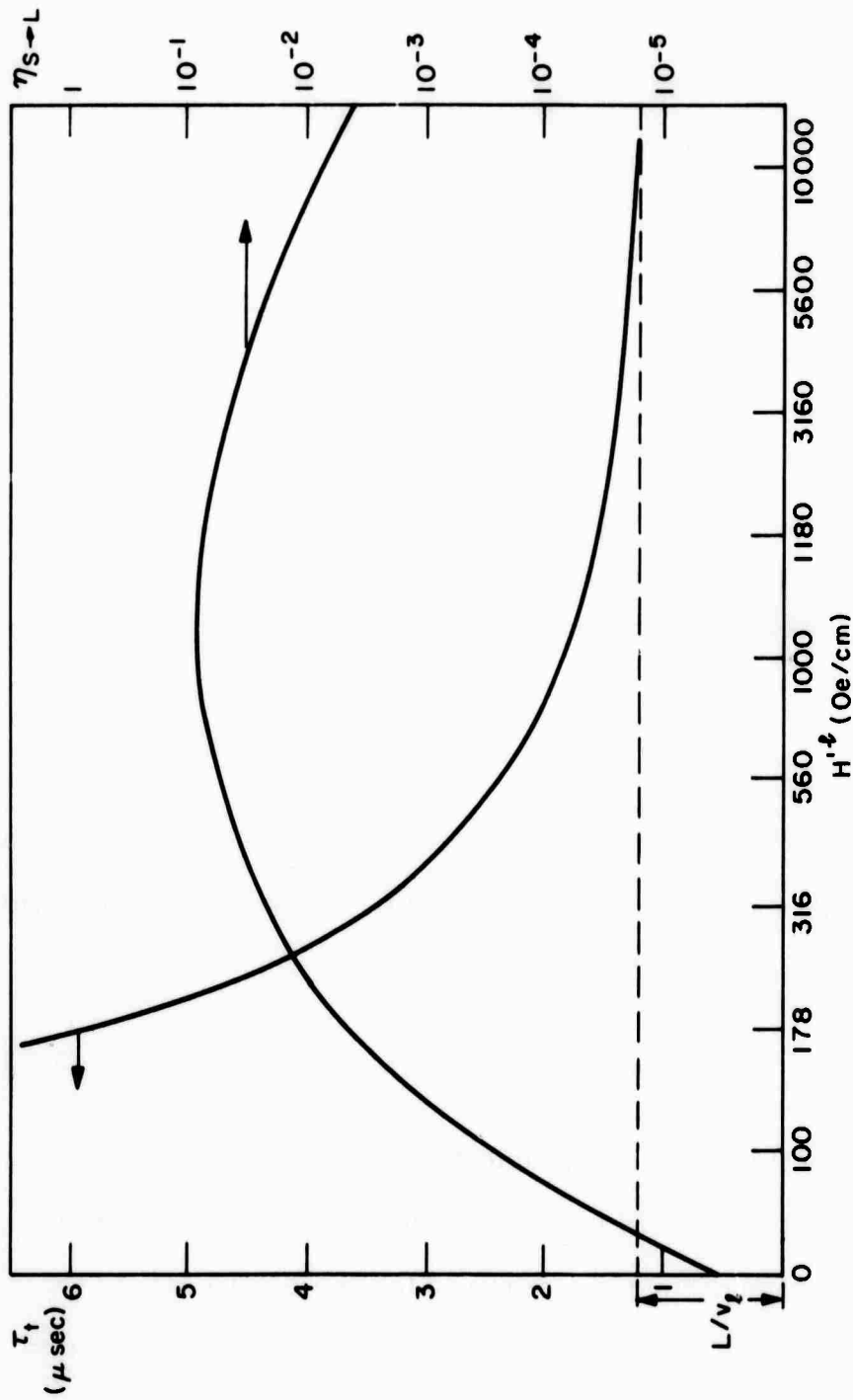


Fig. 3.14 Total delay time (τ_t) and spatial conversion efficiency ($\eta_{S \rightarrow L}$) from shear elastic waves to longitudinal elastic waves via spin wave coupling as a function of field gradient at the longitudinal crossover point.

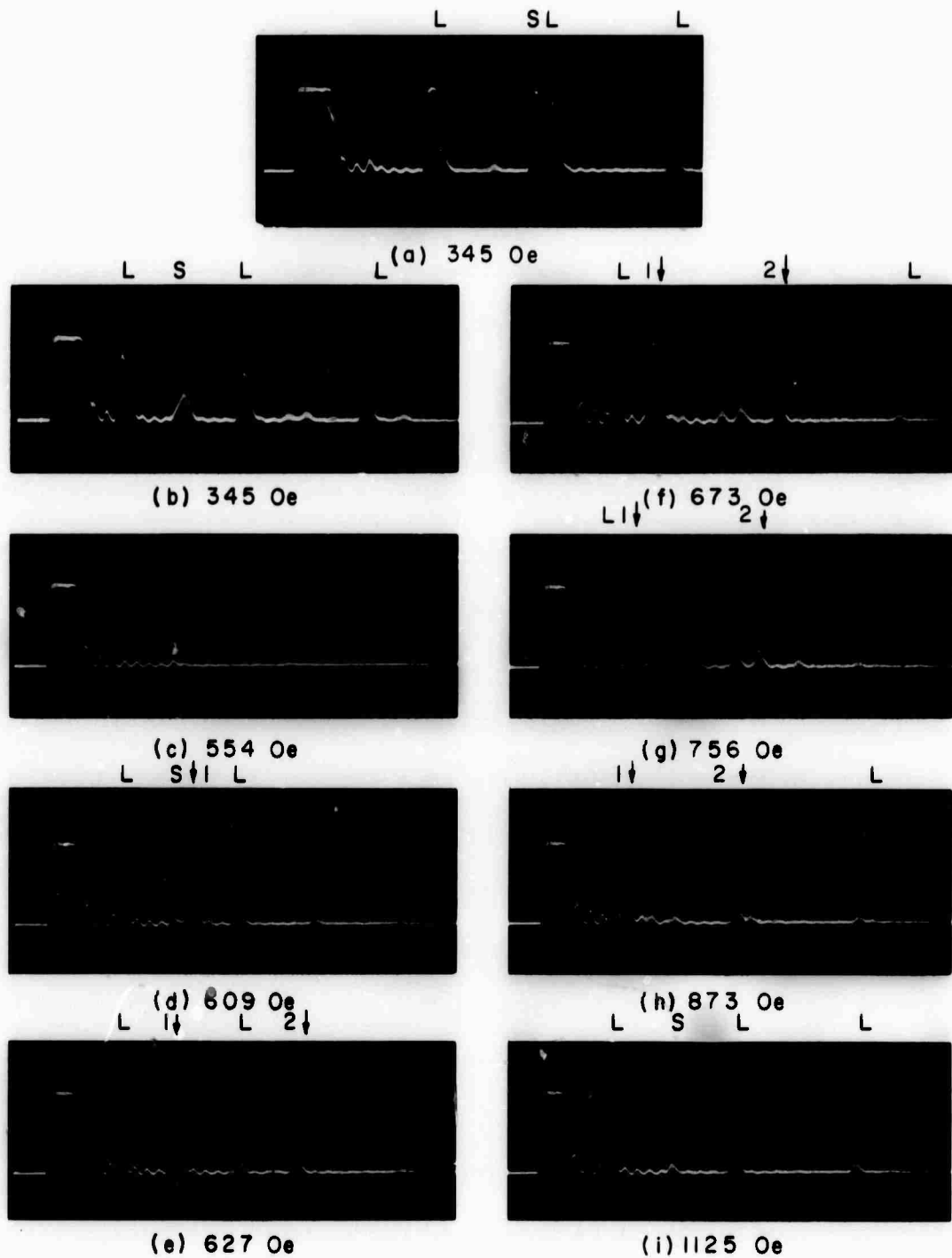


Fig. 3.15 Oscillograms showing the spatial conversion from shear elastic waves to longitudinal elastic waves via spin wave coupling. The horizontal traces are from left to right (time scale $1 \mu\text{sec/cm}$).

are longitudinal elastic ones while the echo marked S is the shear one. In Fig. 3.15, from (b) through (i), are the echo patterns picked up at the receiving transducer as a function of the external applied field H_0 . All the transmitted pulses marked either L or S are the purely elastic longitudinal or shear echoes. In Fig. 3.15(c), the crossover points come in the center of the rod and therefore almost all echoes except that corresponding to the shear one disappear as a result of conversion to spin waves. In Fig. 15, (d) through (e), there are two echoes marked by arrows; the first one (with 1 on the arrow) is believed to come from shear/longitudinal conversion and does show a maximum amplitude in (f) as predicted in Fig. 3.14; the second echo (with 2 on the arrow), which is always spaced at exactly one round trip time required for longitudinal elastic waves, is thought to come from the reflection of the first echo at the receiving transducer. In addition, notice from (h) and (i) that the first echo (with arrow marked 1) eventually approaches the transmitted longitudinal echo and these two echoes disappear at the same time when the fields are increased further, as in (i). Notice that the decreasing field profile at the receiving transducer end merely inflicts some additional loss. The loss is caused by the conversion from the transmitted longitudinal waves to spin waves at the longitudinal crosspoint near the receiving end.

We are unable to make any quantitative comparison with the theoretical curve in Fig. 3.14 because of the unknown internal field profile for this composite structure and the poor qualities of the transducers. However, we do not believe that these two echoes could come from the input longitudinal elastic waves for the following reason. In order to have variable delay times as a function of the external fields,

the longitudinal wave would have to make a round trip to and from the turning point plus a one-way trip as a longitudinal elastic wave from the transmitting transducer to the receiving one. In this case the waves would spend more time as spin waves, go through three times the longitudinal conversion point and therefore suffer more loss than the shear/longitudinal elastic waves mentioned earlier. Furthermore, we do not expect to see a maximum amplitude of the echo, such as in Fig. 3.15(f), for this case. For all these reasons, we believe the first echo, whose delay time varies with the external applied field, does come from shear/longitudinal elastic wave conversion via spin waves.

BLANK PAGE

CHAPTER IV

THEORY OF LIGHT DIFFRACTION FROM COHERENT ELASTIC AND SPIN WAVES

4.1 Introduction

Scattering of light by means of elastic waves in liquids and solids has been extensively studied since the effect was first predicted by Brillouin in 1922³² and observed by Gross³³ in 1930 in liquids where only longitudinal elastic vibrations are allowed. In 1932, Debye and Sears³⁴ and, independently, Lucas and Biquard,³⁵ performed the first successful diffraction of light from coherent ultrasonic waves. This phenomenon, light inelastically scattered from an acoustic elastic wave, has come to be known as Brillouin scattering, while light inelastically scattered from optical phonons, discovered in 1928 by C. V. Raman,³⁶ is known as Raman scattering. Early work on Brillouin scattering³⁷ was used to determine elastic constants and to study thermal phonon distributions in various materials. The advent of the laser in the sixties has greatly revived the interest in light scattering and made the technique useful to probe not only elastic waves but many other elementary excitations such as plasma waves and spin waves.

For Brillouin scattering, it is necessary to distinguish between diffraction at the Bragg angle (Bragg scattering) and Raman-Nath type scattering, after Raman and Nath³⁸ who explained the spatial form of the scattered light in the experiments of Debye and Sears and Lucas and Biquard. In Raman-Nath type scattering the light enters the medium parallel to the wavefronts of the elastic waves and the diffracted light appears on both sides of the primary beam in the form of equally spaced

lines. Willard³⁹ discussed the distinction between these two cases and showed that Bragg scattering results whenever the acoustic column is sufficiently wide such that the product of the optical wavelength in the medium (λ/n) and the acoustic beamwidth (w) is greater than the square of the acoustic wavelength (Λ) (i. e., $\frac{\lambda}{n} w > \Lambda^2$). Indeed, Rytov⁴⁰ has shown that the diffracted light will appear in a single spot and will be a maximum when the light is incident at the Bragg angle. This is also indicated in Brillouin's original work, and it is the only case with which this thesis will be concerned. There have been many excellent review articles on Brillouin scattering, on its theories,⁴¹⁻⁴⁸ its application as a research tool,⁴⁹⁻⁵⁵ and its practical applications such as in optical signal processing.⁵¹⁻⁵⁵

In this chapter, the main objective is to review the theory of light scattering and generalize it to include the theory of coherent light scattering from coherent spin waves. The generalized theory presented here has essentially revised Auld and Wilson's (A-W) calculations⁵⁶ by using the perturbed dielectric tensor, which is linear in small signal spin wave amplitudes rather than in total crystal magnetization. It appears to explain adequately not only our experimental results described in Chapter V, but also observations that previous authors^{57, 58} reported as "anomalous," unexplained by A-W theory.

Our new theory indicates that the characteristics of light scattering from coherent spin waves are quite different from scattering from elastic waves. Unlike the case of coherent elastic waves, the scattered light intensity from coherent spin waves is found to be dependent on both the incident light polarization and the sign of the frequency shift (Stokes or anti-Stokes lines). Also the intensity is independent of the direction

of the applied magnetic field.

The chapter begins with a rather extensive review of the macroscopic theory of light scattering, followed by a description of the characteristics of light scattering from coherent elastic waves. Finally, the theory of coherent spin wave light scattering is presented.

Because of convention and convenience in comparing with the optics literature, the c.g.s. unit system is used throughout this and the next chapter.

4.2 The Macroscopic Theory of Light Diffraction

Before starting our discussion, a few words regarding magneto-optics in general are appropriate here. Following Landau and Lifshitz,⁵⁹ Pershan⁶⁰ discussed in great detail that fact that, especially at optical frequencies, the propagation of an electromagnetic wave in any material can always be described in terms of an effective dielectric permittivity ϵ^{eff} and $\mu = 1$. This ϵ^{eff} , which incorporates whatever magnetic characteristics a particular material has, can be defined in the following manner. Maxwell's equations in c.g.s. unit system for a nonconducting and current-free medium are:

$$\nabla \times \vec{E} = -\frac{1}{c} \frac{\partial \vec{H}}{\partial t} - \frac{4\pi}{c} \frac{\partial \vec{M}}{\partial t} \quad (4.1a)$$

$$\nabla \times \vec{H} = \frac{1}{c} \frac{\partial \vec{E}}{\partial t} + \frac{4\pi}{c} \frac{\partial \vec{P}}{\partial t} \quad (4.1b)$$

$$\nabla \cdot (\vec{E} + 4\pi \vec{P}) = \nabla \cdot (\epsilon \vec{E}) = 0 \quad (4.1c)$$

$$\nabla \cdot (\vec{H} + 4\pi \vec{M}) = 0 \quad (4.1d)$$

where \vec{H} , \vec{E} are the magnetic and electric field vectors. The vectors \vec{M} and \vec{P} are the magnetization and polarization of the medium and c is the

velocity of light in free space; the quantity ϵ is the dielectric constant of the medium.

From Eqs. (4.1a) and (4.1b), one obtains

$$\frac{1}{c^2} \frac{\partial^2}{\partial t^2} \vec{E} - (\nabla \times \nabla \times \vec{E}) = \frac{4\pi}{c^2} \frac{\partial \vec{J}^{\text{eff}}}{\partial t} \quad (4.2a)$$

where

$$\vec{J}^{\text{eff}} = \frac{\partial \vec{P}}{\partial t} + c \nabla \times \vec{M} \quad (4.2b)$$

Equations (4.2) indicate that the effect of the magnetization can be incorporated with an effective current density \vec{J}^{eff} . Therefore one may define an effective dielectric susceptibility $\vec{\chi}^{\text{eff}}$ which takes account of the effect of magnetization M as

$$\vec{J}^{\text{eff}} = \frac{\partial}{\partial t} (\vec{\chi}^{\text{eff}} \cdot \vec{E}) \quad (4.3a)$$

An effective polarization \vec{P}^{eff} then is defined as:

$$\vec{P}^{\text{eff}} = \vec{\chi}^{\text{eff}} \cdot \vec{E} \quad (4.3b)$$

Similarly, an effective dielectric tensor $\vec{\epsilon}^{\text{eff}}$ is then defined as:

$$\vec{\epsilon}^{\text{eff}} = \vec{I} + 4\pi \vec{\chi}^{\text{eff}} \quad (4.3c)$$

Substituting Eq. (4.3a) into Eq. (4.2a), one obtains

$$\left(\nabla^2 - \frac{1}{c^2} \frac{\partial^2}{\partial t^2} \right) \vec{E}(\vec{r}, t) = -\nabla (\vec{E} \cdot \nabla \ln \epsilon) + \frac{4\pi}{c^2} \frac{\partial^2 \vec{P}^{\text{eff}}(\vec{r}, t)}{\partial t^2} \quad (4.4)$$

where use has been made of $\nabla \cdot \vec{E} = -\vec{E} \cdot \nabla \ln \epsilon$. Notice that Eq. (4.4) can also be obtained from Eq. (4.1) directly by setting $\vec{M} = 0$ (or $\mu = 1$) and $\vec{P} = \vec{P}^{\text{eff}}$. This means that whatever effect the magnetization has is included in the effective dielectric susceptibility $\vec{\chi}^{\text{eff}}$ or tensor $\vec{\epsilon}^{\text{eff}}$.

A more detailed account has been given by Pershan.⁶⁰

If we consider $\vec{E}(\vec{r}, t)$ in Eq. (4.4) as a superposition of plane waves of wavelength λ/n , and the elastic or spin waves are of wavelength Λ , the term $\nabla(\vec{E} \cdot \ln \epsilon)$ is of the order $\delta\epsilon \frac{\lambda}{\Lambda}$ times the term $\nabla^2 \vec{E}$. Under usual experimental conditions, $\delta\epsilon$ (the change of ordinary dielectric constant) is much smaller than unity, and $\frac{\lambda}{\Lambda}$ at most of the order of unity. This term can usually be safely neglected. Then we have

$$\left(\nabla^2 - \frac{1}{c^2} \frac{\partial^2}{\partial t^2}\right) \vec{E}(\vec{r}, t) = \frac{4\pi}{c^2} \frac{\partial^2 \vec{P}(\vec{r}, t)}{\partial t^2} \quad (4.5)$$

It is important to recognize that the medium contains as many as 10^9 atoms in a region as small as a cube of the light wavelength and therefore can be regarded essentially as a continuum. A light wave passing through such a medium produces an effective polarization \vec{P}^{eff} at the point \vec{r}' . This polarization, in turn, radiates or scatters electromagnetic energy in all directions. Suppose we are interested only in the radiation in the far field (Fraunhofer region). From Eq. (4.5), the electric field $d\vec{E}^d$ scattered (or diffracted) at point \vec{r} by the effective polarization \vec{P}^{eff} within a volume $(d^3 r') \ll (\lambda/n)^3$ is:^{41, 61}

$$d\vec{E}^d(\vec{r}, t) = \frac{1}{c^2} \left[\frac{\vec{i}_{|\vec{r}-\vec{r}'|} \times (\vec{i}_{|\vec{r}-\vec{r}'|} \times \frac{\partial^2 \vec{P}^{\text{eff}}(\vec{r}', t')}{\partial t'^2})}{|\vec{r} - \vec{r}'|} \cdot d^3 r' \right]_{t' = t - \frac{|\vec{r}-\vec{r}'| n_d}{c}} \quad (4.6)$$

where \vec{r} , \vec{r}' and the unit vectors $\vec{i}_{|\vec{r}-\vec{r}'|}$ and \vec{i}_r are shown in Fig. 4.1. The quantity $t' (= t - \frac{|\vec{r}-\vec{r}'| n_d}{c})$ is the retarded time, c is the light velocity in free space given before and n_d is the index of refraction pertaining to the diffracted electric field in the medium. For simplicity we have taken the field point \vec{r} to be within the medium. If it is outside the medium, one may find the field there by using the laws of refraction at the

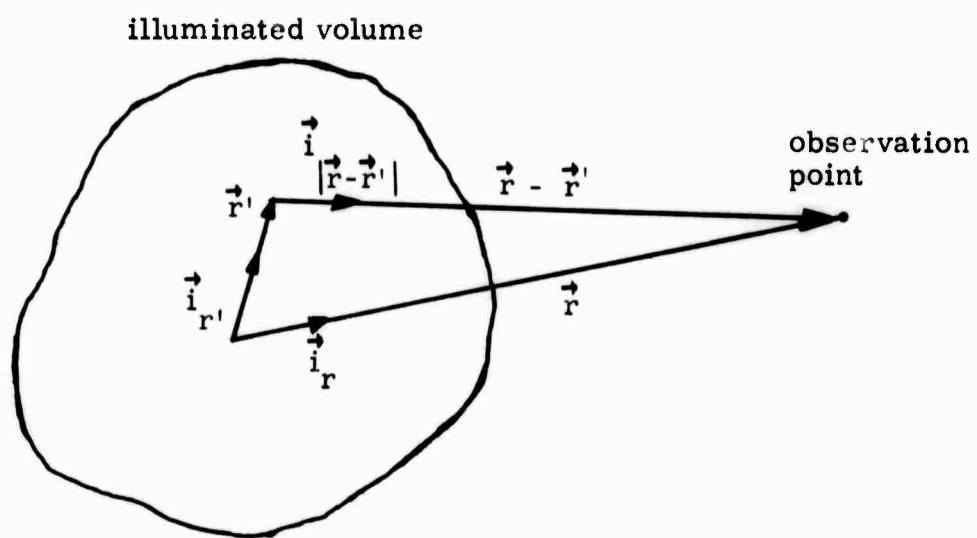


Fig. 4.1 Radiation from an illuminated volume.

boundaries. However, one must be aware of the fact that sometimes there may be additional contributions to the scattered electric field dE^d from the multiple reflection of the undiffracted light at the boundaries.⁶²

The electric field of a monochromatic incident light of frequency ω_L and wavevector \vec{k}_L within the medium can be written as:

$$\vec{E}^i(\vec{r}, t) = \vec{E} e^{j(\omega_L t - \vec{k}_L \cdot \vec{r})} \quad (4.7a)$$

where

$$k_L = \frac{2\pi n_i}{\lambda} = \frac{n_i \omega_L}{c} \quad (4.7b)$$

and n_i is the index of refraction pertaining to the incident electric field \vec{E}^i inside the medium. In general, when the polarization of the incident light is different from that of the diffracted light, $n_i \neq n_d$. The quantity \vec{P}^{eff} in Eq. (4.6) is to be found by substituting the total (incident and diffracted) electric field \vec{E} into Eq. (4.3b). However, since $\vec{\chi}^{eff}$ is modulated slightly by coherent elastic waves or spin waves and the interaction between light and coherent elastic waves and spin waves is very weak, one may approximate \vec{E} in Eq. (4.3b) with the incident electric field \vec{E}^i in Eq. (4.7a) only (the "Born approximation," well known in scattering theory⁶³). From Eqs. (4.3b) and (4.7a), one obtains the polarization \vec{P}^{eff} at point \vec{r}' as:

$$\vec{P}^{eff}(\vec{r}', t') = [\langle \vec{\chi}^{eff} \rangle + \delta \vec{\chi}^{eff}(\vec{r}', t')] \cdot \vec{E}^i e^{j(\omega_L t' - \vec{k}_L \cdot \vec{r}')} \quad (4.8)$$

where $\langle \vec{\chi}^{eff} \rangle$ is the time average part, and $\delta \vec{\chi}^{eff}$ the modulated part of the effective susceptibility. Since $\delta \vec{\chi}^{eff}(\vec{r}', t')$ is usually modulated by a sinusoidal elastic (or spin) wave, it can be decomposed into the Fourier spectra of the elastic (or spin) wave:

$$\delta \vec{\chi}^{\text{eff}}(\vec{r}, t) = \int d^3k \delta \vec{\chi}^{\text{eff}}(\vec{k}) \chi_k(\vec{r}') e^{j(\pm\omega(k)t - \vec{k} \cdot \vec{r})} \quad (4.9)$$

where $|\vec{k}| = \frac{2\pi}{\Lambda}$ and $\omega(\vec{k})$ are, respectively, the wavelength and frequencies of the coherent elastic or spin modes; the quantity $\chi_k(\vec{r}')$ is the transverse profile of the mode \vec{k} ; the \pm sign is placed in front of $\omega(k)$ to account for the degeneracy in the dispersion relation for positive and negative angular frequencies. Equation (4.8) and Eq. (4.9) are to be substituted in Eq. (4.6) to evaluate the diffracted electric field \vec{E}^d . A further simplification may be made when one realizes that the frequencies of microwave elastic waves (or spin waves) are very small ($\leq 10^{10}$ Hz) compared to the light frequency ($\sim 10^{14}$ Hz). Therefore one may approximate $\partial^2 \vec{P}^{\text{eff}} / \partial t^2$ in Eq. (4.5) as:

$$\frac{\partial^2 \vec{P}^{\text{eff}}}{\partial t^2} \cong -\omega_L^2 \vec{P}(\vec{r}', t') \quad (4.10)$$

On substituting Eqs. (4.8), (4.9) and (4.10) into Eq. (4.6), and integrating over the illuminated volume V , one obtains:

$$\begin{aligned} \vec{E}^d(\vec{r}, t) = & -\frac{\omega_L^2}{c^2} \vec{r} \times \left\{ \left[\vec{r} \times \int d^3k \left(\delta \vec{\chi}^{\text{eff}}(\vec{k}) \vec{E}_0^i \frac{e^{j[\omega_L \pm \omega(k)t - \vec{k}_L' \cdot \vec{r}]}}{r} \right) \right] \right. \\ & \left. \int_V \chi_k(\vec{r}') \vec{E}(\vec{r}') e^{-j(\vec{k}_L - \vec{k}_L' + \vec{k}) \cdot \vec{r}} d^3r' \right\} \end{aligned} \quad (4.11)$$

where the term arising from $\langle \chi \rangle$ is dropped and $\vec{E}^i = \vec{E}_0^i \vec{E}(\vec{r}')$; $\vec{E}(\vec{r}')$ accounts for the profile of the light beam. We have used the fact that if $|\vec{r}| \gg |\vec{r}'|$, then

$$\vec{r}_{|\vec{r}-\vec{r}'|} \cong \vec{r}$$

$$\vec{k}'_L = \frac{n_d}{c} (\omega_L \pm \omega(k)) \vec{i}_r$$

$$\frac{n_d \omega_L}{c} |\vec{r} - \vec{r}'| \cong \frac{n_d \omega_L}{c} \vec{i}_r \cdot (\vec{r} - \vec{r}')$$

$$|\vec{r} - \vec{r}'| \cong |\vec{r}| \text{ in the denominator of Eq. (4.6)}$$

Using the fact that $\delta \vec{\epsilon}^{\text{eff}} = \frac{1}{4\pi} \delta \vec{\chi}^{\text{eff}}$ from Eq. (4.3c), one rewrites Eq. (4.11) as:

$$\vec{E}^d(\vec{r}, t) = -\left(\frac{\omega_L^2}{4\pi c^2}\right) \vec{i}_r \times \left[\vec{i}_r \times \int d^3k \frac{D \cdot \vec{Q}}{r} \right] \quad (4.12a)$$

where

$$\vec{Q} = \delta \vec{\epsilon}^{\text{eff}}(\vec{k}) \cdot \vec{E}_0^i e^{j[(\omega_L \pm \omega(k)t) - \vec{k}'_L \cdot \vec{r}]} \quad (4.12b)$$

$$D = \int e^{-j(\vec{k}_L - \vec{k}'_L + \vec{k}) \cdot \vec{r}'} E(\vec{r}') \chi_k(\vec{r}') d^3r' \quad (4.12c)$$

The vector product $(\vec{i}_r \times \vec{i}_r \times)$ merely ensures that the diffracted light is polarized perpendicular to the vector \vec{i}_r ; the vector \vec{Q} determines the scattering light amplitude; the diffraction integral, D , the diffraction pattern. The diffraction pattern has been discussed by McMahon,⁶⁴ Gordon⁶⁵ and others.⁶⁶ In our case, assuming both $E(\vec{r}')$ and $\chi_k(\vec{r}')$ are constant throughout a volume much larger than optical wavelength, we immediately obtain the phase matching (momentum conservation) conditions:

$$\vec{k}'_L = \vec{k}_L \pm \vec{k} \quad (\omega'_L = \omega_L \pm \omega) \quad (4.13)$$

However, assuming a small illuminated rectangular volume $a \times w' \times c$ (the interaction geometry is shown in Fig. 4.2), and that the incident light is almost parallel to the wavefronts of the elastic or spin waves

($\theta_B \approx 0$ in Fig. 4.2), the diffraction pattern \vec{D} at the observation point \vec{r} can be written as:

$$D = a w' c D_1 D_2 D_3 \quad (4.14)$$

where the observation point \vec{r} is at a small angle α from the y-axis and β from y-z plane, and use has been made of:

$$\vec{k}_L = \vec{i}_y k_L \cos \theta_B - \vec{i}_z k_L \sin \theta_B \quad (4.15a)$$

$$\vec{k}'_L = \vec{i}_x k'_L \sin \beta + \vec{i}_y k'_L \cos \beta \cos \alpha + \vec{i}_z k'_L \cos \beta \sin \alpha \quad (4.15b)$$

$$\vec{k} = \vec{i}_z k \quad (4.15c)$$

The quantities D_1 , D_2 and D_3 are given by:

$$D_1 = \frac{\sin(\frac{1}{2} k'_L a \sin \beta)}{\frac{1}{2} k'_L a \sin \beta} \quad (4.16a)$$

$$D_2 = \frac{\sin[\frac{1}{2}(k'_L \cos \beta \cos \alpha - k_L \cos \theta_B)w']}{\frac{1}{2}(k'_L \cos \beta \cos \alpha - k_L \cos \theta_B)w'} \quad (4.16b)$$

$$D_3 = \frac{\sin[\frac{1}{2}(k'_L \cos \beta \sin \alpha + k_L \sin \theta_B - k)c]}{\frac{1}{2}(k'_L \cos \beta \sin \alpha + k_L \sin \theta_B - k)c} \quad (4.16c)$$

As expected, the Fraunhofer diffracted field pattern in Eq. (4.14) resembles the Fourier transform of the illuminated rectangular volume. In Eqs. (4.16), the familiar term $\frac{\sin \Sigma}{\Sigma}$ is maximum when $\Sigma = 0$. One then obtains:

$$\begin{aligned} k'_L a \sin \beta &= 0 \\ k'_L \cos \beta \cos \alpha - k_L \cos \theta_B &= 0 \\ k'_L \cos \beta \sin \alpha + k_L \sin \theta_B &= k \end{aligned} \quad (4.17)$$

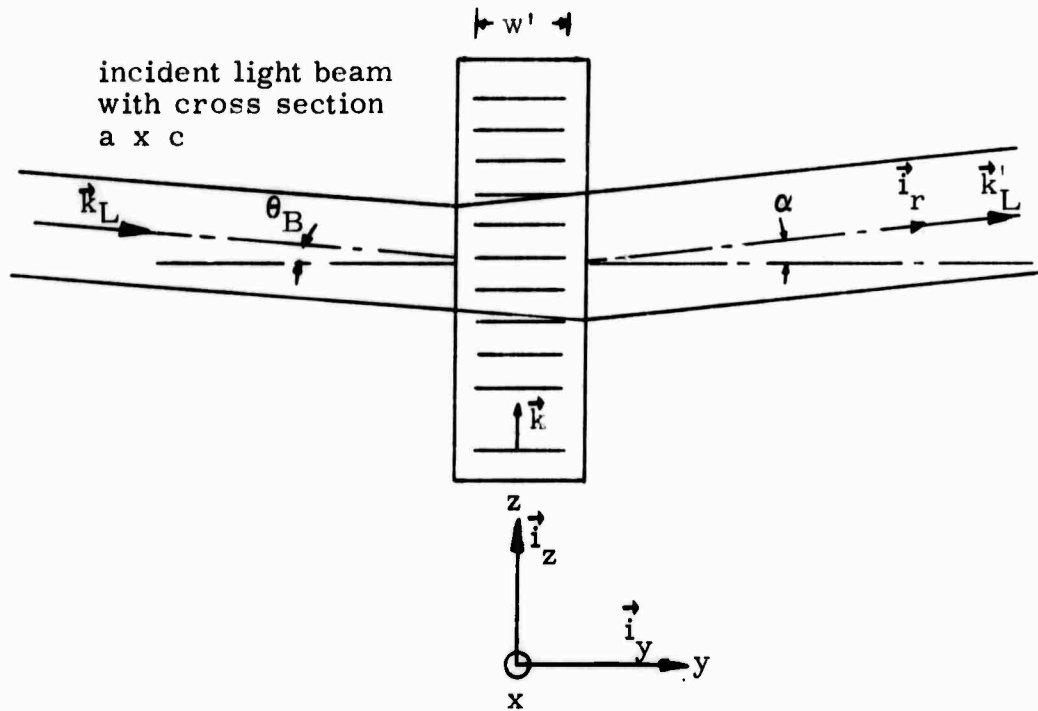


Fig. 4.2 Geometry of light diffraction.

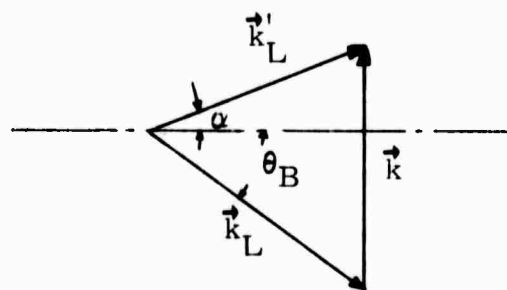


Fig. 4.3 Bragg condition for $\vec{k}'_L = \vec{k}_L + \vec{k}$.

or

$$\begin{aligned}\beta &= 0 \\ k'_L \cos \alpha - k_L \cos \theta_B &= 0 \\ k'_L \sin \alpha + k_L \sin \theta_B &= k\end{aligned}\tag{4.18}$$

Equations (4.18) can be represented geometrically in Fig. 4.3 and can easily be solved as:⁶⁷

$$\sin \theta_B = \frac{\lambda}{2 n_i \Lambda} \left[1 + \frac{\Lambda^2}{\lambda^2} (n_i^2 - n_d^2) \right]\tag{4.19a}$$

$$\sin \alpha = \frac{\lambda}{2 n_d \Lambda} \left[1 + \frac{\Lambda^2}{\lambda^2} (n_i^2 - n_d^2) \right]\tag{4.19b}$$

where $k_L = \frac{2\pi n_i}{\lambda}$, $k'_L = \frac{2\pi n_d}{\lambda}$ and $k = \frac{2\pi}{\Lambda}$ have been used. Notice that we have neglected the small difference in length between \vec{k}_L and \vec{k}'_L . In the case when $n_i = n_d = n$, the usual Bragg condition, Eq. (4.19) reduces to:

$$\sin \alpha = \sin \theta_B = \frac{\lambda}{2 n \Lambda}\tag{4.20}$$

A-W were able to find the ratio of the intensity of the diffracted light I_d and the incident light I_o by integrating Eq. (4.12a) and (4.16) approximately. Under the conditions of:

- (1) $n_i = n_d = n$
- (2) small Bragg angle $= \theta_B \cong 0$
- (3) a rectangular illuminated volume $a \times w' \times c$,

they obtained:

$$\frac{I_d}{I_o} = \left(\frac{\pi w'}{2 n \lambda} \delta \epsilon_{ij}^{\text{eff}} \right)^2\tag{4.21}$$

where $\delta\epsilon_{ij}^{\text{eff}}$ is the appropriate component of $\tilde{\epsilon}^{\text{eff}}$ determined by the vector \vec{Q} in Eq. (4.12b) and w' is the illuminated width of elastic (or spin) wave in the y-z plane in Fig. 4.2. As shown by McMahon,⁶⁴ one may always replace w' by an effective w , so that the effect of arbitrary cross sections of light and/or elastic waves (or spin waves) can be accounted for.

In the following sections, we will concentrate on the quantities $\delta\epsilon_{ij}$ and \vec{Q} in Eq. (4.12b) to study the characteristics of light scattering from elastic and spin waves. The intensity calculation can then be calculated from Eq. (4.21). Since it is understood that the effective dielectric tensor $\tilde{\epsilon}^{\text{eff}}$ is the one we are concerned with, the superscript "eff" is dropped.

4.3 Characteristics of Light Diffraction from Coherent Elastic Waves

The wave propagation, at optical frequencies, inside a crystal is best described by the well-known indicatrix, which is an ellipsoid whose coefficients are the components of the relative dielectric impermeability tensor B_{ij} , namely⁶⁸

$$\sum_{i,j=1}^3 B_{ij} x_i x_j = 1 \quad (4.22a)$$

where

$$B_{ij} = B_{ji} = (\tilde{\epsilon}^{-1})_{ij} \quad (4.22b)$$

and $\tilde{\epsilon}$ is the effective dielectric tensor. Thus, in general, a small change of refraction index or dielectric impermeability δB_{ij} produced by strains $S_{k\ell}$ in the elastic waves (photoelastic interaction) can be described in terms of a change in the shape, size and orientation of the indicatrix. The change is conveniently written with photoelastic constant $P_{ijk\ell}$ as:

$$\delta B_{ij} = \sum_{k, \ell=1}^3 P_{ijk\ell} S_{k\ell} \quad (i, j = 1, 2, 3) \quad (4.23)$$

where $\delta B_{ij} = \delta B_{ji}$, and the quantities δB_{ij} , $P_{ijk\ell}$, $S_{k\ell}$ are all dimensionless. Since both δB_{ij} and $S_{k\ell}$ are symmetrical tensors, the Eq. (4.23) can be contracted into the matrix form:

$$\delta B_m = \sum_{n=1}^6 P_{mn} S_n \quad (m = 1, 2, \dots, 6) \quad (4.24)$$

where the indices are contracted according to the Voigt notation:

$$\begin{aligned} 11 &\rightarrow 1 & 23 &\rightarrow 4 \\ 22 &\rightarrow 2 & 13 &\rightarrow 5 \\ 33 &\rightarrow 3 & 12 &\rightarrow 6 \end{aligned}$$

$$P_{mn} = P_{ijk\ell} \quad \begin{aligned} (m, n = 1, 2, 3 \dots 6) \\ (i, j, k, \ell = 1, 2, 3 \dots) \end{aligned} \quad (4.25a)$$

$$\begin{bmatrix} \delta B_{11} & \delta B_{12} & \delta B_{31} \\ \delta B_{12} & \delta B_{22} & \delta B_{23} \\ \delta B_{13} & \delta B_{32} & \delta B_{33} \end{bmatrix} \rightarrow \begin{bmatrix} \delta B_1 & \delta B_6 & \delta B_5 \\ \delta B_6 & \delta B_2 & \delta B_4 \\ \delta B_5 & \delta B_4 & \delta B_3 \end{bmatrix} \quad (4.25b)$$

and

$$\begin{bmatrix} S_{11} & S_{21} & S_{31} \\ S_{12} & S_{22} & S_{23} \\ S_{13} & S_{23} & S_{33} \end{bmatrix} \rightarrow \begin{bmatrix} S_1 & \frac{1}{2}S_6 & \frac{1}{2}S_5 \\ \frac{1}{2}S_6 & S_2 & \frac{1}{2}S_4 \\ \frac{1}{2}S_5 & \frac{1}{2}S_4 & S_3 \end{bmatrix} \quad (4.25c)$$

For a cubic crystal (class $m\bar{3}m$), like YIG, the photoelastic matrix P_{mn} has the following form when referred to the axes along the cubic edges

(principal axes):⁶⁹

$$[P_{mn}] = \begin{bmatrix} P_{11} & P_{12} & P_{12} & 0 & 0 & 0 \\ P_{12} & P_{11} & P_{12} & 0 & 0 & 0 \\ P_{12} & P_{12} & P_{11} & 0 & 0 & 0 \\ 0 & 0 & 0 & P_{44} & 0 & 0 \\ 0 & 0 & 0 & 0 & P_{44} & 0 \\ 0 & 0 & 0 & 0 & 0 & P_{44} \end{bmatrix} \quad (4.26)$$

Since we are interested in the small change of dielectric tensor, $\delta\epsilon_{ij}$, we want to express $\delta\epsilon_{ij}$ in terms of P_{mn} . From Eq. (4.22b), $\delta\epsilon_{ij}$ can be written as:

$$\delta\epsilon_{ij} = - \sum_{\alpha, \beta=1}^3 \epsilon_{i\alpha} \delta B_{\alpha\beta} \epsilon_{\beta j} \quad (i, j = 1, 2, 3) \quad (4.27)$$

For a cubic crystal, the unperturbed dielectric tensor ϵ_{ij} is a scalar or

$$\epsilon_{ij} = \delta_{ij} \epsilon \quad (4.28)$$

where δ_{ij} is the kronecker delta function.

Combining Eqs. (4.24), (4.26), (4.27) and (4.28), the photoelastic interaction, when referred to the principal axes of a cubic crystal (class m3m), can be described as:

$$\begin{bmatrix} \delta\epsilon_{11} \\ \delta\epsilon_{22} \\ \delta\epsilon_{33} \\ \delta\epsilon_{23} \\ \delta\epsilon_{31} \\ \delta\epsilon_{12} \end{bmatrix} = -\epsilon^2 \begin{bmatrix} P_{11} & P_{12} & P_{12} & 0 & 0 & 0 \\ P_{12} & P_{11} & P_{12} & 0 & 0 & 0 \\ P_{12} & P_{12} & P_{12} & 0 & 0 & 0 \\ 0 & 0 & 0 & P_{44} & 0 & 0 \\ 0 & 0 & 0 & 0 & P_{44} & 0 \\ 0 & 0 & 0 & 0 & 0 & P_{44} \end{bmatrix} \begin{bmatrix} S_{11} & (S_1) \\ S_{22} & (S_2) \\ S_{33} & (S_3) \\ 2S_{23} & (S_4) \\ 2S_{31} & (S_5) \\ 2S_{12} & (S_6) \end{bmatrix} \quad (4.29)$$

In terms of Eqs. (4.12a), (4.12b) and (4.29), assuming the Bragg angle $\theta_B \cong 0$ (Fig. 4.2), the interaction between an elastic wave propagation along a principal axis and an incident light polarized also along a principal axis can be easily determined in the following manner (Fig. 4.2).

Since $\theta_B = \alpha \cong 0$, and if we assume that the y-z plane of incidence is horizontal, the incident E_O^i and diffracted $E_{O\pm}^d$ electric fields can be written as:

$$\vec{E}_O^i \cong \vec{i}_x E_v^i + \vec{i}_z E_H^i \quad (4.30a)$$

$$\vec{E}_{O\pm}^d \cong \vec{i}_x E_{v\pm}^d + \vec{i}_z E_{H\pm}^d \quad (4.30b)$$

where the (\pm) sign indicates whether the frequency of the diffracted light is upshifted (+) or downshifted (-) from the frequency of the incident light as determined by the phase matching conditions (4.13). From Eqs. (4.12a), (4.12b) and (4.30), we obtain

$$\vec{i}_r \cong \vec{i}_y \quad (4.31a)$$

$$\begin{bmatrix} E_{v\pm}^d \\ E_{H\pm}^d \end{bmatrix} = c \begin{bmatrix} \delta\epsilon_{xx} & \delta\epsilon_{xz} \\ \delta\epsilon_{zx} & \delta\epsilon_{zz} \end{bmatrix} \begin{bmatrix} E_v^i \\ E_H^i \end{bmatrix} \quad (4.31b)$$

where c is to be determined by Eq. (4.12a). For our purpose, the explicit form of c is not important because we want to find out $\delta\epsilon_{ij}$ in Eq. (4.21) only. Note that Eq. (4.31b) is valid even in a coordinate system which is oriented in an arbitrary crystallographic direction, as long as $\theta_B = \alpha \cong 0$. Here, since x, y, z axes are assumed to be the principal axes, Eq. (4.31) and Eq. (4.29) reveal that:

- (a) when longitudinal elastic waves propagate along a principal axis (thereby producing S_{33} in Fig. 4.2), the incident light and diffracted light are polarized along the same principal axes;
- (b) when shear elastic waves propagate along a principal axis (thereby producing either S_{13} or S_{23} in Fig. 4.2), the incident and diffracted lights are polarized along two perpendicular principal axes. Besides, the shear strain S_{23} does not scatter any light at all.

Notice that as $\delta\epsilon_{ij}$ is real for the photoelastic interaction, the diffracted light intensity is independent of the sign of the frequency shift. As we shall see, this is not the case for the coherent spin wave scattering.

In case elastic waves do not propagate along a principal axis or the light is not polarized along a principal axis, one merely uses the method of superposition to find the nature of the interaction. Two examples are used to illustrate this.

Example 1

The interaction geometry of the photoelastic interaction is shown in Fig. 4.4. Longitudinal (with the strain S_{zz}) or shear elastic waves (with the strains S_{xz} and S_{yz}) are excited by a transducer. Again notice from Eq. (4.11) or Eq. (4.31b) that the strain S_{yz} does not scatter any light.

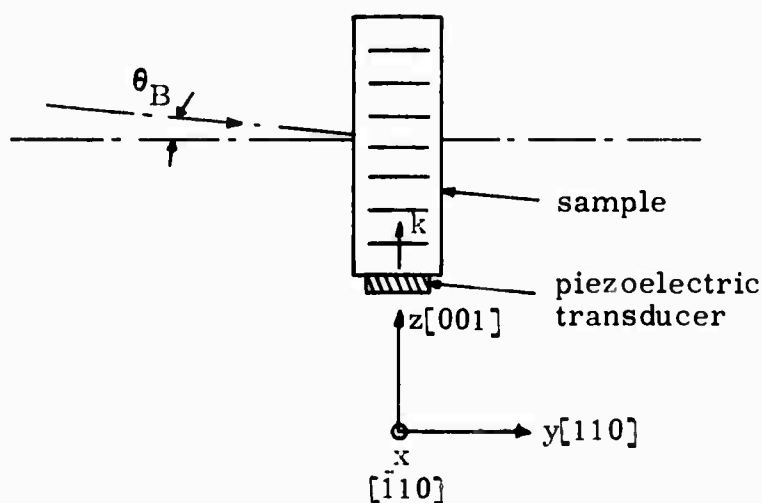


Fig. 4.4 Geometry of the photoelastic interaction.

Since the plane of incidence is not a $\{100\}$ plane (therefore the light is not, in general, polarized along a principal axis), one may either work out the photoelastic interaction in the principal axis coordinate system by transforming all the quantities expressed in the present (x, y, z) coordinate into the principal axis coordinate or transform the photoelastic constants P_{ijkl} into the present coordinate system and use (4.31b). In the present case we do the latter. The transformation from the principal coordinate system ("cubic-edge" coordinate system) is discussed in Chapter II in terms of the Euler Angles (φ, θ, ψ) . From Eq. (4.29) and Eq. (2.4) with $\theta = 0$, $\psi = 0$, but $\varphi \neq 0$, we obtain:

$$\begin{aligned}
 P_{xzxz} &= P_{44} \\
 P_{xxzz} &= P_{12} \\
 P_{zzzz} &= P_{11} \\
 P_{xxxx} &= P_{zzxz} = 0
 \end{aligned}
 \quad \text{independent of } \varphi \quad (4.32)$$

We therefore conclude that for a small Bragg angle, the photoelastic interaction here is independent of φ , the rotation around the $\{100\}$ axis in YIG. In this case, the relation between the polarizations of the incident and the diffracted light can also be readily obtained from Eqs. (4.32) and (4.31b)

Assuming that the polarization of the incident light is at an angle θ from the x-axis (Fig. 4.4), then:

- (a) for shear elastic waves (the strain S_{xz}), the polarization of the diffracted light is at an angle $(\frac{\pi}{2} - \theta)$ from the x-axis;
- (b) for longitudinal elastic waves (the strain S_{zz}), the polarization of the diffracted light is at an angle $\tan^{-1}((P_{11}/P_{12}) \tan \theta)$ from the x-axis.

Example 2

The geometry is shown in Fig. 4.5. Again when we use Eq. (2.2) with $\varphi = 0$, $\psi = 0$, but $\theta \neq 0$, we obtain for the strain S_{zz} :

$$\begin{aligned}
 P_{xxzz} &= \frac{1}{2} \sin^2 2\theta P_{11} + (1 - \frac{1}{2} \sin^2 2\theta) P_{12} - \sin^2 2\theta P_{44} \\
 P_{zzzz} &= (1 - \frac{1}{2} \sin^2 2\theta) P_{11} + \frac{1}{2} \sin^2 2\theta P_{12} + \sin^2 2\theta P_{44} \\
 P_{zxzz} &= P_{xzzz} = \frac{1}{4} \sin 4\theta (-P_{11} + P_{12} + 2P_{44})
 \end{aligned}
 \quad (4.33)$$

and for the shear strain S_{xz} :

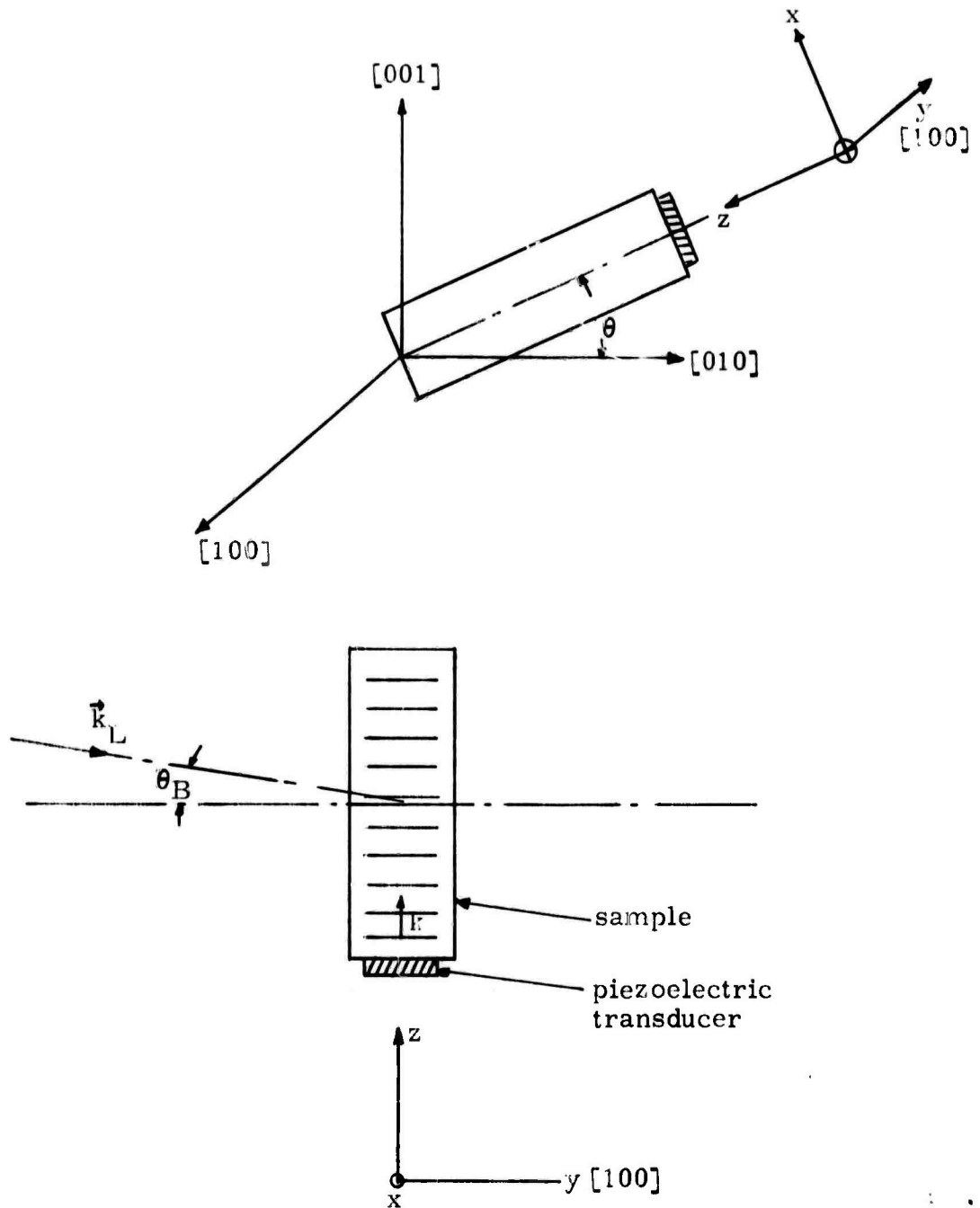


Fig. 4.5 Geometry of the photoelastic interaction and orientation of the long axis (z -axis) of the sample.

$$P_{zzxz} = \frac{1}{4} \sin 4\theta (-P_{11} + P_{12} + 2P_{44})$$

$$P_{xxxx} = \frac{1}{4} \sin 4\theta (P_{11} - P_{12} - 2P_{44}) \quad (4.34)$$

$$P_{zxxz} = P_{xzxz} = \frac{1}{2} \sin^2 2\theta P_{11} - \frac{1}{2} \sin^2 2\theta P_{12} + \cos^2 2\theta P_{44}$$

In particular, for a longitudinal strain S_{zz} , and $\theta = \frac{\pi}{8}$:

$$\begin{bmatrix} \delta\epsilon_{xx} & \delta\epsilon_{xz} \\ \delta\epsilon_{zx} & \delta\epsilon_{zz} \end{bmatrix} = -\frac{1}{4}\epsilon^2 \begin{bmatrix} P_{11} + 3P_{12} - 2P_{44} & -P_{11} + P_{12} + 2P_{44} \\ -P_{11} + P_{12} + 2P_{44} & 3P_{11} + P_{12} + 2P_{44} \end{bmatrix} \quad (4.35)$$

Equation (4.35) is used in Chapter V.

From these two examples, one realizes that the intensity of the diffracted light can be calculated by using Eq. (4.21):

$$\frac{I_d}{I_o} = \frac{1}{2} \left(\frac{\pi w}{\lambda} \right)^2 \left(\frac{n^6 P_{eff}^2}{v_p^3 D_o} \right) P_a \quad (4.36)$$

where $P_a = \frac{1}{2} D_o v_p^3 S^2$; the quantity P_{eff} is the appropriate photoelastic constant, v_p the velocity of elastic wave (longitudinal or shear), P_a acoustic power density, D_o the density of the medium and S is the appropriate strain.

For a circular acoustic beam of an effective diameter w , Eq. (4.36) becomes:

$$\frac{I_d}{I_o} = \frac{2\pi}{\lambda^2} \left(\frac{n^6 P_{eff}^2}{D_o v_p^3} \right) P_A \quad (4.37)$$

where $P_A = \frac{1}{4} \pi w^2 P_a$ and is the total acoustic power.

For YIG^{71, 73} at $\lambda = 1150$ nm:

$$\frac{I_d}{I_o} \cong 1.67 \times 10^{-6} P_A(\text{mW}) \quad (4.38)$$

for the longitudinal elastic waves propagating along a {100} direction and

$$P_{\text{eff}} = P_{12}.$$

$$\frac{I_d}{I_o} \cong 4.0 \times 10^{-6} P_A(\text{mW}) \quad (4.39)$$

for the shear elastic waves propagating along a {100} direction and

$$P_{\text{eff}} = P_{44}.$$

4.4 Characteristics of Light Diffraction from Coherent Spin Waves

In previous work, Auld and Wilson⁵⁶ (A-W), following the derivation of Landau and Lifshitz,⁵⁹ calculated the intensity of light diffracted from coherent spin waves, using a perturbed dielectric tensor restricted to terms linear in the total crystal magnetization. For many magneto-optic experiments, this is sufficient to interpret the observations. However, when the dielectric tensor is modulated by a coherent spin wave, one must look for all terms that are linear in the small signal spin wave amplitude, not just terms linear in the total magnetization M . For example, when the magnetization is along the plus z -axis, terms like $m_x M_z$ and $m_y M_z^2$, although of higher order, are linear in the small signal spin wave amplitudes m_x and m_y . Our derivation of the perturbed dielectric tensor, detailed in Appendix III, is straightforward and essentially follows that of Landau and Lifshitz, with the exception that all linear terms in m_x and m_y are retained. The result for a cubic crystal (class $m3m$), like YIG, is of the form, when expressed in the "cubic edge" coordinate system:

$$\delta\epsilon_{ij}(\lambda) = \delta\epsilon_{ij}'(\lambda) + j \delta\epsilon_{ij}''(\lambda) \quad (i, j = 1, 2, 3) \quad (4.40a)$$

$$\begin{bmatrix} \delta\epsilon_{xx}' \\ \delta\epsilon_{yy}' \\ \delta\epsilon_{zz}' \\ \delta\epsilon_{yz}' \\ \delta\epsilon_{zx}' \\ \delta\epsilon_{xy}' \end{bmatrix} = \begin{bmatrix} g_{11}(\lambda) & g_{12}(\lambda) & g_{12}(\lambda) & 0 & 0 & 0 \\ g_{12}(\lambda) & g_{11}(\lambda) & g_{12}(\lambda) & 0 & 0 & 0 \\ g_{11}(\lambda) & g_{12}(\lambda) & g_{11}(\lambda) & 0 & 0 & 0 \\ 0 & 0 & 0 & g_{44}(\lambda) & 0 & 0 \\ 0 & 0 & 0 & 0 & g_{44}(\lambda) & 0 \\ 0 & 0 & 0 & 0 & 0 & g_{44}(\lambda) \end{bmatrix} \begin{bmatrix} \alpha_x^2 \\ \alpha_y^2 \\ \alpha_z^2 \\ \alpha_y \alpha_z \\ \alpha_z \alpha_x \\ \alpha_x \alpha_y \end{bmatrix} \quad (4.40b)$$

where $\delta\epsilon'_{ij} = \delta\epsilon'_{ji}$.

$$\begin{bmatrix} \delta\epsilon''_{xx} \\ \delta\epsilon''_{yy} \\ \delta\epsilon''_{zz} \\ \delta\epsilon''_{yz} \\ \delta\epsilon''_{zx} \\ \delta\epsilon''_{xy} \end{bmatrix} = \begin{bmatrix} 0 & 0 & 0 \\ 0 & 0 & 0 \\ 0 & 0 & 0 \\ f(\lambda) & 0 & 0 \\ 0 & f(\lambda) & 0 \\ 0 & 0 & f(\lambda) \end{bmatrix} \begin{bmatrix} \alpha_x \\ \alpha_y \\ \alpha_z \end{bmatrix} \quad (4.40c)$$

where $\delta\epsilon''_{ij} = -\delta\epsilon''_{ji}$.

For simplicity we have assumed that the medium is lossless and therefore $\delta\vec{\epsilon}(\lambda)$ is Hermitian. The quantity $f(\lambda)$ is the linear coefficient, $g_{mn}(\lambda)$ the quadratic coefficients, $\alpha_x (= M_x/M)$, $\alpha_y (= M_y/M)$, and $\alpha_z (= M_z/M)$ the direction cosines of the magnetization; both $f(\lambda)$ and $g_{mn}(\lambda)$ are a function of optical frequencies or wavelength λ . When $g_{mn} = 0$, the tensor $\delta\vec{\epsilon}$ reduces to that of A-W. Note that g_{mn} is identical in form to P_{mn} in Eq. (4.29).

The calculation of the intensity of light diffracted from spin waves can be made using Eqs. (4.21), (4.31b) and (4.40). Notice that in Eq. (4.40) the perturbed dielectric tensor is now modulated by z-directed spin waves (wavevector \vec{k} parallel to the dc magnetization vector, which is along the z-axis), with frequency ω . Furthermore, for simplicity, let us assume that the z-directed spin waves are circularly polarized so that α_x and α_y can be written from Eq. (2.16) with $(\omega_k = \omega)$ as:

$$\alpha_x = \frac{M_x}{M} = \frac{m}{M} \cos(\omega t - kz) \quad (4.41a)$$

$$\alpha_y = \frac{M_y}{M} = \frac{m}{M} \sin(\omega t - kz) \quad (4.41b)$$

Here the x, y, z axes do not necessarily coincide with the principal axes.

We are now ready to do the calculation. Just as in the last section, we use two examples to illustrate this.

Example 1

The geometry of light diffraction, identical to Fig. 4.4, is shown in Fig. 4.6; the spin wave amplitudes are given in Eq. (4.41).

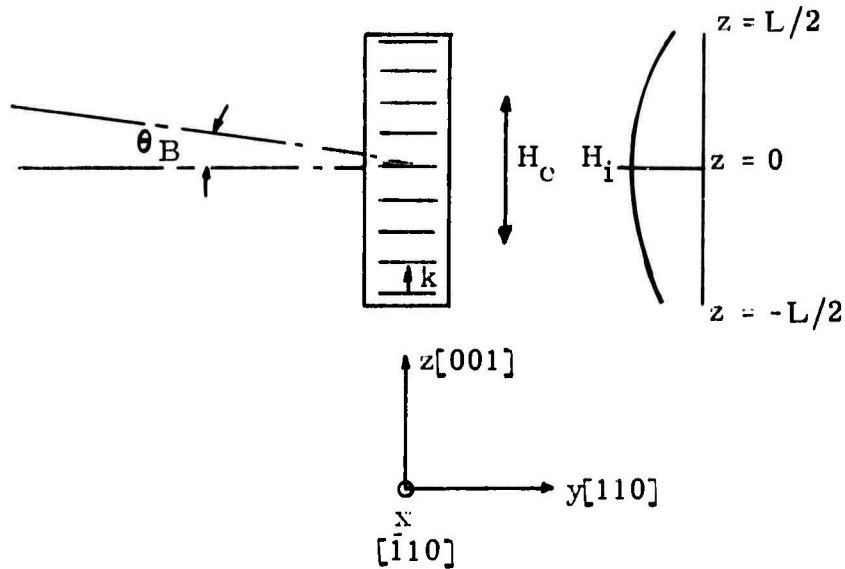


Fig. 4.6 The geometry of light diffraction from spin waves; the internal field profile H_i of the bar is also indicated.

Since the plane of incidence is not a $\{100\}$ plane, we obtain from Eq. (4.40) and Eq. (2.2), with $\psi = \theta = 0$, but $\varphi \neq 0$:

$$\begin{aligned}
 \delta\epsilon_{xx} &= 0 \\
 \delta\epsilon_{zz} &= 0 \quad \text{independent of } \varphi \\
 \delta\epsilon_{xz}^* &= \delta\epsilon_{zx}^* = g_{44} \alpha_z \alpha_x + j f \alpha_y
 \end{aligned} \tag{4.42}^*$$

where only terms linear in α_x, α_y are kept, and $\alpha_z \cong 1$. Substituting Eq. (4.41) into Eq. (4.42), we obtain:

$$\delta\epsilon_{zx} = \left[g_{44} \alpha_z \frac{m}{M} \cos(\omega t - kz) + j f \frac{m}{M} \sin(\omega t - kz) \right] \tag{4.43a}$$

$$= \frac{m}{2M} \left[(g_{44} \alpha_z + f) e^{j(\omega t - kz)} + (g_{44} \alpha_z - f) e^{-j(\omega t - kz)} \right]$$

$$\delta\epsilon_{xz} = \delta\epsilon_{zx}^* \tag{4.43b}$$

$$= \frac{m}{2M} \left[(g_{44} \alpha_z - f) e^{j(\omega t - kz)} + (g_{44} \alpha_z + f) e^{-j(\omega t - kz)} \right]$$

Substituting Eqs. (4.43) into Eq. (4.31b), and noting the phase matching condition in Eq. (4.13), we obtain:

$$\begin{bmatrix} E_{v\pm}^d \\ E_{H\pm}^d \end{bmatrix} = c \frac{m}{2M} \begin{bmatrix} 0 & g_{44} \alpha_z \mp f \\ g_{44} \alpha_z \pm f & 0 \end{bmatrix} \begin{bmatrix} E_v^i \\ E_H^i \end{bmatrix} \tag{4.44}$$

where a subscript v or H denotes whether the polarization of the electric field vectors is perpendicular (x-axis) or parallel to the horizontal (y-z) plane of incidence. The plus or minus sign indicates whether the frequency shift is upward (anti-Stokes line $\omega_L + \omega$) or downward (Stokes

* The asterisk on $\delta\epsilon_{xz}^*$ denotes complex conjugation.

line $\omega_L - \omega$).

From Eq. (4.44) one can deduce that the maximum diffracted light intensity depends on the incident light polarization and the sign of the frequency shift. If f and g_{44} have the same sign, E_v^i will give the maximum diffracted light intensity for the upshifted case, whereas E_H^i will for the case of downshifted diffracted light. Furthermore, reversing the direction of the magnetic field changes the sign of α_z and the sense of the spin wave circular polarization. Consequently, the above situation remains unchanged, because the ratio $(g_{44}\alpha_z\alpha_x/f\alpha_y)$ still has the same sign.

The "anomalous" experimental observations that Collins and Wilson⁵⁷ have reported fit precisely this description, provided one remembers that low to medium wavenumber magnetostatic waves are backward waves with the wavevector direction opposing the direction of the power flow. They found that, with a laser beam polarized perpendicular to the plane of incidence, the scattered beam was always strongest on the left side of the beam when using the left-hand antenna, but was always found on the right side of the main beam when using the right-hand antenna. These two cases correspond to frequency upshifted diffracted light, as indicated in Fig. 4.7. The converse effects, i. e., frequency downshifted diffracted light when the input laser polarization was parallel to the plane of incidence, are also similarly explained.

Other experimental evidence is furnished by Smith's work⁵⁸ in which he found similar situations for light scattering from shear magnetoelastic waves with a large mixture of spin waves. Again he reported it as "anomalous." Section 5.2 gives a more detailed account.

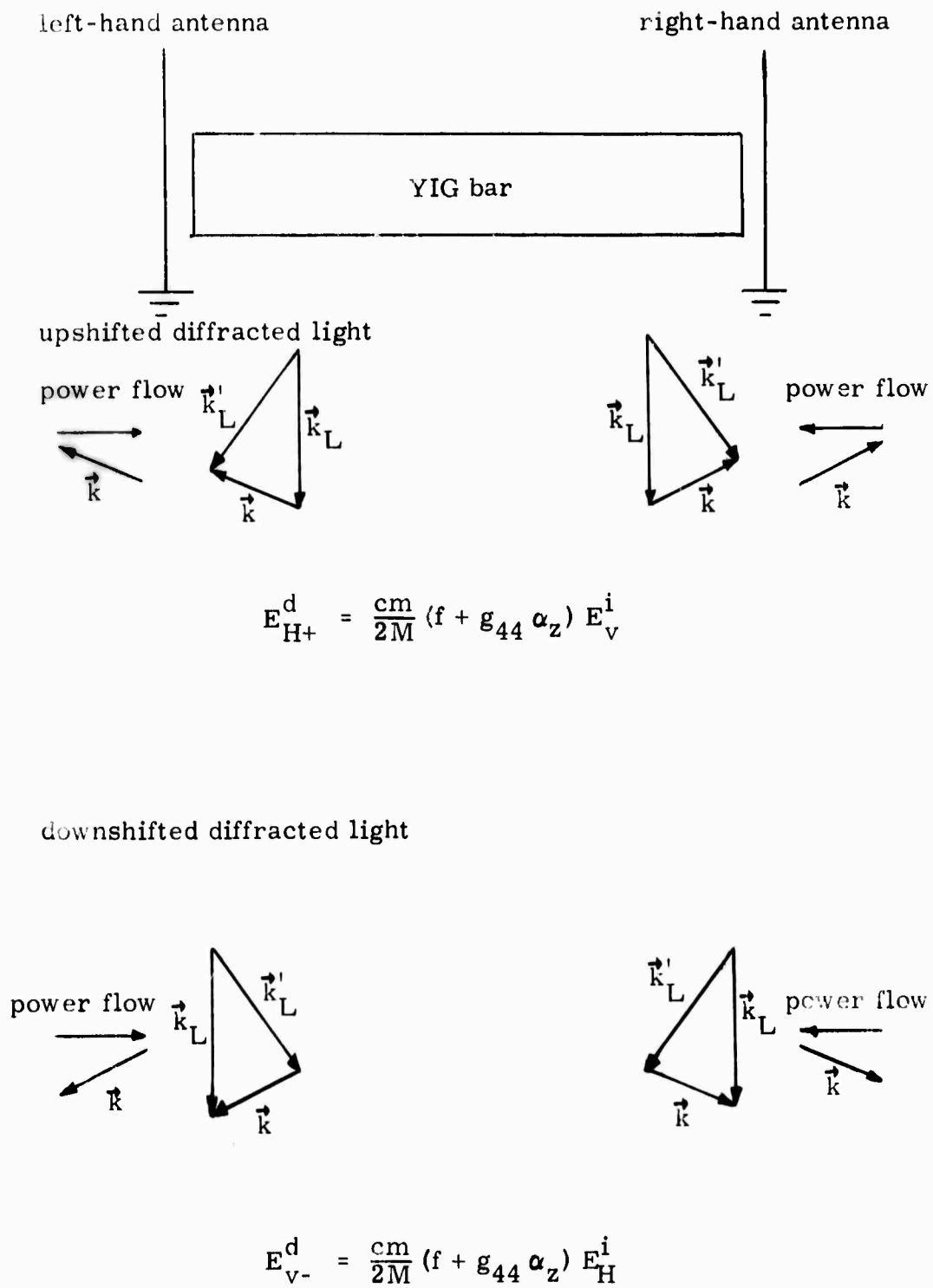


Fig. 4.7 Light diffraction from coherent magnetostatic waves.

Example 2

The geometry of light diffraction is identical to Fig. 4.5 where the applied magnetic field is along the z-direction. Again when we use Eq. (2.2) with $\varphi = \psi = 0$, but $\theta \neq 0$, we obtain:

$$\begin{aligned}\delta\epsilon_{xx} &= \frac{1}{4}\sin 4\theta(g_{11} - g_{12} - 2g_{44})\alpha_z\alpha_x \\ \delta\epsilon_{zz} &= \frac{1}{4}\sin 4\theta(-g_{11} + g_{12} + 2g_{44})\alpha_z\alpha_x \\ \delta\epsilon_{xz}^* = \delta\epsilon_{zx} &= [\frac{1}{2}\sin^2 2\theta g_{11} - \frac{1}{2}\sin^2 2\theta g_{12} + \cos^2 2\theta g_{44}]\alpha_z\alpha_x + jf\alpha_y\end{aligned}\quad (4.45)$$

In particular, for $\theta = \frac{\pi}{8}$, we obtain:

$$\begin{bmatrix} \delta\epsilon_{xx} & \delta\epsilon_{xz} \\ \delta\epsilon_{zx} & \delta\epsilon_{zz} \end{bmatrix} = \frac{1}{4} \begin{bmatrix} \Delta g \alpha_x \alpha_z & (g_{11} - g_{12} + 2g_{44})\alpha_z\alpha_x - 4jf\alpha_y \\ (g_{11} - g_{12} + 2g_{44})\alpha_x\alpha_z + 4jf\alpha_y & -\Delta g \alpha_x \alpha_z \end{bmatrix}\quad (4.46a)$$

where

$$\Delta g = g_{11} - g_{12} - 2g_{44} \quad (4.46b)$$

Notice that when $\Delta g = 0$ (Cauchy relation),^{68, 69} the medium becomes "isotropic," i.e., x, y, z axes are determined by the dc magnetization ($\approx \alpha_z$) and small signal spin wave amplitudes α_x and α_y only. Substituting Eqs. (4.41) and (4.46a) into Eq. (4.31b), as in Example 1, we obtain:

$$\begin{bmatrix} E_{v\pm}^e \\ E_{H\pm}^d \end{bmatrix} = c \frac{m}{2M} \begin{bmatrix} \frac{1}{4} \Delta g \alpha_z & \frac{1}{4}(g_{11} - g_{12} + 2g_{44})\alpha_z \mp f \\ \frac{1}{4}(g_{11} - g_{12} + 2g_{44})\alpha_z \pm f & -\Delta g \alpha_z \frac{1}{4} \end{bmatrix} \begin{bmatrix} E_v^i \\ E_H^i \end{bmatrix}\quad (4.47)$$

Except for the different g 's, Eq. (4.47) is similar to (4.44), and therefore most of the characteristics discussed there are applicable here. When $\Delta g = 0$, Eq. (4.47) is identical to Eq. (4.41).

CHAPTER V

EXPERIMENTAL RESULTS OF LIGHT DIFFRACTION FROM COHERENT ELASTIC AND/OR SPIN WAVES IN YIG

In this chapter, experimental results of light diffraction from coherent shear elastic/spin waves, and longitudinal elastic/spin waves in YIG are presented. Of particular interest is the strong infrared Bragg scattering from coherent spin waves reported in section 5.3.⁷⁸ The experimental results in this case appear to be in good agreement with the theory on light scattering from coherent spin waves derived in the last chapter.

The chapter begins with a review of previous experimental work on light diffraction in YIG, followed by a description of the optical experimental setup. In section 5.2, results of Bragg diffraction from shear elastic/spin waves similar to the work of Dixon⁷³ and Smith^{74,75,76} are described. In the last section of the chapter, 5.4, we report on measurements of temporal longitudinal elastic/spin wave conversion efficiencies, which are difficult with conventional microwave techniques whenever intrinsic non-uniform fields due to demagnetizing effects occur inside a ferrimagnetic sample.

Dixon and Matthews⁷¹ first employed coherent light scattering from shear elastic waves to measure the photoelastic constants of YIG. In a later paper, Dixon,⁷² using an optical heterodyne system, reported large Faraday rotations of shear elastic waves and a substantial frequency dispersion of shear elastic/spin waves in YIG. Smith reported light scattering from shear elastic/spin waves that had been excited both acoustically^{74,75} and magnetically.⁷⁶ Of necessity, he employed rf magnetic and electric field excitation at high microwave power inputs of

5 to 300 watts; therefore, nonlinear interactions probably occurred. He also observed the dependence of the scattered light intensity on the incident light polarization and diffracted light frequency shifts. Based on Auld and Wilson's (A-W) theory,⁵⁶ he interpreted this dependence qualitatively as due to the interference of the scattered light from elastic and spin waves. Subsequently, A-W⁷⁷ observed the field dependence of scattered light intensity for longitudinal elastic/spin waves in an obliquely magnetized YIG bar, but their experimental data were not accurate enough to either prove or disprove their calculation.⁵⁶ Collins and Wilson⁵⁷ studied the light scattered from magnetostatic waves; they reported an "anomalous behavior" unexplained by the A-W theory which, however, can be interpreted quite satisfactorily by our new theory described in section 4.4. Most recently, Desormiere et al.⁷⁹ reported on related experiments on light diffraction from magnetostatic waves and observed "anomalous behavior" similar to what Collins and Wilson had reported.

5.1 Setup for Light Diffraction Experiments

The experimental setup shown in Fig. 5.1a comprises a microwave system which is used for injecting and monitoring coherent elastic waves via piezoelectric transducers in YIG, and an optical system for sending a coherent laser beam and detecting the diffracted light from the elastic and/or spin waves in the sample.

The microwave system is similar to that in Fig. 3.1, except that a TWT (HP 489A, maximum power output = 2.0 watts at L band), capable of amplification of μ sec pulses, is used following the PIN modulator to boost the power output of the signal generator. When using bulk transducers, which are less efficient, have narrower bandwidth, but can

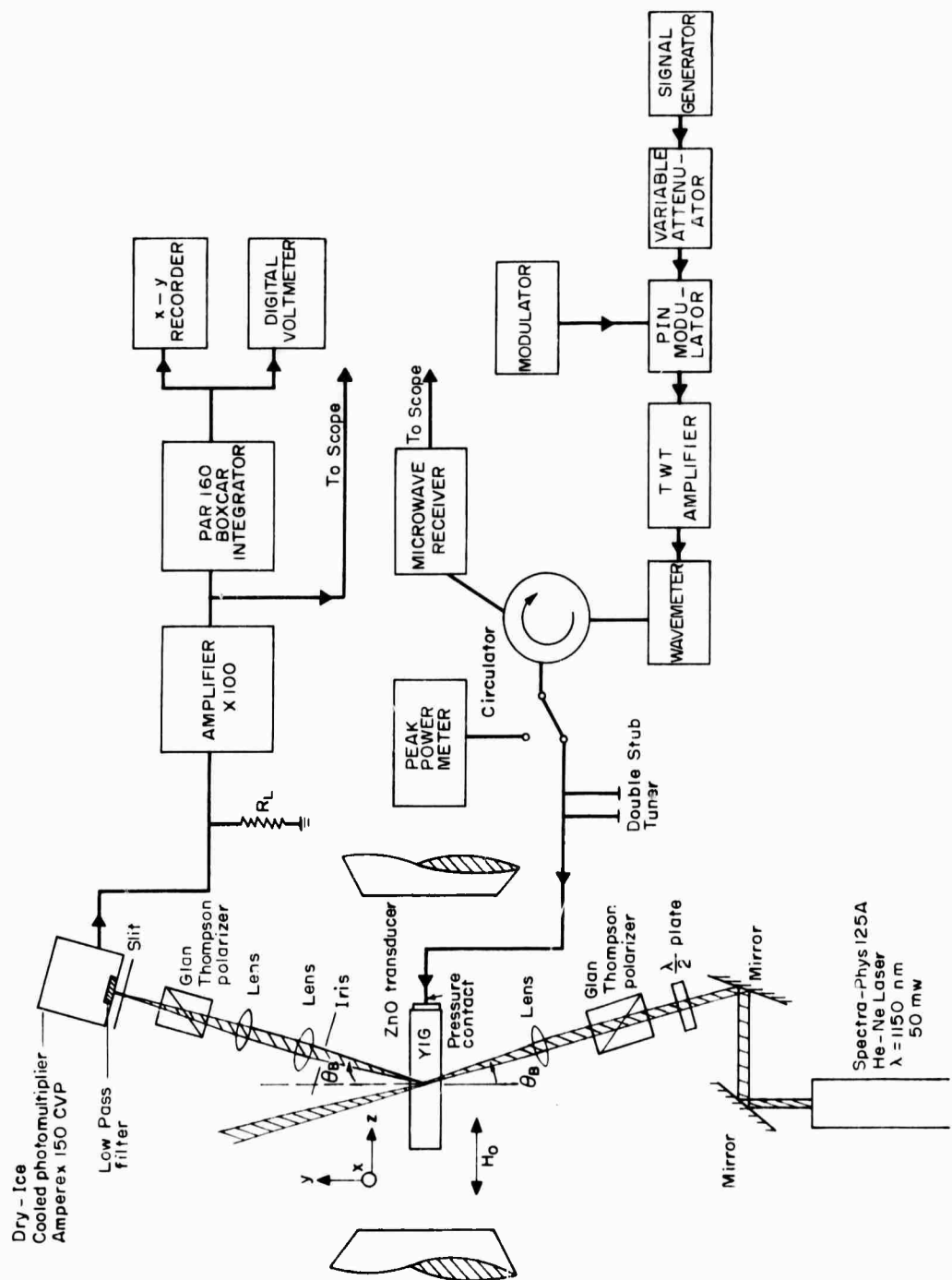


Fig. 5.1(a) Block diagram of the optical experimental setup.

handle more power than the thin film transducer, a power oscillator (a modified AIL 125, externally pulse modulated), capable of 20 to 50 watts power output, was sometimes used to facilitate the location of the diffracted light signal. A peak power meter (Narda 66A3A) is used to measure the input pulse power to the transducers. The microwave receiver system is essentially the same heterodyne system described in section 3.1, but with a limiter and an attenuator preceding the mixer / preamplifier to prevent an excessive power loading of the mixer. The receiver system is used to measure the transducer losses, optimize the stub tuner (which was as close to the load as feasible), monitor the acoustic echo from the sample and provide supplementary information regarding the interpretation of the optical signal.

The samples used in the optical experiments are rectangular YIG bars with two end surfaces as well as two opposite long surfaces optically polished. The orientation of the crystals is described separately in each section. No optical antireflection coating is used on the long polished surfaces. The piezoelectric transducers used in the experiments for injecting elastic waves into the sample are either bulk transducers or a sputtered ZnO thin film transducer. The bulk transducers are X-cut LiNbO_3 plates for generation of linearly polarized shear elastic waves, or Z-cut Li-doped ZnO plates for generation of longitudinal elastic waves. The dimensions of the bulk transducers are 0.005" in thickness and about 0.120" in diameter. For the bulk transducer bonded with phenyl benzoate,⁸⁰ typical insertion loss (i.e., the power ratios of the input pulse to the first echo) is 50 db or more at 1 GHz. The sputtered thin film ZnO transducer (courtesy of Dr. N. F. Foster of Bell Telephone Labs., Inc.), on the other hand, has a very large bandwidth

and initially exhibited only a 20 db insertion loss but, unfortunately, deteriorated later to about 36 db.

The optical system consists of the following components (Fig. 5.1a):

- (a) A laser: ^{*} Spectra-Physics Model 125A modified to give maximum power output at 1150 nm; power output, 50 mW; transverse mode, TEM₀₀; dc excitation. [†]
- (b) A set of three mirrors mounted on micro-positioners for coarse and vernier movements in the horizontal and vertical directions. The mirrors are dielectric-coated and give 99% reflectance at 45° incident angle for "p- and s-polarized" light. [‡] One of the three mirrors is not used at 45° angle of incidence and probably should be replaced by a more suitable mirror.
- (c) Two Glan-Thompson polarizers mounted on rotating stages to allow selection of the polarization of the transmitted light. The polarizers, with an extinction ratio of 10⁵:1, prove to be extremely useful in improving signal-to-noise ratio when the diffracted light is polarized at 90° with respect to the incident light, as in the cases of diffraction from shear elastic waves and spin waves.

^{*} A 1 mW 1150 nm laser was used in the early stages of the work and we did observe diffracted light signals with 10 watts microwave power into a LiNbO₃ transducer (~50 db insertion loss) after three hours of integration time with a PAR 160 boxcar integrator.

[†] An rf excitation gives more power output and stability but may cause electromagnetic interference with other instruments in use. Therefore a dc excitation sometimes is more desirable.

[‡] The phrase "p-polarized" refers to light polarized in the plane of incidence, while "s-polarized" refers to light polarized perpendicular to the plane of incidence. One should beware that some manufacturers may, without warning, supply dielectric mirrors which give 99% reflectance at 45° angle of incidence for only s-polarized light.

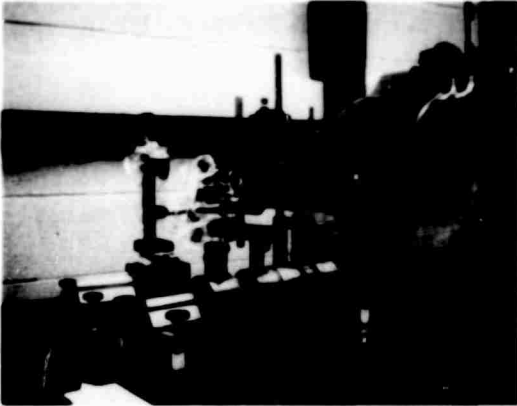
- (d) Three lenses are employed, as shown in Fig. 5.1a. One is used for focusing the 5 mm laser beam onto the surfaces of the sample, the other two for collecting diffracted light and focusing it into a slit in front of the photomultiplier.
- (e) An iris in front of the first collecting lens and a slit in front of the photomultiplier, as shown in Fig. 5.1a, are found to be very helpful in reducing the scattered background light.
- (f) An Amperex 150 CVP photomultiplier (S-1 photocathode, operating at 1,500 V) is cooled to the dry ice temperature in a housing (Products for Research Model TE-200). Cooling of the photomultiplier to dry ice temperatures is necessary here because of the high dark current, low quantum efficiency of the S-1 cathode, and the low level diffracted light signal obtained in the experiments. A heated ring is installed on the outer surface of the viewing window of the photomultiplier housing to prevent the formation of dew on the cold surface. A low pass filter (transmittance 80% at 1150 nm and above, from IR Industries) is also placed in front of the viewing window to prevent any stray room light from getting into the photomultiplier.
- (g) A mica half-wave plate for 1150 nm is also used between the laser and the polarizer to rotate the polarization of the incident light. A Kodak IR Phosphor Card, which converts the near infrared to visible red light, is useful for optical alignment but is not sensitive enough to observe the diffracted light.
- (h) A sample stage placed in the airgap of the pole pieces of a Varian 6" magnet can be used to position the samples properly

with respect to the incident light beam. When experimental data are taken the sample is not moved with respect to the applied magnetic fields. Other details of the optical experimental setup are shown in Fig. 5.1b.

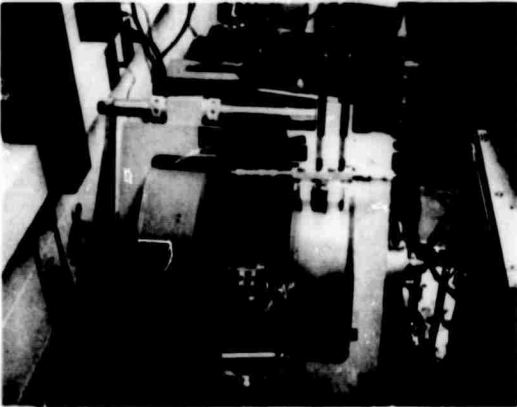
The electronic system following the output of the photomultiplier contains (Fig. 5.1a):

- (a) Load Resistor R_L . Either a 1 K ohm resistor for better signal-to-noise ratio or a 50 ohm resistor for faster risetime of the diffracted light pulse is used.
- (b) For $R_L = 1$ K, an amplifier with 10 MHz bandwidth and an amplification of 100 is adequate for the input of the boxcar integrator. However, for $R_L = 50$ ohm, an amplification of 1,000 and a larger bandwidth (70 MHz) are needed to observe the fast diffracted pulse.
- (c) A PAR Model 160 boxcar integrator is used to measure the diffracted light signal and take the experimental data. The output of the boxcar integrator is fed into a digital voltmeter for display and an x-y recorder for permanent records. The display of the digital voltmeter is found to be very helpful for optimizing the signal in a dark room.

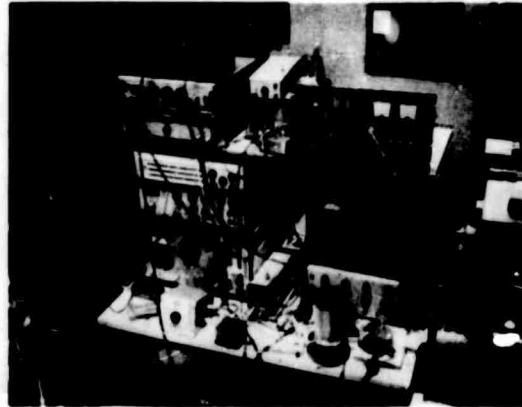
The experimental difficulties in performing optical probing of elastic and/or spin waves are dominated by the poor signal-to-noise ratio, worsened in particular by the poor quantum efficiency of the S-1 photocathode and comparatively low power laser available at 1150 nm. If one is working in the visible spectrum, a factor of 1,000 improvement in photocathode quantum efficiency can be obtained and, in addition, perhaps a factor of 10 increase in laser power output before



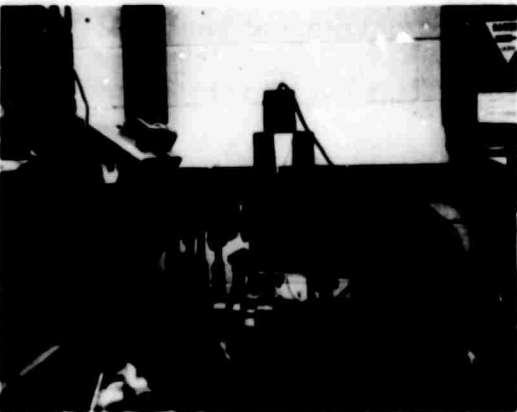
(a) Laser beam incident system, the laser (not shown) is at the left of the picture.



(b) The magnet and sample holder



(d) Microwave apparatus



(c) Optical detection system

Fig. 5.1(b) Optical experimental setup.

problems of heating the sample under investigation occur. Wilson,⁸¹ following Anderson,⁸² gave a simple calculation of the minimum detectable intensity of an optical signal diffracted from either a square wave or a pulse modulated elastic or spin wave. There is nothing further we want to add, except to point out that under our experimental situation (with laser power 50 mW and acoustic power inside the medium less than 1 mW) the noise is always dominated by the background noise, which comes either from scattering from imperfections on the surface or from inside the crystal. While the signal intensity is proportional to the incident laser power, the background noise due to scattering from the crystal imperfections is proportional only to the square root of the laser power. Consequently a high power laser is still helpful even in this case. Of course when the noise is dominated by the dark current, the high power laser is even more helpful.

5.2 Infrared Bragg Scattering from Shear Elastic/Spin Waves

Bragg scattering from shear elastic/spin waves in YIG has been studied extensively, first by Dixon,^{71, 72} then by Smith.^{58, 74-76} Dixon has exhausted almost all the experimental cases of interest with this kind of light scattering, with the exception of the dependence of the intensity of the diffracted light on the incident light polarization and the the sign of the frequency shift. Smith^{58, 76} first reported this dependence and, based on the A-W theory, interpreted it qualitatively as the interference between the light diffracted from elastic waves and from spin waves. However, he found an "anomaly" which his interpretation fails to explain.⁵⁸ The "anomaly" occurs when the light is scattered by the shear elastic/spin waves with a large mixture of spin waves. He thought this "anomaly" might be due to the large amplitude of the shear elastic/spin wave signal used in his experiments. In fact, he did report some nonlinear behavior of light scattering from shear elastic/spin waves.⁷⁵

In this section we report some results on light scattering from shear elastic/spin waves under essentially the same experimental conditions as Smith's, but employing a much reduced microwave power input. Within the range of microwave power which we operated, no nonlinear behavior in the light scattering was observed.

Our experiments were performed using a rectangular YIG bar which measures 4 mm x 4.6 mm x 12.7 mm and is oriented at a $\langle 100 \rangle$ axis (Fig. 4.4 or 4.6). A LiNbO_3 shear wave piezoelectric transducer with a 50 db insertion loss was bonded to the YIG bar and used to excite shear elastic waves. The peak power of a 1.0 μsec , 1.3 GHz micro-

wave pulse used was between 100 mW and 500 mW (versus Smith's 5-300 W).

Figure 5.2 shows typical diffracted light pulses observed with the light beam near the free end of the bar. A diffracted light pulse results each time the shear elastic wave packet, which is reflected back and forth in the sample, crosses the path of the light beam. In the figure the insert is a trace from a Tektronix 585 scope, while the graph was plotted from the signal conditioned with the PAR boxcar integrator. The quantities E_H^i and E_{v-}^d , defined in Eq. (4.30), denote the polarizations of the incident and diffracted light; the minus sign following the subscript v indicates the downshifted diffracted light. The quantity H_0 is the external applied magnetic field. Figure 5.3 is a plot of the diffracted light intensity as a function of the external applied magnetic field H_0 , when the light beam is incident near the mid-point of the long axis of the sample at the time when the shear elastic/spin wave packet crosses the path of the incident light beam for the first time. The solid curve was obtained when the incident light was polarized in the horizontal plane of incidence (hence E_H^i) and the downshifted diffracted light, polarized perpendicular to the plane of incidence (hence E_{v-}^d). On the other hand, the dashed curve was obtained when the incident light was polarized vertically (E_V^i) and the downshifted diffracted light, polarized horizontally (E_{H-}^d). The Bragg angle for the shear elastic waves outside the sample was 13.3° (Eq. (4.20)).

The sample was then rotated 180° around an axis perpendicular to the horizontal plane of incidence so that the upshifted diffracted light could be obtained. The position of the sample was readjusted so that the light beam was incident near the mid-point of the long axis again.

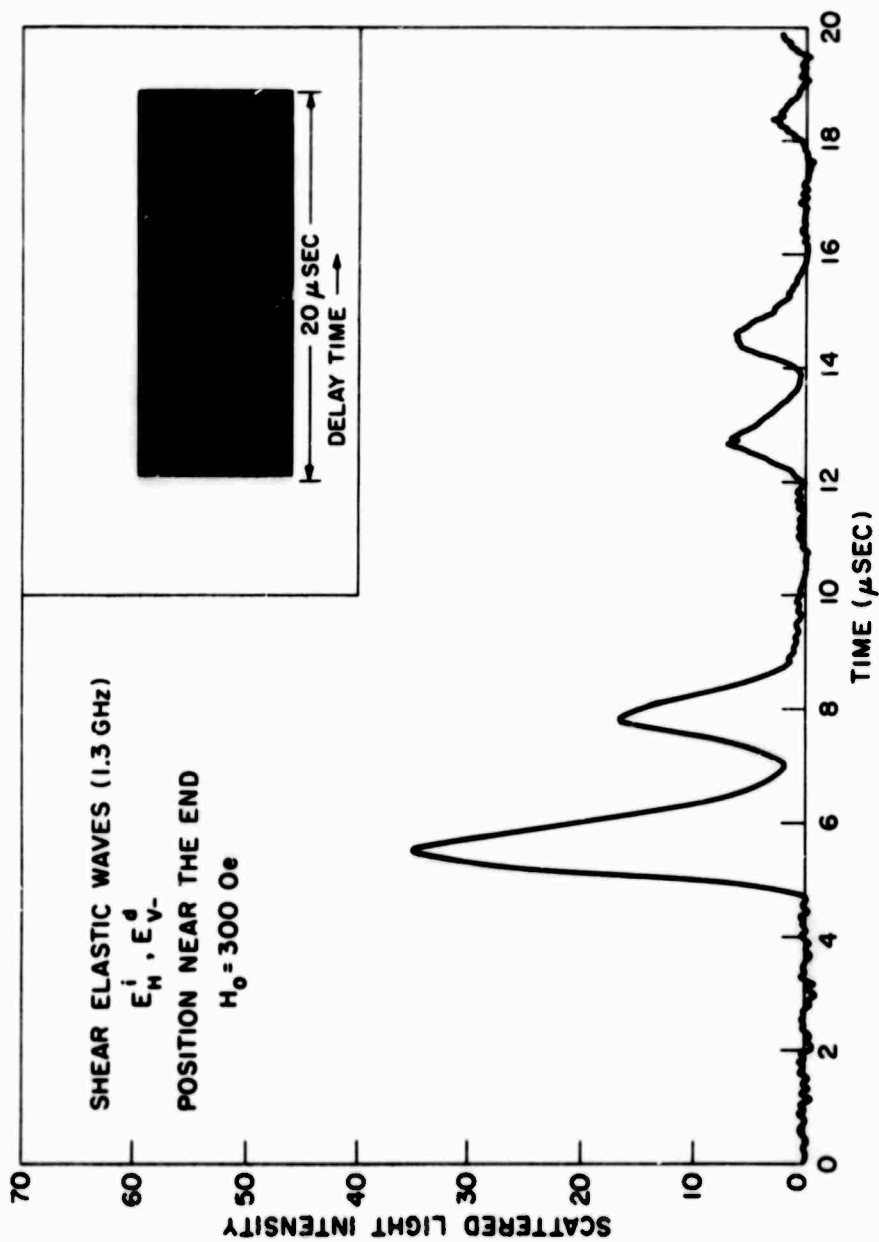


Fig. 5.2 Diffracted light pulses from a 1.3 GHz shear elastic wave pulse propagating along a $\langle 100 \rangle$ direction and polarized along a $\langle 110 \rangle$ direction in YIG. The graph was recorded with the signal from the PAR boxcar integrator. The insert is the scope trace.

A plot of the diffracted light intensity as a function of the external applied fields with either horizontally or vertically polarized incident light gave exactly identical curves in reverse order. In contrast to the previous case, the solid curve was obtained when the incident light was vertically polarized (E_v^i) and the upshifted diffracted light, horizontally polarized (E_{H+}^d), while the dashed curve was obtained when the incident light was horizontally polarized (E_H^i) and the upshifted diffracted light, vertically polarized (E_{v+}^d). These results are, in fact, identical to those Smith⁵⁸ has obtained with high microwave power input. Therefore we conclude that the "anomaly" he reported is not due to the nonlinear effect, but is intrinsic with the light diffraction from spin waves.

Notice in Fig. 5.3 that when $H_0 > H_C^S$ (H_C^S is the applied field value for which the shear crossover point^{10, 11} is at the mid-point of the long axis), the diffracted light intensity becomes independent of the incident light polarization, which is expected, since only the negative rotating shear elastic wave is present here.⁷² In the case of $H_0 < H_C^S$ (and the downshifted diffracted light), E_v^i gives a systematically larger diffracted signal E_{H-}^d than the E_H^i . (The intensity oscillations in Fig. 5.3 result from the acoustic Faraday rotation.⁷²) This is consistent with Smith's theory, in which he pointed out that this effect is due to the interference of the light diffracted from elastic waves and spin waves. This also checks with our new theory, derived in section 4.4 (Example 1), when our calculations (rather than A-W's) of the contribution of the diffracted light intensity from spin waves are used in Smith's theory.

When $H_0 \approx H_C$ (and the downshifted diffracted light), the shear elastic/spin waves contain a large mixture of spin waves. In this case, E_H^i gives a larger diffracted signal (a peak marked "spin" in Fig. 5.3)

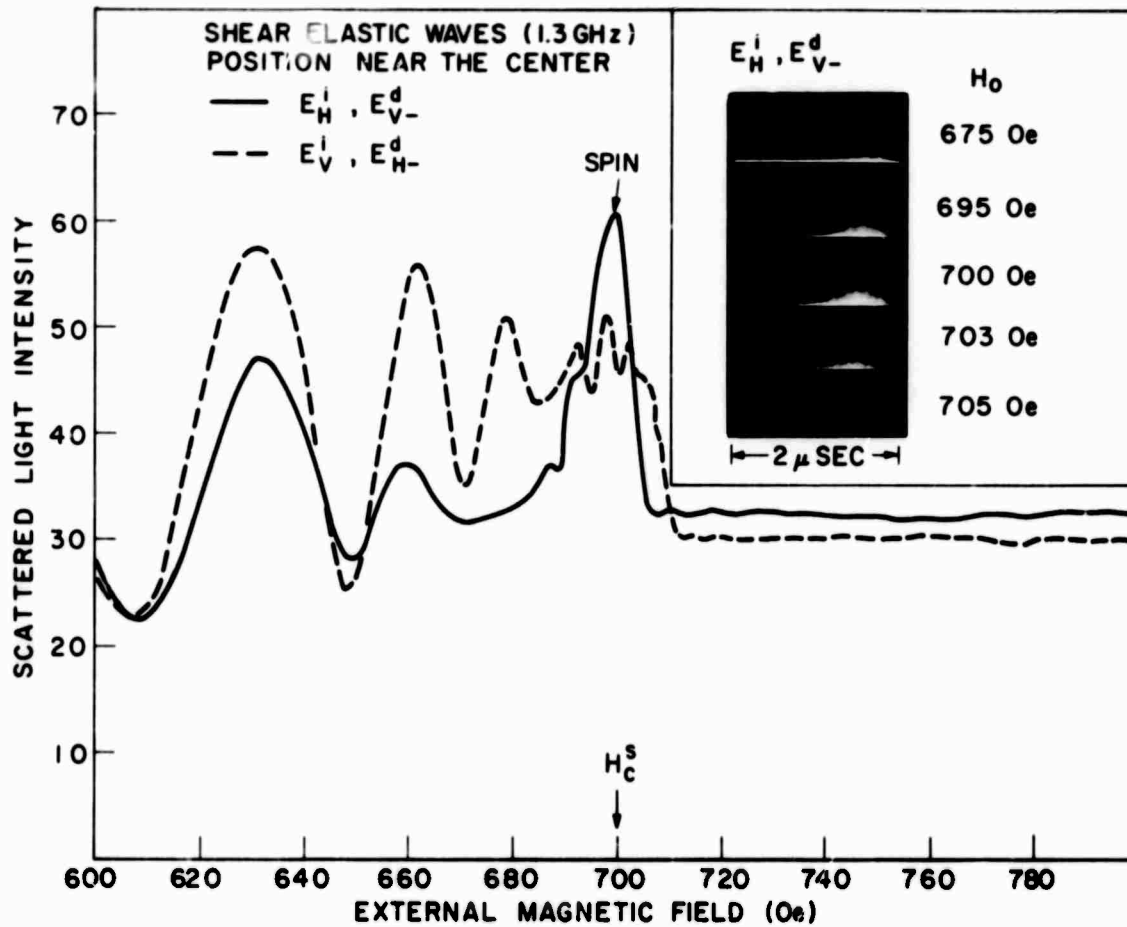


Fig. 5.3 Diffracted light intensity (in arbitrary units) of shear elastic/spin waves as a function of external magnetic field; the light beam is incident near the mid-point of the long axis. The insert is the scope trace swept from right to left when $H_0 \approx H_c^s$, indicating small group velocity dispersion. A full explanation is given in the text.

which Smith was not able to explain (the "anomaly"). According to our theory for spin wave scattering, detailed in section 4.4, Example 1, the incident electric field E_H^i should indeed give a larger diffracted signal for the downshifted diffracted light.

All the phenomena of the converse case, i. e., the upshifted case, can be similarly explained.

In order to ascertain that the peak (marked "spin") in Fig. 5.3 does result from light diffracted from coherent spin waves, another plot of the diffracted light intensity as a function of external magnetic fields was made (Fig. 5.4). In obtaining Fig. 5.4, the incident light was polarized at an angle of $\frac{1}{4}\pi$ from the x-axis (Fig. 4.4 or 4.6) and the diffracted light was always downshifted in frequency. The solid curve was obtained when the polarizer in front of the photomultiplier was set to transmit only the diffracted light polarized at an angle of $\frac{3}{4}\pi$ from the x-axis, while the dashed curve, only the light polarized at an angle of $\frac{\pi}{4}$ from the x-axis. According to Example 1 in section 4.3, the diffracted light from the elastic waves must be polarized in the same direction as the incident light; consequently the diffracted signal of the solid curve could only result from the light diffracted from spin waves. Furthermore: (1) the applied field value at the peak of the solid curve is equal to H_c ; (2) there is a small observable decrease in the Bragg angle θ_B due to the decreasing wavenumbers of the spin waves in the non-uniform internal field; the inserts in Fig. 5.4 indicate a small increase of the delay time of the diffracted light pulse due to the decreasing group velocities of the waves; and (3) the diffracted signal disappears when $H_0 > H_c$.

Figure 5.5 and Fig. 5.6 show plots of diffracted light intensity as a

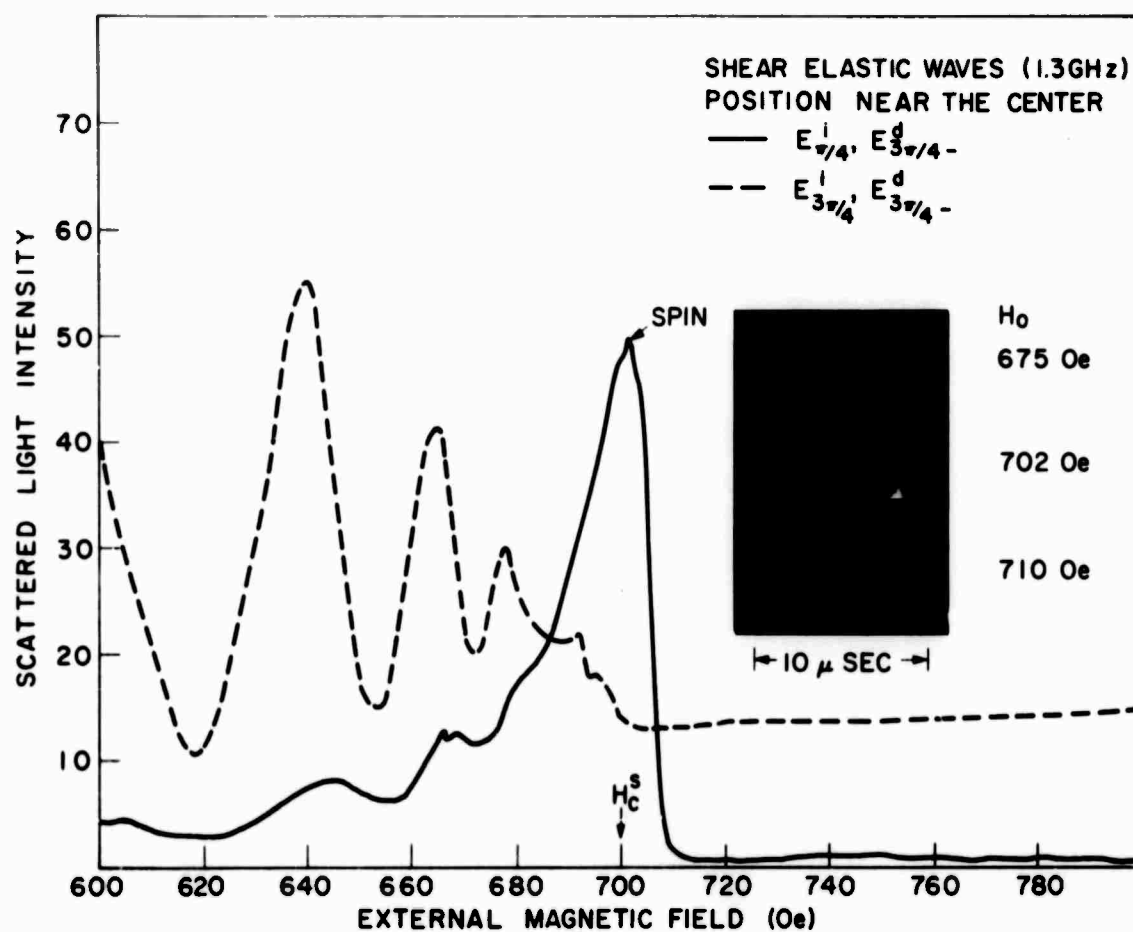


Fig. 5.4 Diffracted light intensity (in arbitrary units) of shear elastic/spin waves as a function of external magnetic field; the light beam is incident near the mid-point of the long axis. The insert is the scope trace swept from right to left when $H_0 \cong H_c^s$, indicating diffracted light intensity (marked "spin" on the curve) and a slight decrease of the group velocity.

function of the external applied field. The solid and dashed curves in both figures correspond, respectively, to the waves propagating parallel and antiparallel to the applied field. The curves in each figure were obtained by reversing the applied field only and leaving all other experimental conditions, including the sample location in the air gap of the magnet, unchanged. Notice in these figures that the shape of the curves is the same for a given incident light polarization and diffracted light polarization and frequency shift. Thus, light diffraction from spin waves is not affected by the direction of the applied field, in agreement with our theory. However, the magnitude of the diffracted signal or the height of the curves in the same figure differs slightly. Since the applied field was the only condition that had been changed, the conclusion is that the sample in the air gap experienced different applied field homogeneity for the two opposite directions of the applied field.

Finally, from all these observations we conclude that the intensity of light diffracted from coherent spin waves depends on the incident light polarization and frequency shift of the diffracted light. This characteristic is intrinsic for the interaction of light and spin waves and is not due to the interference between the light diffracted from elastic waves and spin waves.

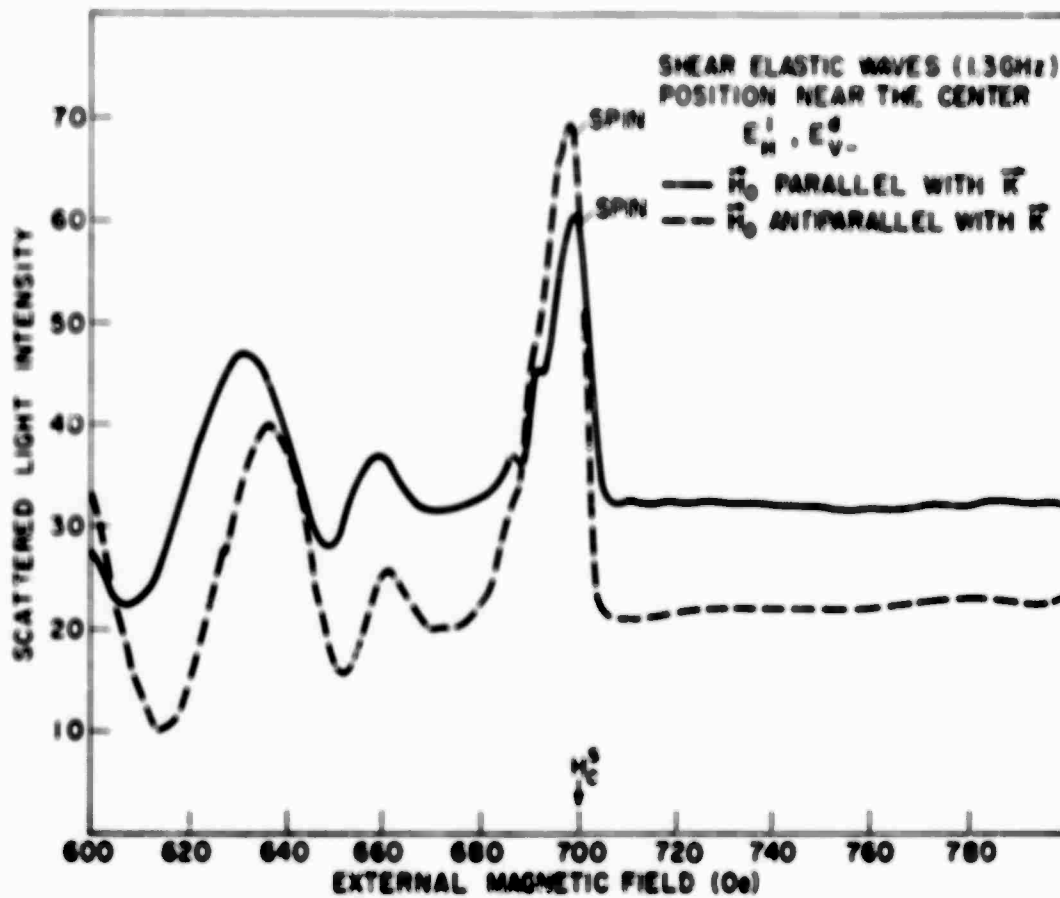


Fig. 5.5 Diffracted light intensity of shear elastic/spin waves as a function of external magnetic fields, illustrating the effect of homogeneity of the applied field.

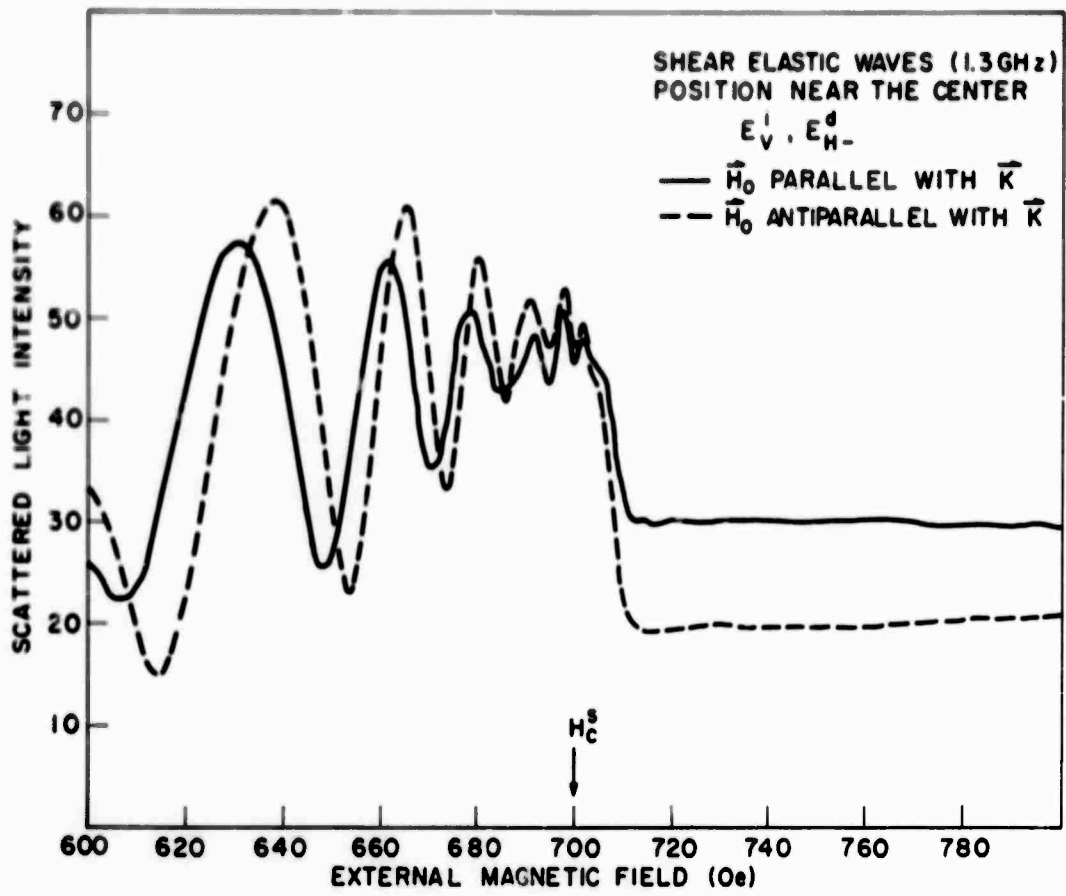


Fig. 5.6 Diffracted light intensity of shear elastic/spin waves as a function of external magnetic fields, illustrating the effect of homogeneity of the applied field.

5.3 Strong Infrared Bragg Scattering from Coherent Spin Waves⁷⁸

In this section we report the first direct observation of strong Bragg-scattered infrared light from coherent spin waves. The maximum scattered light intensity is found to be at least five times stronger than that from longitudinal elastic waves of comparable power. The coherent spin waves were generated through efficient space-gradient conversion from longitudinal elastic waves; the latter were excited by the sputtered ZnO transducer. The scattered light intensity is, again, found to be dependent on the incident light polarization and the sign of frequency shift (Stokes or anti-Stokes lines), and independent of the direction of the applied magnetic field. All these observations are in agreement with our new theoretical results derived in section 4.4, Example 2.

Before outlining our experiments, it is deemed helpful to review the underlying physics of microwave spin/elastic wave conversion.

A ferromagnet subject to a spatially varying internal magnetic field has a non-uniform refractive index insofar as spin wave propagation is concerned. As discussed in detail by numerous authors,^{11,21} a spin wave traveling in such a medium will undergo variation of its wave-number. In crossover regions where the frequency and wavenumber of the spin wave match those of an appropriate elastic wave, conversion to the elastic wave or vice versa will occur with an efficiency η given approximately by:^{11,21}

$$\eta = 1 - e^{-H'_{\text{crit}}/|H'(z_{\text{cr}})|} \quad (3.6)$$

The quantity $H'(z_{\text{cr}})$ is the value of the magnetic field gradient in the crossover region; H'_{crit} is a critical field gradient that is, in simple

cases, proportional to the square of the magnetoelastic splitting frequency.

Longitudinal elastic waves launched at an end surface of an axially magnetized bar, experience an increasing magnetic field as they approach the center of the bar.^{10, 11, 25} If an appropriate external magnetic field is applied such that there are crossover regions inside the sample, conversion to spin waves will occur at those regions, with efficiencies being determined by Eq. (3.6). After conversion, the wavenumbers start to decrease as the spin waves encounter the increasing magnetic fields. Subsequent conversion from spin waves into shear elastic waves is therefore not possible. On the other hand, if one starts from shear elastic waves, subsequent conversion from spin waves into longitudinal elastic waves would be possible (Chapter III).

For YIG at room temperature and with the magnetization lying in a {100} plane at an angle of (22.5°) from a $\langle 100 \rangle$ axis, the values of H'_{crit} for the longitudinal and shear crossover regions are, respectively, 150 Oe/cm/GHz and 19,000 Oe/cm/GHz.¹⁵ Owing to the small longitudinal magnetoelastic splitting, the transition from longitudinal elastic to magnetic character is very abrupt. Therefore, in a fairly uniform magnetic field the spin waves can be locally excited through the spatial conversion and essentially frozen with a well defined wavenumber, before they eventually spread into spin waves with dissimilar wavenumbers.

Our experiments with longitudinal elastic/spin wave scattering utilized the geometry shown in Fig. 5.1a. The rectangular single crystal YIG bar measures 4 x 4 x 12 (mm) and was cut so that its long axis is oriented in a {100} plane at an angle of (22.5°) from a $\langle 100 \rangle$ axis (Fig. 4.5). Two end surfaces, as well as two opposite long {100}

surfaces, of the bar were polished optically flat. The sputtered ZnO transducer with one-way conversion loss of approximately 15 db at 1.5 GHz was used to excite longitudinal elastic waves. The peak power of a 0.5 μ sec, 1.5 GHz microwave pulse used was between 10 mW and 200 mW. The half-wave plate and Glan-Thompson polarizers were used to obtain various combinations of incident and diffracted light polarization. The Bragg angle for the longitudinal elastic waves outside the sample was 6.9°.

Initially, experiments (Fig. 5.7) were done at fairly high magnetic fields (2700 Oe) where at 1.5 GHz the magnetoelastic coupling is virtually zero. Notice that as the long axis of the sample is not along any principal crystallographic direction, the photoelastic parameters involved are a linear combination of the photoelastic constants, and the polarization of the light diffracted from the longitudinal elastic wave will not be in the same direction as that of the incident light. The electric fields of the diffracted light (E_v^d, E_H^d) are related to those of the incident light (E_v^i, E_H^i), according to Eqs. (4.31b) and (4.35), by:

$$\begin{bmatrix} E_v^d \\ E_H^d \end{bmatrix} = -\frac{\epsilon}{4} c \begin{bmatrix} P_{11} + 3P_{12} - 2P_{44} & -P_{11} + P_{12} + 2P_{44} \\ -P_{11} + P_{12} + 2P_{44} & 3P_{11} + P_{12} + 2P_{44} \end{bmatrix} \begin{bmatrix} E_v^i \\ E_H^i \end{bmatrix} \quad (5.1)$$

where c is a constant that can be calculated, if necessary, from Eq. (4.12a). The absolute values of the photoelastic constants P_{ij} for YIG are reported by Dixon and Matthews⁷¹ as:

$$|P_{11}| = 0.025$$

$$|P_{12}| = 0.073$$

$$|P_{44}| = 0.041$$

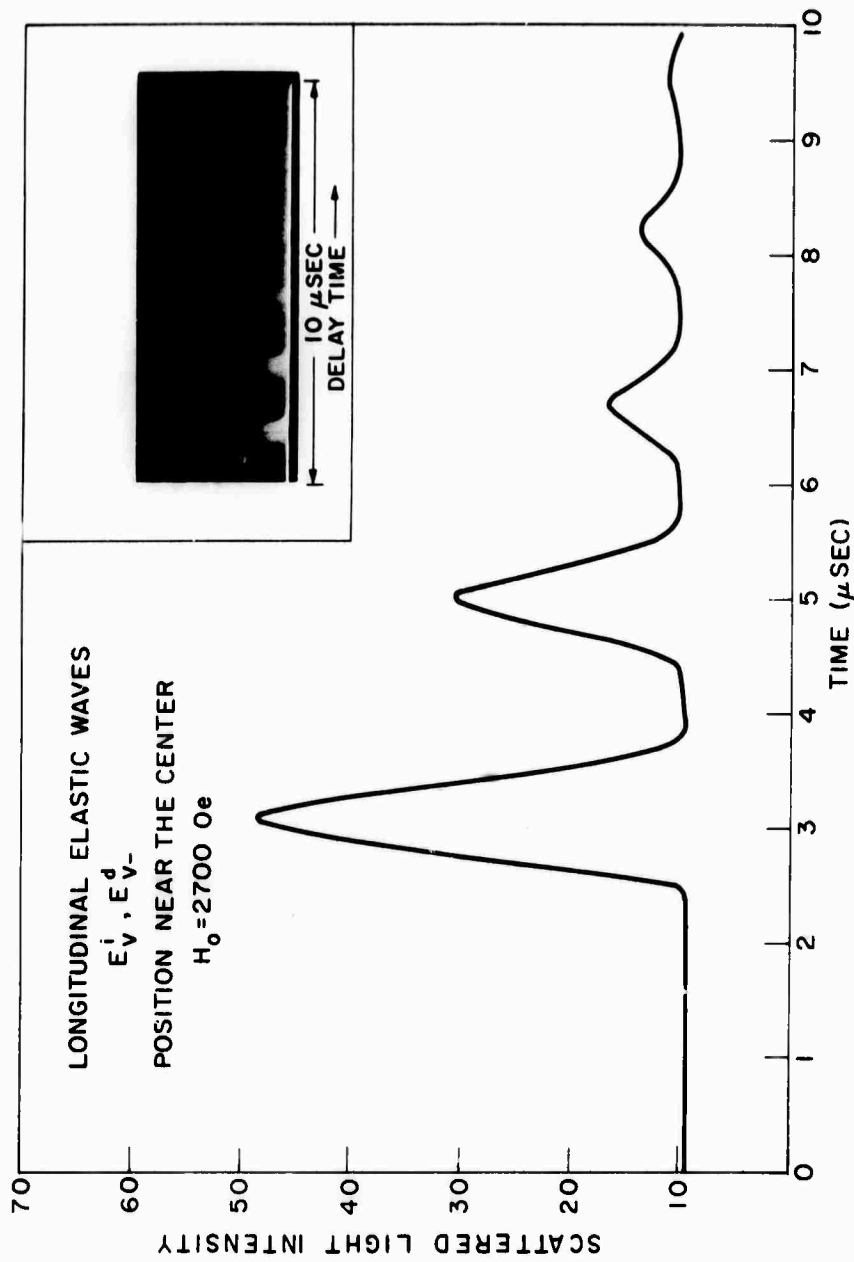


Fig. 5.7 Diffracted light pulses from a 1.5 GHz longitudinal elastic wave pulse propagating along a "22.5°" YIG bar. The graph was recorded with the signals from the PAR boxcar integrator. The insert is the scope trace.

The signs of the photoelastic constants are not known. From the measurements of the intensity of the diffracted light with an incident light polarized either horizontally (in the plane of incidence) or vertically (perpendicular to the plane of incidence), we obtain (from Eqs. (4.36) and (5.1)):

$$(P_{11}+3P_{12}-2P_{44})^2:(3P_{11}+P_{12}+2P_{44})^2:(-P_{11}+P_{12}+2P_{44})^2 = 55:4:1$$

If one assumes: $P_{11}:P_{12}:P_{44} = 25:75:(-41)$, then

$$(P_{11}+3P_{12}-2P_{44})^2:(3P_{11}+P_{12}+2P_{44})^2:(-P_{11}+P_{12}+2P_{44})^2 = 91:4:1$$

On the other hand, other possibilities exist such as:

$$P_{11}:P_{12}:P_{44} = 25:(-73):41$$

then

$$(P_{11}+3P_{12}-2P_{44})^2:(3P_{11}+P_{12}+2P_{44})^2:(P_{11}+P_{12}+2P_{44})^2 = 300:27.5:1$$

$$\text{or if } P_{11}:P_{12}:P_{44} = 25:73:41$$

then

$$(P_{11}+3P_{12}-2P_{44})^2:(3P_{11}+P_{12}+2P_{44}):(-P_{11}+P_{12}+2P_{44})^2 = 1.56:3.0:1$$

$$\text{or if } P_{11}:P_{12}:P_{44} = -25:73:41,$$

then

$$(P_{11}+3P_{12}-2P_{44})^2:(3P_{11}+P_{12}+2P_{44}):(-P_{11}+P_{12}+2P_{44})^2 = 2:1:5$$

From these results we conclude that it is most likely that:

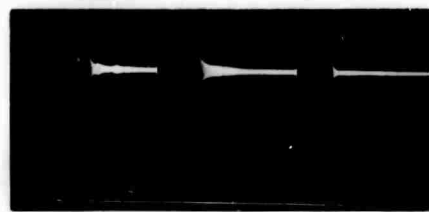
$$P_{11}:P_{12}:P_{44} = (0.025):(0.073):(-0.041).$$

We do not expect our measurements to be in good agreement with Dixon's since the total error in the measurements tends to become larger when linear combinations of the measured quantities are formed.

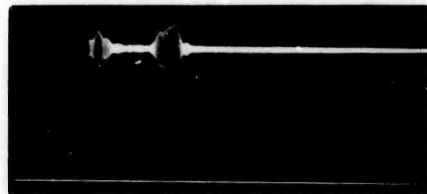
Nevertheless, in all cases using either horizontally or vertically polarized incident light, the component of the scattered light (either downshifted or upshifted in frequency) with polarization perpendicular to that of the incident light is always much smaller than the one with the same polarization as that of the incident light.

Next, the magnetic field was slowly decreased until the longitudinal crossover region occurred near the middle of the bar. Under these conditions $H'(z_{cr}^{\ell})$ is small and efficient longitudinal elastic wave/spin wave conversion occurred, as indicated by the strong attenuation of the elastic wave echoes observed with the microwave circuitry (Fig. 5. 8(b)). When the laser was focused on the crossover region, high intensity diffracted light was observed to coincide with the time of arrival of the longitudinal elastic waves at the crossover point, as is shown in the lower trace of Fig. 5. 8(c).

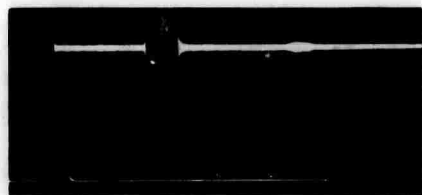
As observed in the experiments, the polarization of the diffracted light was perpendicular to that of the incident light only when the latter was either horizontally or vertically polarized. This indicates that $\Delta g \cong 0$ in Eq. (4. 47). There were no observable changes of the Bragg angle from that of the longitudinal elastic waves. This excludes the possibility that the scattering was due to shear elastic waves, for otherwise the Bragg angle would be almost twice as large. Furthermore, the downshifted diffracted light intensity was maximum when the incident light was horizontally polarized and minimum when the incident light was vertically polarized, the ratio of maximum to minimum diffracted light intensities being approximately 8. For the upshifted case, the reverse was true. Again this kind of asymmetry cannot be expected from shear elastic waves, but can be easily explained in terms



(a) $H_0 = 720 \text{ Oe}$



(b) $H_0 = 722.4 \text{ Oe}$



(c) $H_0 = 736 \text{ Oe}$

HORIZONTAL TRACE $1 \mu \text{ SEC/CM}$

Fig. 5.8 Scope traces indicated with signals from the microwave circuitry and the photomultiplier as a function of external magnetic field. The upper and lower traces are synchronized; the upper traces are from the microwave receiver and the lower traces are from the photomultiplier. The diffracted light signal is polarized at $\pi/2$ with respect to the incident light (E_H^i, E_{V-}^d). In (a), the upper trace indicates the first leakage pulse, and two longitudinal elastic echoes where amplitudes saturate the receiver. In (b), the longitudinal echoes are strongly attenuated due to the magnetoelastic coupling. In (c), the longitudinal echoes are still attenuated; the lower trace now indicates a strong diffracted light signal from coherent spin waves (compare the diffracted light pulse with that in Fig. 5.7).

of Eq. (4.47) if one assumes that f and $(g_{11} - g_{12} + 2g_{44})$ are of the same sign at 1150 nm. When the magnetic field was reversed, all the above situations remained unchanged in agreement with Eq. (4.47).

Figure 5.9 is a typical plot (in arbitrary units) of the intensity of the light diffracted from spin waves and elastic waves as a function of the external magnetic field; the intensity of the light diffracted from both waves was proportional to the microwave input power within the power range (10 to 200 mW) used in the experiment (Fig. 5.10). The incident light here was vertically polarized, the light spot position was approximately in the middle of the bar, and the diffracted light was upshifted in frequency. The polarization of the light diffracted from the spin waves was horizontal; from the elastic waves, vertical. There was negligible contribution from longitudinal elastic waves to the horizontally polarized diffracted light intensity, as supported both by the calculations and experiments done at higher magnetic fields. Specifically in this case, the polarization of the incident light and the frequency shift of the diffracted light were arranged so as to give the strongest possible diffracted light intensity, not only from spin waves (Eq. (4.47)), but also from longitudinal elastic waves (Eq. (5.1)). Note that the scale has been amplified by a factor of 5 in the case of much weaker vertically polarized diffracted light from the elastic waves. Also, the minimum and maximum of these two diffracted light intensities do not coincide due to the very small conversion region and the comparatively large size of the light spot. The minimum of the vertically polarized diffracted light is not exactly zero, which may be due to the non-zero magnetic field gradient at the crossover point caused either by a large chip in the sample at the opposite end of the

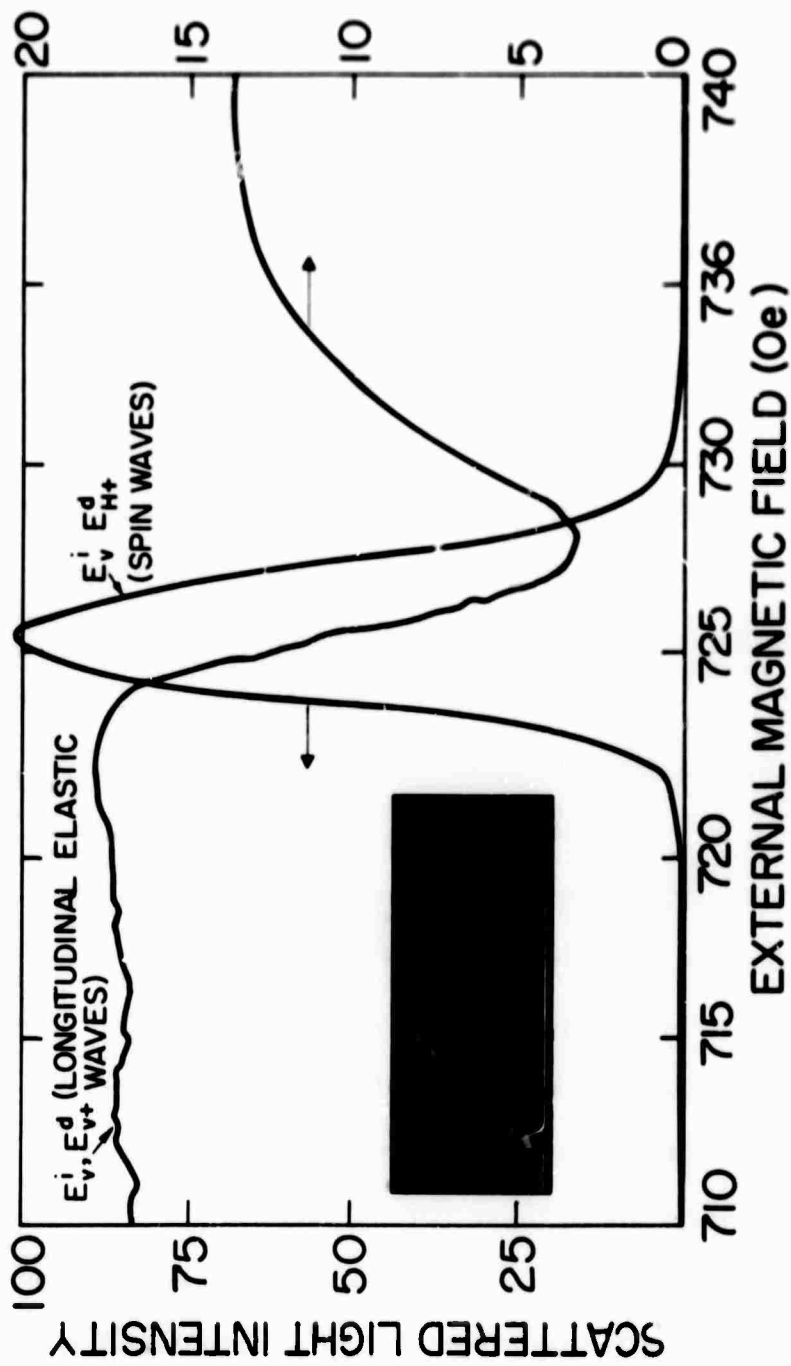


Fig. 5.9 Scattered light intensity (in arbitrary units) of spin waves and longitudinal elastic waves as a function of external magnetic field. The insert is the oscilloscope trace showing the peak intensity of the diffracted light pulse (compare with the diffracted light pulse of the scope trace in Fig. 5.7).

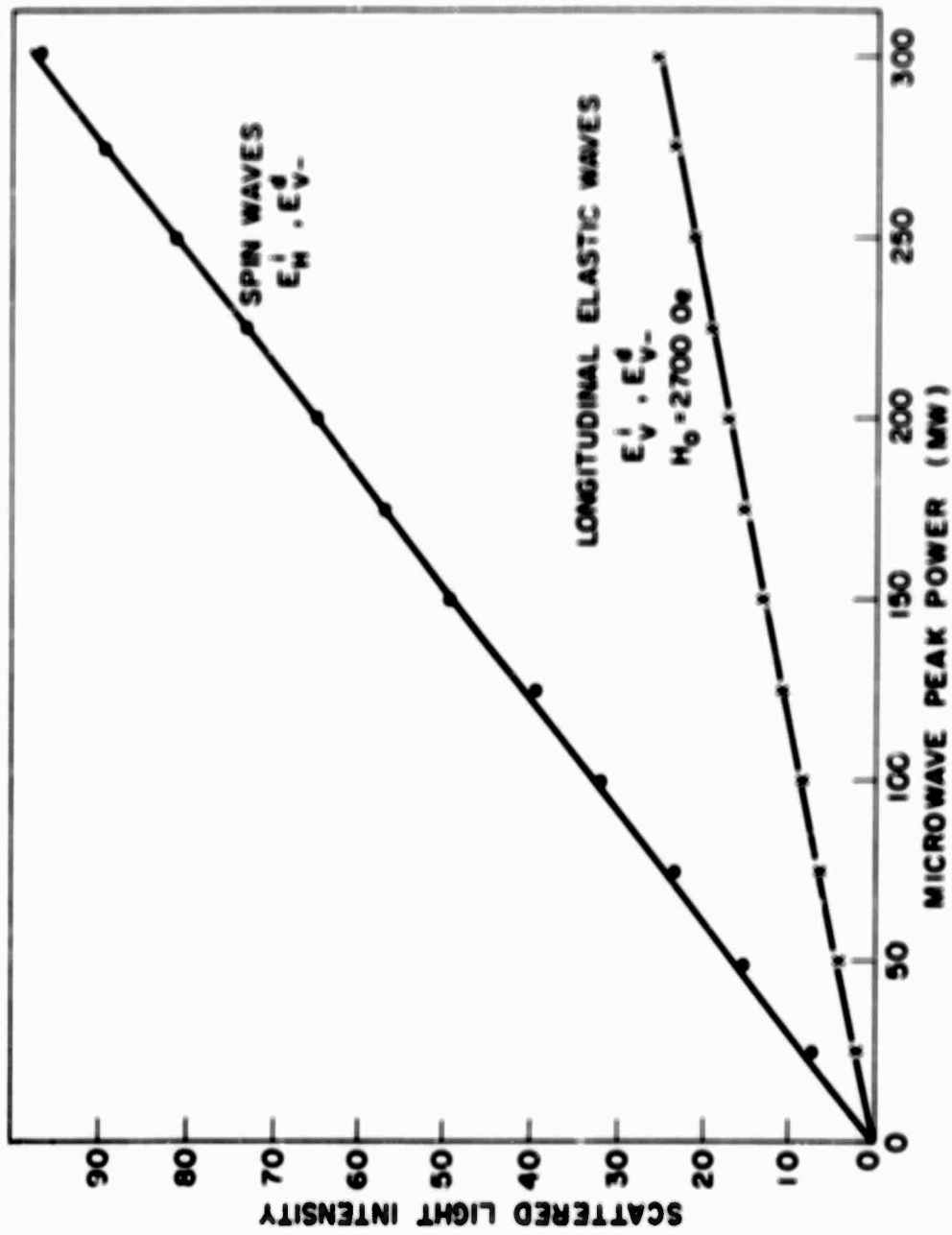


Fig. 5.10 Diffracted light intensity as a function of input microwave power.

transducer or by the transverse field gradients. The trailing edge of the curve labelled "longitudinal elastic waves" of Fig. 5.9 is, of course, due to residual conversion¹⁹ to spin wave form as the crossover point moves toward the end of the sample. In this case, the spin waves had already been cut off and did not diffract any light. Assuming full conversion from elastic waves into spin waves, and using the relative diffracted intensity of elastic waves and spin waves, with either horizontally polarized or vertically polarized incident light, we obtain, at $\lambda = 1150$ nm, either $f = 1.08 \times 10^{-4} \cdot \frac{1}{4}(g_{11} - g_{12} + 2g_{44}) \approx 2.15 \times 10^{-4}$ or vice versa (because the sign of $\frac{4f + (g_{11} - g_{12} + 2g_{44})}{4f - (g_{11} - g_{12} + 2g_{44})}$ could not be determined from the intensity data). Resolution of this ambiguity and the values of g_{mn} must await precise magneto-optic measurements of f and $(g_{11} - g_{12} + 2g_{44})$, e. g. from Faraday rotation and Voigt effect. We also observed the intensity of light diffracted from coherent spin waves as a function of the light position along the bar and external applied field strength. For spin waves of a fixed frequency, the strength of the external applied fields has to be of such a value that the light beam position coincides with the longitudinal crossover point. Therefore in principle one has a good way of measuring the internal field profile by using light scattering from coherent spin waves. Of course if the field gradient at the crossover point is large, weak conversion from elastic waves to spin waves occurs and the scattering intensity is reduced, as was indeed observed. Since there is a large chip on the sample, theoretical calculations of the internal field profile are not feasible. Therefore no results on internal field profile probing are presented here.

5.4 Measurements of Temporal Longitudinal Elastic/Spin Wave Conversion Efficiencies

Optical probing of longitudinal elastic/spin waves subjected to pulsed magnetic fields was used to measure the temporal longitudinal elastic/spin wave conversion efficiencies by directly observing the scattered light intensity from the converted spin waves. It is difficult to make the measurements with conventional microwave techniques whenever intrinsic non-uniform fields due to demagnetizing effects occur inside a ferrimagnetic sample. The experiments were performed under identical conditions and using the identical sample as in section 5.3. The sample used here, however, has a 38 Oe/Amp coil uniformly wound around it, except for a space near the center of the long axis where the light beam was focused. The lower trace of Fig. 5.11(a) shows the light pulse diffracted from coherent spin waves ($H_0 = 726$ Oe). The upper traces (synchronous with the lower traces) in Fig. 5.10 show a positive field pulse that is in the direction of the applied field. In Fig. 5.11(a) the small field pulse is applied after the spin waves cross the light beam and therefore has no effect on the diffracted light. In Fig. 5.11(b) the dc bias field is decreased by 15 Oe and the field pulse is increased by 15 Oe and is applied before the elastic waves are launched at the bar end. The result is that the elastic waves still convert to spin waves at the light beam position through a spatial gradient and therefore a diffracted light pulse from coherent spin waves can be seen, as in 5.11(a). Now the field pulse is increased by another 23 Oe while still being applied at the same time, as in Fig. 5.11(b). Therefore no spin waves could be observed at the original light beam position, as shown in the lower trace of Fig. 5.11(c). We then changed the timing of the field pulse

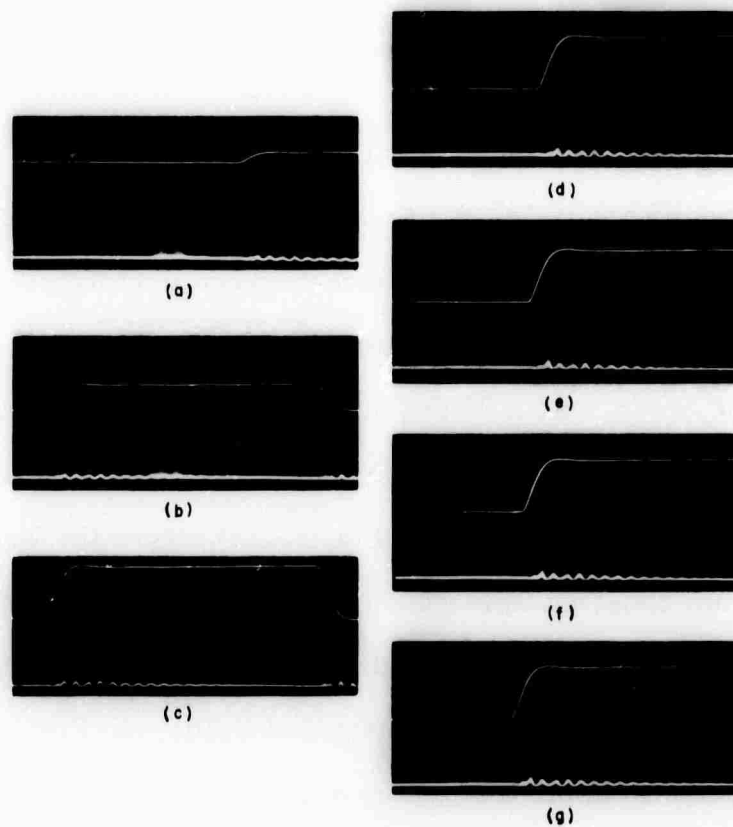


Fig. 5.11 Diffracted light intensity (E_v^i , E_{H+}^d) from coherent spin waves as a function of the timing of the pulsed bias field; the spin waves are generated through temporal conversion from longitudinal elastic waves (time scale $0.5 \mu\text{sec/cm}$). A full explanation is given in the text.

while maintaining its amplitude. In Figs. 5.11(d) through 5.11(g), the diffracted light signal was observed at a fixed delay following the application of the field pulse. Figure 5.12 is an expanded version of Fig. 5.11.

These two figures not only give further endorsement to the interpretation of the light scattering from coherent spin waves, as discussed in the last section, but also enable us to measure the efficiencies of temporal spin/longitudinal elastic wave conversion. The results are indicated in Fig. 5.13 where the field gradients are determined from the risetime and amplitudes of the field pulse. These results do not agree very well with the theory. The discrepancy may be caused by the non-uniform internal fields inside the sample.

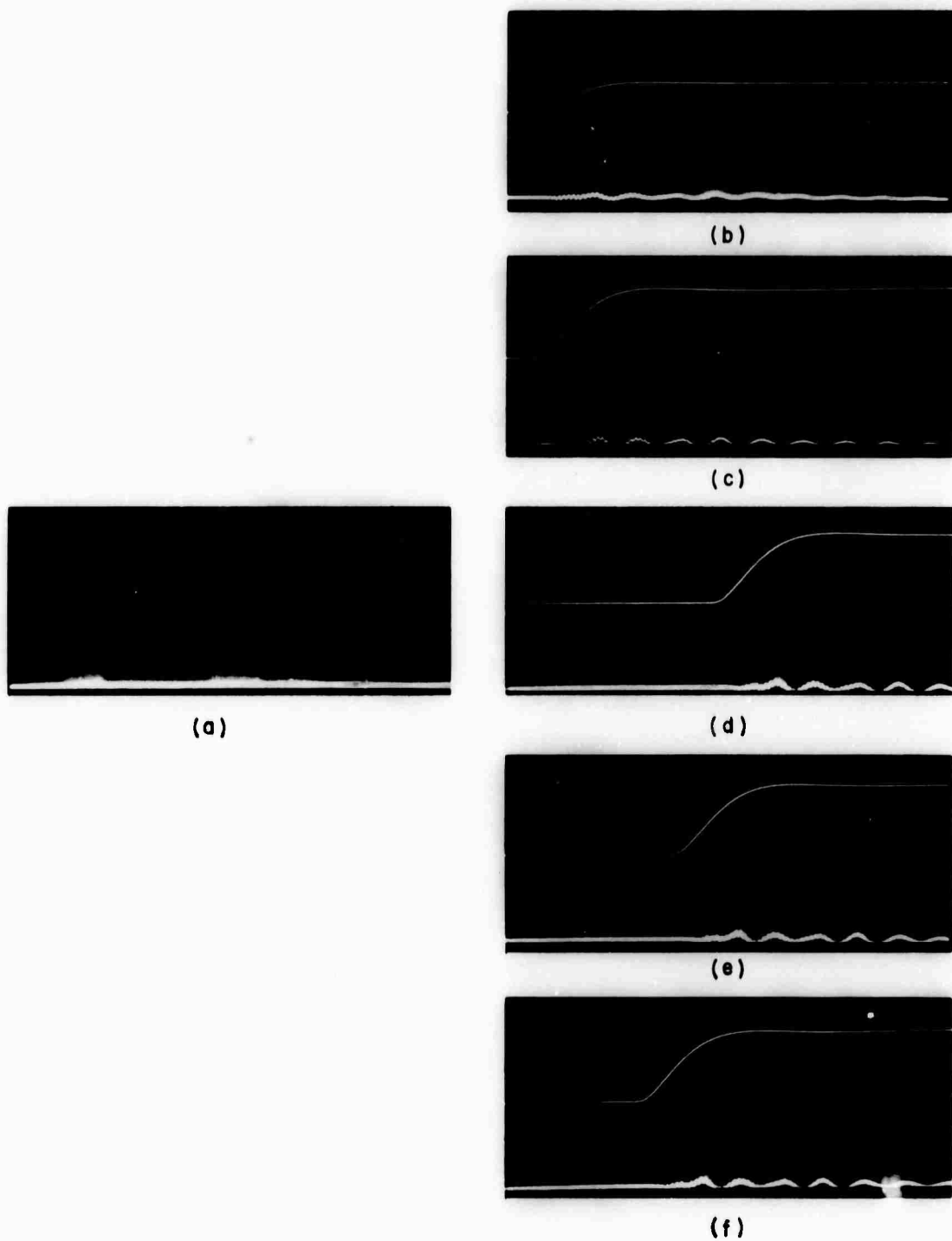


Fig. 5.12 (a) diffracted light pulses from longitudinal elastic waves (E_V^i, E_V^d) (time scale $0.5 \mu\text{sec/cm}$).
 (b) to (f) - an expanded version of Fig. 5.11 (E_V^i, E_{H+}^d) (time scale $0.2 \mu\text{sec/cm}$).

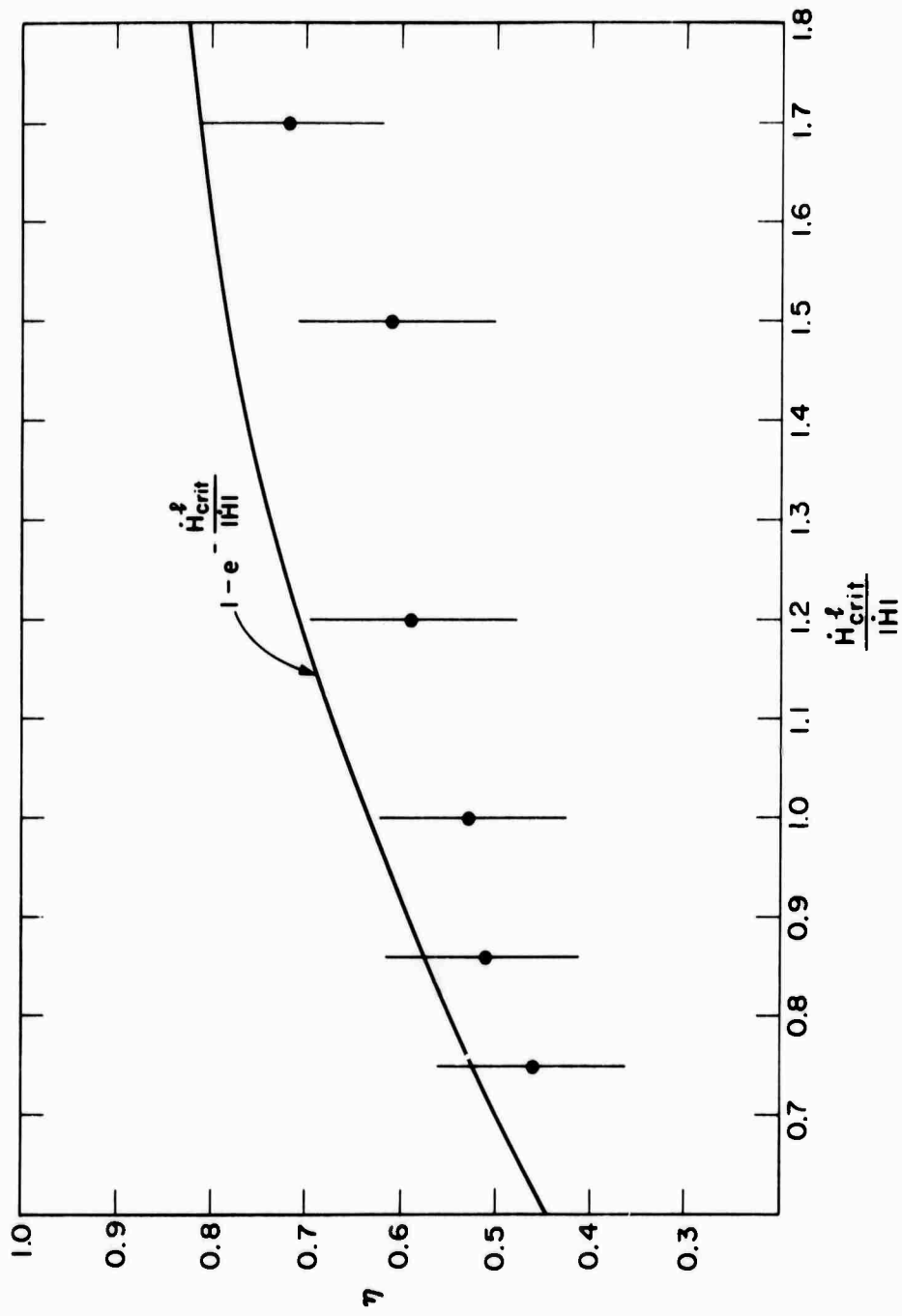


Fig. 5.13 Magnetoelastic (phonon \rightarrow magnon) conversion efficiency versus inverse temporal field gradient \dot{H}_{crit}^{ℓ} .

BLANK PAGE

Appendix I

Effective Anisotropy Fields and Small Anisotropy Tensor \vec{N}^{an} for Cubic Crystals

We here discuss the effective anisotropy fields and small signal anisotropy tensor \vec{N}^{an} for cubic crystals in a coordinate system in which the static magnetization \vec{M} is along the z-axis (referred hereon to the transformed coordinate system), but otherwise arbitrary with respect to the crystallographic directions.

In a coordinate system (ξ, η, ζ) with axes along the cube edges, the anisotropy energy density W_{an} of a cubic crystal can be written as:

$$W_{an} = \frac{K_1}{M^4} \sum_{\substack{\ell, m=1 \\ \ell > m}}^3 M_\ell^2 M_m^2 + \frac{K_2}{M^6} M_\xi^2 M_\eta^2 M_\zeta^2 \quad (A1.1)$$

As we are only concerned with the effective anisotropy field portion H_1^{an} which is at most linear in the transverse small signal magnetization components in the transformed coordinate system, the term of W_{an} containing K_2 in Eq. (A1.1) can be safely neglected. Equation (A1.1) can then be written as:

$$W_{an} \cong \frac{K_1}{M^4} \sum_{\substack{\ell, m=1 \\ \ell > m}}^3 M_\ell^2 M_m^2 = \frac{-K_1}{2M^4} \sum_{\ell=1}^3 M_\ell^4 + \frac{K_1}{2} \quad (A1.2)$$

Suppose the transformed coordinate system is oriented at the Euler Angles $(\varphi, \theta, 0)$ from the "cubic-edge" coordinate system. Expressing W_{an} in terms of the transformed coordinate system, one obtains:

$$W_{an} = \frac{K_1}{2} - \frac{K_1}{2M^4} \left[\sum_{\ell=1}^3 \sum_{f, i, j, k=1}^3 T_{\ell f} T_{\ell i} T_{\ell j} T_{\ell k} M_f M_i M_j M_k \right] \quad (A1.3)$$

where \vec{T} is given in Eq. (2.4). The effective anisotropy field in the transformed coordinate system (where the static magnetization \vec{M} is along the z-axis) can then be written down as:

$$\begin{aligned} H_i^{an} &= -\frac{1}{\mu_0} \frac{\partial W_{an}}{\partial M_i} = \frac{2K_1}{\mu_0 M^4} \sum_{\ell=1}^3 \sum_{f,j,k=1}^3 T_{\ell f} T_{\ell j} T_{\ell k} T_{\ell i} M_f M_j M_k \\ &= \frac{2K_1}{\mu_0 M^4} \left[\sum_{\ell=1}^3 T_{\ell i} T_{\ell 3}^3 M_3^3 + 3 \sum_{\ell=1}^3 T_{\ell i} T_{\ell 1} T_{\ell 3}^2 M_1 M_3^2 \right. \\ &\quad \left. + 3 \sum_{\ell=1}^3 T_{\ell i} T_{\ell 2} T_{\ell 3}^2 M_2 M_3^2 \right] + O(M_1^2, M_2^2, M_1 M_2) \end{aligned} \quad (A1.4)$$

Only terms which are at most linear in M_x and M_y are retained in Eq. (A1.4) and higher order terms like $O(M_1^2, M_2^2, M_1 M_2)$ are to be dropped. Furthermore, in the expressions H_1^{an} and H_2^{an} ($i = 1, 2$ in Eq. (A1.4)), the term $\frac{2K_1}{\mu_0 M^4} \sum_{\ell=1}^3 T_{\ell i} T_{\ell 3}^3 M_3^3$ ($i = 1, 2$) does not contribute to h^{an} in the small signal equations of motion Eq. (1.2). On the other hand, the term $\frac{2K_1}{\mu_0 M^4} \sum_{\ell=1}^3 T_{\ell 3}^4 M_3^3$ in H_3^{an} is the only one that enters the equations of motion and is in fact equal to H_M^{an} in Eq. (1.3a). We therefore write (using $M_3 \cong M$, $M_1 = m_1$, and $M_2 = m_2$):

$$h_1^{an} = \frac{2K_1}{\mu_0 M^2} \left(3 \sum_{\ell=1}^3 T_{\ell 1}^2 T_{\ell 3}^2 m_1 + 3 \sum_{\ell=1}^3 T_{\ell 1} T_{\ell 2} T_{\ell 3}^2 m_2 \right) \quad (A1.5a)$$

$$h_2^{an} = \frac{2K_1}{\mu_0 M^2} \left(3 \sum_{\ell=1}^3 T_{\ell 1} T_{\ell 2} T_{\ell 3}^2 m_1 + 3 \sum_{\ell=1}^3 T_{\ell 2}^2 T_{\ell 3}^2 m_2 \right) \quad (A1.5b)$$

$$H_{\mu}^{an} = H_3^{an} \cong \frac{2K_1}{\mu_0 M} \sum_{\ell=1}^3 T_{\ell 3}^4 \quad (A1.5c)$$

Recall the definition of the small signal anisotropy term \tilde{N} (Eq. (1.3b)

as:

$$h_i^{an} = \sum_{j=1}^2 -N_{ij}^{an} m_j \quad (i = 1, 2) \quad (A1.6)$$

Using (A1.5), (A1.6) and the \tilde{T} from Eq. (2.4) (with $\psi = 0$), one obtains:

$$N_{11}^{an} = + \frac{2K_1}{\mu_0 M^2} \left[-\frac{3}{2} \sin^2 2\theta \left(1 - \frac{1}{4} \sin^2 2\varphi \right) \right] \quad (A1.7a)$$

$$N_{22}^{an} = \frac{2K_1}{\mu_0 M^2} \left[-\frac{3}{2} \sin^2 \theta \sin^2 2\varphi \right] \quad (A1.7b)$$

$$N_{12}^{an} = N_{21}^{an} = \frac{2K_1}{\mu_0 M^2} \left[-\frac{3}{8} \sin \theta \sin 2\theta \sin 4\varphi \right] \quad (A1.7c)$$

$$H_3^{an} = H_M^{an} = \frac{2K_1}{\mu_0 M} \left[1 - \frac{1}{2} (\sin^2 2\theta + \sin^4 \theta \sin^2 2\varphi) \right] \quad (A1.8)$$

Since in the small signal equations of motion, \tilde{N}^{an} is always multiplied with the magnetization M and H_3^{an}/M , with m_1 or m_2 . In view of this, sometimes it is found convenient to define an effective \tilde{N}'^{an} such that H_3^{an}/M and \tilde{N}^{an} are combined as follows:

$$N_{11}'^{an} = \frac{H_3^{an}}{M} + N_{11}^{an} = \frac{2K_1}{\mu_0 M^2} \left\{ \left[1 - \frac{1}{2} (\sin^2 2\theta + \sin^4 \theta \sin^2 2\varphi) \right] - \frac{3}{2} \sin^2 2\theta \left(1 - \frac{1}{4} \sin^2 2\varphi \right) \right\} \quad (A1.9a)$$

$$N_{22}'^{an} = \frac{H_3^{an}}{M} + N_{22}^{an} = \frac{2K_1}{\mu_0 M^2} \left\{ \left[1 - \frac{1}{2} (\sin^2 2\theta + \sin^4 \theta \sin^2 2\varphi) \right] - \frac{3}{2} \sin^2 \theta \sin^2 2\varphi \right\} \quad (A1.9b)$$

$$N_{12}'^{an} = N_{21}'^{an} = N_{12}^{an} = N_{21}^{an} = \frac{2K_1}{\mu_0 M^2} \left[-\frac{3}{8} \sin \theta \sin 2\theta \sin 4\varphi \right] \quad (A1.9c)$$

Using this effective anisotropy tensor, \tilde{N}'^{an} , the internal magnetic field H_i in the small signal equations of motion is just the sum of the applied and demagnetizing fields only.

Appendix II

The First Order Magnetoelastic Constants for an Arbitrarily Oriented Coordinate System in Cubic Crystals

The first order (in strain) magnetoelastic constants, b_{fijk} pertaining to the small signal magnetoelastic equations of motion in an arbitrarily oriented coordinate system in cubic crystals, are derived here. The connection between the magnetoelastic constants b_{ijkl} defined in Eq. (1.3d) and b_{fijk} is also discussed.

In general, the first order (in strain) magnetoelastic energy density W_{me} of a cubic ferromagnet can be written in terms of the first order magnetoelastic constants b_{fijk} as:

$$W_{me} = \frac{1}{M^2} \sum_{f,i} \sum_{j,k} b_{fijk} M_f M_i S_{jk} \quad (A2.1)$$

$$(f, i, j \text{ and } k = 1, 2, 3)$$

where S_{jk} is the symmetrical finite strain tensor and therefore the magnetoelastic constants b_{fijk} have the symmetry properties:

$$b_{fijk} = b_{ifjk} = b_{fikj} = b_{ifkj} \quad (A2.2a)$$

With cubic symmetry, the b_{fijk} 's have the additional symmetry properties:

$$b_{fijk} = b_{jkfi} \quad (A2.2b)$$

Consequently there are at most 18 independent b_{fijk} 's for an arbitrarily oriented coordinate system in cubic crystals.

Since we are mainly concerned here with the small signal

equations of motion, the finite strain tensor S_{jk} can be approximated by the small signal strain tensor and can be written as:

$$S_{jk} \cong \frac{1}{2} \left(\frac{\partial \rho_j}{\partial x_k} + \frac{\partial \rho_k}{\partial x_j} \right) \quad (A2.3)$$

where $\vec{\rho}$ is the elastic displacement.

Suppose the transformed coordinate system is oriented at the Euler Angles $(\varphi, \theta, 0)$ with respect to the "cubic-edge" coordinate system. We now want to proceed and find the b_{fijk} 's in terms of the ordinary first order magnetoelastic constants b_1 and b_2 and the Euler Angles.

If W_{me} is expressed in the "cubic-edge" coordinate system there are only two different b_{fijk} , i. e., b_1 and b_2 since

$$b_1 = b_{iiii} \quad (i = 1, 2, 3) \quad (A2.4a)$$

$$\frac{1}{2} b_2 = b_{ijij} = b_{jiij} = b_{ijji} = b_{jiji} \quad (i \neq j, i, j = 1, 2, 3) \quad (A2.4b)$$

$$\text{All other } b_{fijk} = 0 \quad (A2.4c)$$

We can then rewrite (A2.1) as:

$$W_{me} = \frac{1}{M^2} \left[\sum_{\ell=1}^3 b_1 M_{\ell}^2 S_{\ell\ell} + \sum_{\substack{\ell, m=1 \\ \ell \neq m}}^3 b_2 M_{\ell} M_m S_{\ell m} \right] \quad (A2.5a)$$

or

$$W_{me} = \frac{b_2}{M^2} \left(\sum_{\ell=1}^3 M_{\ell}^2 S_{\ell\ell} + \sum_{\substack{\ell, m=1 \\ \ell \neq m}}^3 M_{\ell} M_m S_{\ell m} \right) + \frac{(b_1 - b_2)}{M^2} \sum_{\ell=1}^3 M_{\ell}^2 S_{\ell\ell} \quad (A2.5b)$$

Since the first term of Eq. (A2.5b) is invariant under rotations, only

the second term has to be transformed into the new coordinate system.

Let us define b'_{fijk} as the invariant part and b''_{fijk} as the transformed part of the b_{fijk} in the new coordinate system.

$$b'_{1111} = b'_{2222} = b'_{3333} = \frac{b_2}{M^2} \quad (A2.6a)$$

$$\begin{aligned} & b'_{1212} (b'_{1221}, b'_{2112} \text{ or } b'_{2121}) \\ &= b'_{1313} (b'_{1331}, b'_{3113}, \text{ or } b'_{3131}) \\ &= b'_{2323} (b'_{2332}, b'_{3223}, \text{ or } b'_{3232}) \\ &= \frac{b_2}{2M^2} \end{aligned} \quad (A2.6b)$$

$$\text{all other } (b')'s = 0 \quad (A2.6c)$$

and

$$b''_{fijk} = \frac{(b_1 - b_2)}{M^2} \sum_{\ell=1}^3 T_{\ell f} T_{\ell i} T_{\ell j} T_{\ell k} \quad (A2.7)$$

where \vec{T} is given in Eq. (2.4). Note that from Eq. (2.7), the b''_{fijk} 's are invariant with the interchange of all four indices and thus at most take 15 different values. The first order magnetoelastic constants b_{fijk} can then be easily obtained from Eqs. (A2.6) and (A2.7). The results are indicated in Table A2.1.

For small signal magnetoelastic problems, b_{fijk} 's are not very convenient to use. Now let us choose a particular set of the Euler Angles $(\varphi, \theta, 0)$ such that the z-axis of the transformed coordinate system coincides with the static magnetization \vec{M} , i.e., $\vec{M} = i_z M_3$. Then working in this particular coordinate system, we note from Eqs. (1.3d), (1.5) and (A2.1), that the only energy terms that contribute to the

Table A2.1

The First Order Magnetoelastic Constants b_{ijkl} in a Coordinate System at the Euler Angles $(\varphi, \theta, 0)$ from the "Cubic-Edge" Coordinate System

No.	Magnetoelastic Constants	Expression	Total No.	Remarks
(1)	b_{3333}	$\frac{b_2}{M^2} + \frac{(b_1 - b_2)}{M^2} \left[1 - \frac{1}{2}(\sin^2 2\theta + \sin^4 \theta \sin^2 2\varphi) \right]$	1	
(2)	$b_{3332} = b_{3323} = b_{3233} = b_{2333}$	$\frac{(b_1 - b_2)}{M^2} \left[-\frac{1}{4} \sin^3 \theta \sin 4\varphi \right]$	4	
(3)	$b_{3331} = b_{3313} = b_{3133} = b_{1333}$	$\frac{(b_1 - b_2)}{M^2} \left[-\frac{1}{2} \sin 2\theta (\cos 2\theta + \frac{1}{2} \sin^2 \theta \sin^2 2\varphi) \right]$	4	
(4)	$b_{3322} = b_{2233}$	$\frac{(b_1 - b_2)}{M^2} \left[\frac{1}{2} \sin^2 \theta \sin^2 2\varphi \right]$	2	
(5)	$b_{3311} = b_{1133}$	$\frac{(b_1 - b_2)}{M^2} \left[\frac{1}{2} \sin^2 2\theta (1 - \frac{1}{4} \sin^2 2\varphi) \right]$	2	
(6)	$b_{3232} = b_{3223} = b_{2323} = b_{2332}$	$\frac{b_2}{2M^2} + \frac{(b_1 - b_2)}{M^2} \left[\frac{1}{2} \sin^2 \theta \sin^2 2\varphi \right]$	4	
(7)	$b_{3131} = b_{3113} = b_{1331} = b_{1313}$	$\frac{b_2}{2M^2} + \frac{(b_1 - b_2)}{M^2} \left[\frac{1}{2} \sin^2 2\theta (1 - \frac{1}{4} \sin^2 2\varphi) \right]$	4	
(8)	$b_{3321} = b_{3312} = b_{3231} = b_{3213}$ $= b_{3132} = b_{3123} = b_{2331} = b_{2313}$ $= b_{2133} = b_{1332} = b_{1323} = b_{1233}$	$\frac{(b_1 - b_2)}{M^2} \left[-\frac{1}{8} (\sin \theta \sin 2\theta \sin 4\varphi) \right]$	12	Invariant with all 4 indices.

Table A2.1 (continued)

No.	Magnetoelastic Constants	Expression	Total No.	Remarks
(9)	$b_{3221} = b_{3212} = b_{3122} = b_{2321}$ $= b_{2312} = b_{2231} = b_{2213} = b_{2132}$ $= b_{2133} = b_{1322} = b_{1232} = b_{1223}$	$\frac{(b_1 - b_2)}{M^2} \left[\frac{1}{4} \sin 2\theta \sin^2 2\varphi \right]$	12	Invariant with all 4 indices.
(10)	$b_{3211} = b_{3121} = b_{3112} = b_{2311}$ $= b_{2131} = b_{2113} = b_{1321} = b_{1312}$ $= b_{1231} = b_{1213} = b_{1132} = b_{1123}$	$\frac{(b_1 - b_2)}{M^2} \left[-\frac{1}{8} (\sin 2\theta \cos \theta \sin 4\varphi) \right]$	12	Invariant with all 4 indices.
(11)	$b_{3222} = b_{2322} = b_{2232} = b_{2223}$	$\frac{(b_1 - b_2)}{M^2} \left[\frac{1}{4} \sin \theta \sin 4\varphi \right]$	4	
(12)	$b_{3111} = b_{1311} = b_{1131} = b_{1113}$	$\frac{(b_1 - b_2)}{M^2} \left[\frac{1}{2} \sin^2 \theta (\cos 2\theta - \frac{1}{2} \cos^2 \theta \sin^2 2\varphi) \right]$	4	
(13)	$b_{2211} = b_{1122}$	$\frac{(b_1 - b_2)}{M^2} \left[\frac{1}{2} \cos^2 \theta \sin^2 2\varphi \right]$	2	
(14)	$b_{2121} = b_{1221} = b_{2112} = b_{1212}$	$\frac{b_2}{2M^2} + \frac{(b_1 - b_2)}{M^2} \left[\frac{1}{2} \cos^2 \theta \sin^2 2\varphi \right]$	4	
(15)	$b_{2221} = b_{2212} = b_{2122} = b_{1222}$	$\frac{(b_1 - b_2)}{M^2} \left[\frac{1}{4} \cos \theta \sin 4\varphi \right]$	4	

Table A2.1 (continued)

No.	Magnetoelastic Constants	Expression	Total No.	Remarks
(16)	$b_{2111} = b_{1211} = b_{1121} = b_{1112}$	$\frac{(b_1 - b_2)}{M^2} \left[-\frac{1}{4} \cos^3 \theta \sin 4\phi \right]$	4	
(17)	b_{2222}	$\frac{b_2}{M^2} + \frac{(b_1 - b_2)}{M^2} \left[1 - \frac{1}{2} \sin^2 2\phi \right]$	1	
(18)	b_{1111}	$\frac{b_2}{M^2} + \frac{(b_1 - b_2)}{M^2} \left[1 - \frac{1}{2} (\sin^2 2\theta + \cos^4 \theta \sin^2 2\phi) \right]$	1	

effective magnetoelastic torque are those with one and only one M_3 .

Consequently we may define a small signal magnetoelastic energy density

w_{me} with the corresponding small signal magnetoelastic constants b_{ijk} as:

$$w_{me} = \frac{1}{M} \sum_{i,j,k=1}^3 b_{ijk} M_i \frac{\partial \rho_j}{\partial x_k} \quad (A2.8)$$

Rewrite (A2.1) as:

$$\begin{aligned} W_{me} &= \frac{M_3}{M^2} \sum_{j,k=1}^3 \left[b_{33jk} M_3 + 2 \sum_{i=1}^2 b_{3ijk} M_i \right] \cdot \frac{1}{2} \left(\frac{\partial \rho_j}{\partial x_k} + \frac{\partial \rho_k}{\partial x_j} \right) \\ &+ \frac{1}{M^2} \sum_{i,f=1}^2 \sum_{j,k=1}^3 b_{fijk} M_f M_i S_{jk} \\ &= \frac{M_3}{M^2} \sum_{j,k=1}^3 \left[b_{33jk} M_3 + 2 \sum_{i=1}^2 b_{3ijk} M_i \right] \frac{\partial \rho_j}{\partial x_k} \\ &+ \frac{1}{M^2} \sum_{i,f=1}^2 \sum_{j,k=1}^3 b_{fijk} M_f M_i S_{jk} \end{aligned} \quad (A2.9)$$

By comparing (A2.8) and (A2.9), and letting $M_3 \cong M$, one obtains

$$\begin{aligned} b_{3jk} &= b_{33jk} M \quad (j, k = 1, 2, 3) \\ b_{ijk} &= 2b_{3ijk} M \quad (i = 1, 2; k = 1, 2, 3) \end{aligned} \quad (A2.10)$$

and

$$b_{ijk} = b_{ikj} \quad (A2.11)$$

According to Eq. (A2.11), there are in general 18 different b_{ijk} 's with cubic symmetry, at most 12 independent b_{ijk} 's. These are the ones corresponding to the first 12 in Table A2.1. Using Eq. (A2.10) and Table A2.1, we obtain Table A2.2.

Table A2.2

The First Order Magnetoelastic Constants b_{ijk} in a Coordinate System at the Euler Angles $(\varphi, \theta, 0)$ from the "Cubic-Edge" Coordinate System

No.	Magnetoelastic Constants	Expression	Remarks
(1)	b_{333}	$\frac{b_2}{M} + \frac{(b_1-b_2)}{M} \left[1 - \frac{1}{2}(\sin^2 2\theta + \sin^4 \theta \sin^2 2\varphi) \right]$	
(2)	$2b_{332} = 2b_{323} = b_{233}$	$\frac{2(b_1-b_2)}{M} \left[-\frac{1}{4}(\sin^3 \theta \sin 4\varphi) \right]$	
(3)	$2b_{331} = 2b_{313} = b_{133}$	$\frac{2(b_1-b_2)}{M} \left[-\frac{1}{2} \sin 2\theta (\cos 2\theta + \frac{1}{2} \sin^2 \theta \sin^2 2\varphi) \right]$	
(4)	b_{322}	$\frac{(b_1-b_2)}{M} \left[\frac{1}{2} \sin^2 \theta \sin^2 2\varphi \right]$	
(5)	b_{311}	$\frac{(b_1-b_2)}{M} \left[\frac{1}{2} \sin^2 2\theta (1 - \frac{1}{4} \sin^2 2\varphi) \right]$	
(6)	$b_{223} = b_{232}$	$\frac{b_2}{M} + \frac{2(b_1-b_2)}{M} \left[\frac{1}{2} \sin^2 \theta \sin^2 2\varphi \right]$	Nonvanishing when $\theta = \varphi = 0$
(7)	$b_{131} = b_{113}$	$\frac{b_2}{M} + \frac{2(b_1-b_2)}{M} \left[\frac{1}{2} \sin^2 2\theta (1 - \frac{1}{4} \sin^2 2\varphi) \right]$	Nonvanishing when $\theta = \varphi = 0$
(8)	$2b_{321} = 2b_{312} = b_{213} = b_{231}$ $= b_{123} = b_{132}$	$\frac{2(b_1-b_2)}{M} \left[-\frac{1}{8}(\sin \theta \sin 2\theta \sin 4\varphi) \right]$	

Table A2.2 (continued)

No.	Magnetoelastic Constants	Expression	Remarks
(9)	$b_{221} = b_{212} = b_{122}$	$\frac{2(b_1 - b_2)}{M} \left[\frac{1}{4} \sin 2\theta \sin^2 2\phi \right]$	
(10)	$b_{211} = b_{121} = b_{112}$	$\frac{2(b_1 - b_2)}{M} \left[-\frac{1}{8} (\sin 2\theta \cos \theta \sin 4\phi) \right]$	
(11)	b_{222}	$\frac{2(b_1 - b_2)}{M} \left[\frac{1}{4} \sin \theta \sin 4\phi \right]$	
(12)	b_{111}	$\frac{2(b_1 - b_2)}{M} \left[\frac{1}{2} \sin 2\theta (\cos 2\theta - \frac{1}{2} \cos^2 \theta \sin^2 2\phi) \right]$	

Finally, using Eqs. (A2.7), (A2.10), and (2.5), we want to express specifically b_{233} and b_{133} in a coordinate system which lies at the Euler Angles (φ, θ, ψ) with respect to the "cubic-edge" coordinate system:

$$b_{233} = \frac{(b_1 - b_2)}{M} \left\{ \sin \psi \left[-\frac{1}{2} \sin 2\theta (\cos 2\theta + \frac{1}{2} \sin^2 \theta \sin^2 2\varphi) \right] \right. \\ \left. + \cos \psi \left[-\frac{1}{4} \sin^3 \theta \sin 4\varphi \right] \right\} \quad (A2.12)$$

$$b_{133} = \frac{(b_1 - b_2)}{M} \left\{ \sin \psi \left[-\frac{1}{4} \sin^3 \theta \sin 4\varphi \right] \right. \\ \left. - \cos \psi \left[-\frac{1}{2} \sin 2\theta (\cos 2\theta + \frac{1}{2} \sin^2 \theta \sin^2 2\varphi) \right] \right\} \quad (A2.13)$$

It may be interesting to note from Eqs. (A2.12), (A2.13), and Table A2.2 that the term $(b_{133}^2 + b_{233}^2)$ is independent of ψ and can be written as

$$b_{133}^2 + b_{233}^2 = \frac{(b_2 - b_1)^2}{M^2} \left[\frac{1}{4} \sin^2 4\theta + \sin^2 2\varphi \left(\frac{1}{2} \sin^2 \theta \sin 2\theta \sin 4\theta \right. \right. \\ \left. \left. + \frac{1}{4} \sin^2 2\varphi \sin^4 \theta \sin^2 2\theta \right) + \frac{1}{4} \sin^6 \theta \sin^2 4\varphi \right] \quad (A2.14)$$

It is also useful to express some b_{ijk} 's in the present coordinate system:

$$b_{232} = b_{223} = \frac{b_2}{M} + \frac{(b_1 - b_2)}{M} \left\{ \sin^2 \psi \left[\frac{1}{2} \sin^2 2\theta (1 - \frac{1}{4} \sin^2 2\varphi) \right] \right. \\ \left. + \sin 2\psi \left[\frac{1}{8} \sin \theta \sin 2\theta \sin 4\varphi \right] \right. \\ \left. + \cos^2 \psi \left[\frac{1}{2} \sin^2 \theta \sin^2 2\varphi \right] \right\} \quad (A2.15)$$

$$\begin{aligned}
 b_{131} = b_{113} = & \frac{b_2}{M} + \frac{b_1 - b_2}{M} \left\{ \sin^2 \psi \left[\frac{1}{2} \sin^2 \theta \sin^2 2\varphi \right] \right. \\
 & + \sin 2\psi \left[-\frac{1}{8} \sin \theta \sin 2\theta \sin 4\varphi \right] \\
 & \left. + \cos^2 \psi \left[\frac{1}{2} \sin^2 2\theta (1 - \frac{1}{4} \sin^2 2\varphi) \right] \right\}
 \end{aligned} \tag{A2.16}$$

$$\begin{aligned}
 b_{123} = b_{132} = b_{213} = b_{231} = & \frac{(b_1 - b_2)}{M} \cdot \\
 & \left\{ \sin^2 \psi \left[\frac{1}{8} \sin \theta \sin 2\theta \sin 4\varphi \right] \right. \\
 & + \sin 2\psi \sin^2 \theta \left[\frac{1}{4} \sin^2 2\varphi (1 + \cos^2 \theta) - \cos^2 \theta \right] \\
 & \left. + \cos^2 \psi \left[-\frac{1}{8} \sin \theta \sin 2\theta \sin 4\varphi \right] \right\}
 \end{aligned} \tag{A2.17}$$

BLANK PAGE

Appendix III

Dielectric Tensor of a "Cubic" Magnetic Medium⁵⁹

As pointed out by many authors^{59, 60} and discussed briefly in Chapter IV, magneto-optics can always be described, macroscopically, in terms of an effective dielectric tensor $\tilde{\epsilon}$ by setting the permeability $\mu = 1$. Once this $\tilde{\epsilon}$ is specified, one can substitute it into Maxwell's equations and proceed to solve the equations with suitable boundary conditions.

The dielectric tensor $\tilde{\epsilon}$ is defined, for the electric field of a single frequency ω_L , as

$$D_i(\omega_L) = \sum_{j=1}^3 \epsilon_{ij}(\omega_L) E_j(\omega_L) \quad (i=1, 2, 3) \quad (A3.1)$$

In a non-polarized medium, ϵ_{ij} is symmetrical; however, in a magnetically saturated medium with magnetization \vec{M} the generalized principle of symmetry of kinetic coefficient⁵⁹ requires:

$$\epsilon_{ij}(\vec{M}) = \epsilon_{ji}(-\vec{M}) \quad (A3.2)$$

Furthermore, since we are only concerned with sinusoidally varying fields, we can use complex notation, i. e., $\vec{D}, \vec{E} \sim e^{j\omega_L t}$. Therefore $\tilde{\epsilon}$ is now complex. Assuming media is optically lossless, $\tilde{\epsilon}$ must then be Hermitian.

$$\epsilon_{ij} = \epsilon_{ji}^* \quad (A3.3a)$$

where

$$\epsilon_{ij} = \epsilon'_{ij} + j\epsilon''_{ij} \quad (A3.3b)$$

Using (A3.1), (A3.2) and (A3.3), we then obtain:

$$\epsilon'_{ij}(\vec{M}) = \epsilon'_{ji}(\vec{M}) = \epsilon'_{ij}(-\vec{M}) \quad (\text{A3.4})$$

$$\epsilon''_{ij}(\vec{M}) = -\epsilon''_{ji}(\vec{M}) = -\epsilon''_{ij}(-\vec{M}) \quad (\text{A3.5})$$

Following (A3.4) and (A3.5), one concludes that ϵ'_{ij} is symmetrical and an even function of \vec{M} , while ϵ''_{ij} is antisymmetrical and an odd function of \vec{M} .

Using antisymmetrical unit tensor e_{ijk} , ϵ''_{ij} can then be written in terms of a vector \vec{G} .

$$\epsilon''_{ij} = e_{ijk} G_k \quad (\text{A3.6})$$

i. e.,

$$\begin{aligned} -\epsilon_{zy} &= \epsilon''_{yz} = G_x \\ -\epsilon_{xz} &= \epsilon''_{zx} = G_y \\ -\epsilon_{xy} &= \epsilon''_{xy} = G_z \end{aligned} \quad (\text{A3.7})$$

\therefore

$$\begin{aligned} D_i &= (\epsilon'_{ij} + i \epsilon''_{ij}) E_j \\ &= \epsilon'_{ij} E_j + i e_{ijk} G_k E_j \\ &= \epsilon'_{ij} E_j + c (\vec{E} \times \vec{G})_i \end{aligned} \quad (\text{A3.8})$$

A medium in which the relation between \vec{E} and \vec{D} is of this form is said to be gyrotropic.

As magneto-optical effects are fairly small, one can expand $\vec{\epsilon}$ into power series of \vec{M} or direction cosines $(\alpha_x, \alpha_y, \alpha_z)$ of M

$$G_k = \sum_{\mu=1}^3 f_{k\mu} \alpha_{\mu} + O(\alpha^3) \quad (\text{A3.9})$$

$$\epsilon'_{ij} = (\epsilon_o)_{ij} + \sum_{k, \ell=1}^3 g_{ijkl} \alpha_k \alpha_\ell + O(\alpha^4) \quad (A3.10a)$$

$$g_{ijkl} = g_{jikl} = g_{ijlk} = g_{jilk} \quad (A3.10b)$$

where $f_{k\mu}$ and g_{ijkl} contain all the symmetry properties of a crystal.

For example, when \vec{M} is along a $[001]$ direction in a cubic crystal, one can simplify (A3.9) by keeping only the linear term of α_z and using the symmetry properties of the crystal. One obtains, in the "cubic-edge" coordinate system (or principal axes):

$$\vec{\epsilon} = \begin{bmatrix} \epsilon_o & jf\alpha_z & 0 \\ -jf\alpha_z & \epsilon_o & 0 \\ 0 & 0 & \epsilon_i + g^2\alpha_z^2 \end{bmatrix} \quad (A3.11)$$

This is the well known dielectric tensor whose off-diagonal terms give rise to Faraday rotation and diagonal terms magnetic birefringent effect (Voigt effect).

In the case of spin wave scattering with the static magnetization \vec{M} along z-axis direction, one should keep all linear terms of α_x and α_y which may also come from second order or higher order terms such as $\alpha_x\alpha_z$, $\alpha_x\alpha_z^2$ and $\alpha_x\alpha_z^3$.

Notice from Eqs. (A3.9) and (A3.10) that $f_{k\mu}$ is a 2nd rank polar tensor and g_{ijkl} a 4th rank polar tensor.⁶⁹ For a cubic crystal (class m3m), like YIG, using the "cubic edge" coordinate system one obtains:⁶⁹

$$f_{k\mu} = f \delta_{k\mu} \quad (A3.12)$$

where $\delta_{k\mu}$ is the kronecker delta function, and

$$[g] = \begin{bmatrix} g_{11} & g_{12} & g_{12} & 0 & 0 & 0 \\ g_{12} & g_{11} & g_{12} & 0 & 0 & 0 \\ g_{12} & g_{12} & g_{11} & 0 & 0 & 0 \\ 0 & 0 & 0 & g_{44} & 0 & 0 \\ 0 & 0 & 0 & 0 & g_{44} & 0 \\ 0 & 0 & 0 & 0 & 0 & g_{44} \end{bmatrix} \quad (A3.13)$$

where g_{ijkl} is written in the matrix form as in the case of the photo-elastic tensor in Eq. (4.25a). The higher order terms which contain a first order term of α_x or α_y such as $\alpha_z^2 \alpha_x$ and $\alpha_z^3 \alpha_x$ do not exist in a cubic crystal and therefore need not be considered. In a crystal with less symmetry, where terms like $\alpha_z^2 \alpha_x$ and $\alpha_z^3 \alpha_x$ do exist, we can always lump them into effective g_{mn} or f .

Combining Eqs. (A3.6) (A3.9), and (A3.10a), the small change of the dielectric tensor, $\delta\epsilon_{ij} = \delta\epsilon'_{ij} + j\delta\epsilon''_{ij}$, can be expressed as:

$$\begin{bmatrix} \delta\epsilon'_{xx} \\ \delta\epsilon'_{yy} \\ \delta\epsilon'_{zz} \\ \delta\epsilon'_{yz} \\ \delta\epsilon'_{zx} \\ \delta\epsilon'_{xy} \end{bmatrix} = \begin{bmatrix} g_{11} & g_{12} & g_{12} & 0 & 0 & 0 \\ g_{12} & g_{11} & g_{12} & 0 & 0 & 0 \\ g_{12} & g_{12} & g_{11} & 0 & 0 & 0 \\ 0 & 0 & 0 & g_{44} & 0 & 0 \\ 0 & 0 & 0 & 0 & g_{44} & 0 \\ 0 & 0 & 0 & 0 & 0 & g_{44} \end{bmatrix} \begin{bmatrix} \alpha_x^2 \\ \alpha_y^2 \\ \alpha_z^2 \\ \alpha_y \alpha_z \\ \alpha_z \alpha_x \\ \alpha_x \alpha_y \end{bmatrix} \quad (A3.14)$$

where $\delta\epsilon'_{ij} = \delta\epsilon'_{ji}$.

$$\begin{bmatrix} \delta\epsilon_{xx}'' \\ \delta\epsilon_{yy}'' \\ \delta\epsilon_{zz}'' \\ \delta\epsilon_{yz}'' \\ \delta\epsilon_{zx}'' \\ \delta\epsilon_{xy}'' \end{bmatrix} = \begin{bmatrix} 0 & 0 & 0 \\ 0 & 0 & 0 \\ 0 & 0 & 0 \\ f & 0 & 0 \\ 0 & f & 0 \\ 0 & 0 & f \end{bmatrix} \begin{bmatrix} \alpha_x \\ \alpha_y \\ \alpha_z \end{bmatrix} \quad (\text{A3.15})$$

where $\delta\epsilon_{ij}'' = -\delta\epsilon_{ji}''$. The quantity f is related to the Faraday effect, while the matrix g_{mn} is related to the birefringence effect. Besides, f and g_{mn} , in general, are a function of optical angular frequency ω_L or wavelength λ .

The derivation here, following Landau,⁵⁹ is similar to that of Auld and Wilson,⁵⁶ but the result is quite different. They failed to take account of the terms g_{mn} in Eq. (A3.14); therefore the effect of α_x on $\delta\epsilon_{xz}$ is nil. We will see that these terms are essential in interpreting our experimental results as well as Collins and Wilson's⁵⁷ "anomalous" experimental observation. Besides, the origin of g comes from birefringence. In an experiment like coherent spin wave light scattering, by looking at the geometry of the interaction one would expect the scattered light to depend as much on α_x through the birefringence effect as on α_y through Faraday rotation.⁸¹

BLANK PAGE

REFERENCES

1. H. F. Tiersten, "Coupled Magnetomechanical Equations for Magnetically Saturated Insulators," *J. Math. Phys.* 5, 1298 (1964).
2. W. F. Brown, Jr., Magnetoelastic Interactions, Springer-Verlag New York Inc. (1966).
3. D. E. Eastman, "Ultrasonic Study of First-Order and Second-Order Magnetoelastic Properties of Yttrium Iron Garnet," *Phys. Rev.* 148, 530 (1966).
4. B. A. Auld, "Nonlinear Interactions of Spin Waves and Elastic Waves" in Advances in Microwaves, Vol. 3, Academic Press, Inc., New York (1968).
5. F. R. Morgenthaler, "Small Signal Power and Momentum Theorems for a Magnetoelastic Ferromagnet," Technical Report 14, Microwave and Quantum Magnetism Group, M.I.T. (1967).
6. F. R. Morgenthaler, "Magnetoelastic Wave Propagation in Time Varying Magnetic Fields," in Recent Advances in Engineering Science, Ed. A. C. Eringen, Gordon and Breach, New York (1970).
7. L. R. Walker, "Magnetostatic Modes in Ferromagnetic Resonance," *Phys. Rev.* 105, 390 (1957).
8. S. M. Rezende and F. R. Morgenthaler, "Magnetoelastic Waves in Time Varying Magnetic Fields I - Theory and II - Experiments," *J. Appl. Phys.* 40, 524 (1969).
9. J. R. Eshbach, "Spin-Wave Propagation and the Magnetoelastic Interaction in Yttrium Iron Garnet," *J. Appl. Phys.* 34, 1298 (1963).
10. W. Strauss, "Magnetoelastic Waves in Yttrium Iron Garnet," *J. Appl. Phys.* 36, 118 (1965).
11. E. Schlömann and R. I. Joseph, "Generation of Spin Waves in Nonuniform Magnetic Fields. III. Magnetoelastic Interaction," (Erratum in JAP 36, 875) *J. Appl. Phys.* 35, 2382 (1964).
12. F. R. Morgenthaler, S. M. Rezende, H. L. Hu and A. Platzker, "Spin-Longitudinal and Spin-Shear Elastic Wave Conversion," *Appl. Phys. Letters* 16, 133 (1970).
13. E. Schlömann and R. I. Joseph, "Stable Spin-Wave Trajectories," *J. Appl. Phys.* 38, 1238 (1967).

14. P. de Santis, "Evidence of Longitudinal Magnetoelastic Waves in YIG Rods," *Appl. Phys. Letters* 13, 9 (1968).
15. F. R. Morgenthaler, "A Figure of Merit for Magnon-Elevation and Elastic Wave Conversion in YIG," *IEEE Ultrasonics Symposium*, St. Louis, Missouri, September 1969, Paper L7 (unpublished).
16. A. E. Clark and R. E. Strakna, "Elastic Constants of Single-Crystal YIG," *J. Appl. Phys.* 31, 1172 (1961).
17. H. Goldstein, *Classical Mechanics*, Addison-Wesley, Reading, Massachusetts (1950).
18. B. A. Auld, J. H. Collins and H. R. Zapp, "Signal Processing in a Non-periodically Time-Varying Magnetoelastic Medium," *Proc. IEEE* 56, 258 (1968).
19. H. L. Hu, S. M. Rezenda, and F. R. Morgenthaler, "Measurements of Longitudinal Elastic-Wave/Spin-Wave Conversion Efficiencies in an Axially Magnetized YIG Rod," *J. Appl. Phys.* 41, 1417 (1970).
20. S. M. Rezende, "Magnetoelastic and Magnetostatic Waves in Time-Varying Magnetic Fields," Ph. D. Dissertation, Department of Electrical Engineering, M. I. T. (1967). Available as Microwave and Quantum Magnetics Group Technical Report No. 19, 1967.
21. E. K. Kirchner, L. F. Donaghey, F. A. Olson, and B. A. Auld, "Analysis of Magnetoelastic Conversion Efficiency," *J. Appl. Phys.* 37, 988 (1966).
22. A. Sommerfeld, *Electrodynamics*, Academic Press, Inc., New York, (1952), p. 82.
23. Ernst Schlömann, "Properties of Magnetic Materials with a Nonuniform Saturation Magnetization. I. General Theory and Calculation of the Static Magnetization," *J. Appl. Phys.* 38, 5027 (1967).
24. B. A. Auld, J. H. Collins and D. C. Webb, "Excitation of Magnetoelastic Waves in YIG Delay Lines," *J. Appl. Phys.* 39, 1598 (1968).
25. E. Schlömann, R. I. Joseph and T. Kohane, "Generation of Spin Waves in Nonuniform Magnetic Fields, with Application to Magnetic Delay Lines," *Proc. IEEE* 53, 1495 (1965).
26. W. Strauss and F. G. Eggers, "Evidence for Polarization Reversal of Magnetoelastic Waves," *Appl. Phys. Letters* 6, 18 (1965).
27. E. G. Spencer, R. T. Denton and R. P. Chambers, "Temperature Dependence of Microwave Acoustic Losses in Yttrium Iron Garnet," *Phys. Rev.* 125, 1950 (1962).

28. W. Strauss, "Elastic and Magnetoelastic Waves in Yttrium Iron Garnet," *Proc. IEEE* 53, 1485 (1965).
29. J. D. Adam, "Frequency Translation of Longitudinal Magnetoelastic Waves in YIG," *J. Appl. Phys.* 40, 810 (1969).
30. R. L. Comstock and P. E. Wigen, "Shear and Longitudinal Magnetoelastic Waves in Transversely Magnetized Rods," *J. Appl. Phys.* 36, 2426 (1965).
31. F. R. Morgenthaler, "Phase-Velocity Modulated Magnetoelastic Waves," *J. Appl. Phys.* 37, 3326 (1966).
32. L. Brillouin, "Diffusion de la lumière et des rayons X par un corps transparent homogène," *Ann. Phys. (France)* 17 88 (1922).
33. E. Gross, "Change of Wavelength of Light due to Elastic Heat Waves at Scattering in Liquids," *Nature* 126, 201 (1930).
34. P. Debye and F. W. Sears, "On the Scattering of Light by Supersonic Waves," *Proc. Nat. Acad. Sci. (USA)* 18, 409 (1932).
35. R. Lucas and P. Biquard, "Optical Properties of Solids and Liquids under Ultrasonic Vibrations," *J. Phys. Radium* 3, 464 (1932).
36. C. V. Raman, "A New Radiation," *Indian J. Phys.* 2, 387 (1928).
37. R. Peierls, *Quantum Theory of Solids*, Oxford University Press, New York (1955). See also references 45 and 46.
38. C. V. Raman and N. S. N. Nath, "The Diffraction of Light by Sound Waves of High Frequency, Parts I and II," *Proc. Ind. Acad. Sci. A2*, 406, 413 (1935).
39. G. W. Willard, "Criteria for Normal and Abnormal Ultrasonic Light Diffraction Effects," *J. Acoust. Soc. Amer.* 21, 101 (1949).
40. S. M. Rytov, *Zh. Eksperim. i Teor. Fiz.* 33, 514, 669 (1957).
41. G. B. Benedek and K. Fritsch, "Brillouin Scattering in Cubic Crystals," *Phys. Rev.* 149, 647 (1966).
42. L. L. Hope, "Brillouin Scattering in Birefringent Media," *Phys. Rev.* 166, 883 (1968).
43. W. R. Klein and B. D. Cook, "Unified Approach to Ultrasonic Light Diffraction," *IEEE Trans.* SU-14, 123 (1967).
44. Allan Griffin, "Brillouin Light Scattering from Crystals in the Hydrodynamic Region," *Rev. Mod. Phys.* 40, 167 (1968).

45. M. Born and E. Wolf, Principles of Optics, Pergamon Press, Oxford (1964).
46. M. Born and K. Huang, Dynamical Theory of Crystal Lattices, Clarendon Press, Oxford, (1954).
47. A. Yariv, "Quantum Theory for Parametric Interactions of Light and Hypersound," IEEE Trans. QE-1, 28 (1965).
48. R. Loudon, "Theory of the First-Order Raman Effect in Crystals," Proc. Roy. Soc. A. 275, 218 (1963).
49. P. A. Fleury, "Light Scattering as a Probe of Phonons and Other Excitation," in Physical Acoustics: Principles and Methods, Vol. VI, Ed. by W. P. Mason and R. N. Thurston, Academic Press, New York (1970).
50. M. G. Cohen and E. I. Gordan, "Acoustic Beam Probing Using Optical Techniques," Bell Sys. Tech. J. 44, 693 (1965).
51. C. F. Quate, C. D. W. Wilkinson and D. K. Winslow, "Interaction of Light and Microwave Sound," IEEE Proc. 53, 1604 (1965).
52. R. W. Dixon, "Acoustooptic Interactions and Devices," IEEE Trans. ED-17, 229 (1970).
53. R. Adler, "Interaction between Light and Sound," IEEE Spectrum 43 (May 1967).
54. A. Korpel, R. Adler, and P. Desmanes, "A Television Display Using Acoustic Deflection and Modulation of Coherent Light," Proc. IEEE 54, 1429 (1966).
55. R. W. Damon, W. T. Maloney and D. H. McMahon, "Interaction of Light with Ultrasound: Phenomena and Applications," in Physical Acoustics: Principles and Methods, Vol. VII, Ed. by W. P. Mason and R. N. Thurston, Academic Press, New York (1970).
56. B. A. Auld and D. A. Wilson, "Bragg Scattering of Infrared Radiation from Coherent Spin Waves," J. Appl. Phys. 38, 3331 (1967).
57. J. H. Collins and D. A. Wilson, "Optical Probing of Magneto-static Modes in YIG Delay Lines," Appl. Phys. Letters 12, 331 (1968).
58. A. W. Smith, "Optical Probing of Magnetoelastic Waves," in Light Scattering Spectra of Solids, Ed. by G. B. Wright, Springer-Verlag New York Inc. (1969).
59. L. D. Landau, and E. M. Lifshitz, Electrodynamics of Continuous Media, Pergamon Press Inc., New York (1960).

60. P. S. Pershan, "Magneto-Optical Effects," J. Appl. Phys. 38, 1482 (1967).
61. See, for example, P. M. Morse and H. Feshbach, Methods of Theoretical Physics, McGraw-Hill, New York (1953).
62. M. G. Cohen and E. I. Gordon, "Acoustic Scattering of Light in a Fabry-Perot Resonator," Bell Sys. Tech. J. 45, 945 (1966).
63. See, for example, A. Sommerfeld, Optics, Academic Press, New York (1949).
64. D. H. McMahon, "Relative Efficiency of Optical Bragg Diffraction as a Function of Interaction Geometry," IEEE Trans. SU-16, 41 (1969).
65. E. I. Gordon, "A Review of Acoustooptical Deflection and Modulation Devices," Proc. IEEE 54, 1391 (1966).
66. W. T. Maloney, G. Meltz and R. L. Gravel, "Optical Probing of the Fresnel and Fraunhofer Regions of a Rectangular Acoustic Transducer," IEEE Trans. SU-15, 167 (1968).
67. R. W. Dixon, "Acoustic Diffraction of Light in Anisotropic Media," Symposium on Modern Optics, Polytechnic Institute of Brooklyn, New York, March 22-24, 1967; IEEE QE-3, 85 (1967).
68. J. F. Nye, Physical Properties of Crystals, Oxford University Press, New York (1957), pp 305-309.
69. W. P. Mason, Crystal Physics of Interaction Processes, Academic Press, New York (1966).
70. E. G. Spencer, P. V. Lenzo, and A. A. Ballman, "Dielectric Materials for Electrooptic, Elastooptic, and Ultrasonic Device Applications," Proc. IEEE 55, 2074 (1967).
71. R. W. Dixon and H. Matthews, "Diffraction of Light by Elastic Waves in YIG," Appl. Phys. Letters 10, 195 (1967).
72. R. W. Dixon, "Optical Investigation of Magnetically Induced Elastic-Wave Dispersion in YIG," J. Appl. Phys. 38, 3634 (1967).
73. R. W. Dixon, "Photoelastic Properties of Selected Materials and Their Relevance for Applications to Acoustic Light Modulators and Scanners," J. Appl. Phys. 38, 5149 (1967).
74. A. W. Smith, "Diffraction of Light by Magnetoelastic Waves," Appl. Phys. Letters 11, 7 (1967).
75. A. W. Smith, "Diffraction of Light by Magnetoelastic Waves," IEEE Trans. SU-15, 161 (1968).

76. A. W. Smith, "Optical Probing of Magnetoelastic Waves," Phys. Rev. Letters 20, 334 (1968).
77. B. A. Auld and D. A. Wilson, "Spin and Acoustic Bragg Diffraction in Longitudinal Magnetoelastic Waves," Appl. Phys. Letters 11, 368 (1967).
78. H. L. Hu and F. R. Morgenthaler, "Strong Infrared Light Scattering from Coherent Spin Waves in Yttrium Iron Garnet," to be published.
79. G. B. Desormiere, L. C. R. Thomson and H. LeGall, "Magneto-Optical Effects in Transparent Media under Inhomogeneous Magnetization," International Conference of Magnetism, Grenoble, France, 1970, Paper Lu E-3.
80. E. G. H. Lean, "Studies of Microwave Shear Waves in Solids," Ph.D. Dissertation, Stanford University (1967). Available as W. W. Hansen Labs of Physics, M. L. Report No. 1543.
81. D. A. Wilson, "Bragg Diffraction of Light from Magnetostatic and Magnetoelastic Waves," Ph.D. Dissertation, Stanford University (1970). Available as W. W. Hansen Labs of Physics, M. L. Report No. 1836.
82. L. K. Anderson and B. J. McMurtry, "High Speed Photodetectors," Proc. IEEE 54, 1335 (1966).
83. Ernst Schlömann, "Spin-Wave Spectroscopy," in Advances in Quantum Electronics, Columbia University Press (1961).
84. J. R. Eshbach, "Spin-Wave Propagation and the Magnetoelastic Interaction in Yttrium Iron Garnet," Phys. Rev. Letters 8, 357 (1962).
85. M. F. Lewis, "Excitation of Longitudinal Magnetoelastic Waves in Axially Magnetized YIG Rods," J. Appl. Phys. 41, 2505 (1970).

BIOGRAPHICAL NOTE

The author was born January 7, 1943, in Shanghai, China. He attended high schools in Taiwan, and received the B. S. in Electrical Engineering (top of the class) from National Taiwan University, Taipei, Taiwan, Republic of China, in June, 1964. After a year of military service as a communications officer in the Chinese Air Force, he enrolled in the Electrical Engineering Department at M. I. T. in September, 1965, and received the S. M. and E. E. degrees in June, 1967. Since 1965 he has been a research assistant in the Microwave and Quantum Magnetics Group at M. I. T. He is a co-author of three publications, entitled:

1. Spin-Longitudinal and Spin-Shear Elastic Wave Conversion in an Axially Magnetized YIG Rod - by F. R. Morgenthaler, S. M. Rezende, H. L. Hu, and A. Platzker, Appl. Phys. Letters 16, 133 (1970).
2. Measurements of Longitudinal Elastic Wave/Spin Wave Conversion Efficiencies in an Axially Magnetized YIG Rod - by H. L. Hu, S. M. Rezende, and F. R. Morgenthaler, J. Appl. Phys. 41, 1417 (1970).
3. Strong Infrared Light Scattering from Coherent Spin Waves in Yttrium Iron Garnet - by H. L. Hu and F. R. Morgenthaler, to be published in Appl. Phys. Letters.

He is a student member of IEEE and the Optical Society of America, and an associate member of Sigma Xi.

Unclassified

Security Classification

DOCUMENT CONTROL DATA - R & D

(Security classification of title, body of abstract and indexing annotation must be entered when the overall report is classified)

1. ORIGINATING ACTIVITY (Corporate author) Massachusetts Institute of Technology, Microwave and Quantum Magnetics Group/Crystral Physics Laboratory, Dept. of Elec. Eng. and Ctr. for Materials Science and Engineering. Cambridge, Mass. 02139		2a. REPORT SECURITY CLASSIFICATION Unclassified	
3. REPORT TITLE Steerable Volume and Surface Spin Waves in Ferrimagnetic Films		2b. GROUP	
4. DESCRIPTIVE NOTES (Type of report and inclusive dates) Semi-Annual Technical Report August 1, 1970 - February 1, 1971			
5. AUTHOR(S) (First name, middle initial, last name) Morgenthaler, Frederic R.			
6. REPORT DATE March 15, 1971	7a. TOTAL NO. OF PAGES 96	7b. NO. OF REFS 85	
8a. CONTRACT OR GRANT NO. DAHC 15 70 C 0190	8b. ORIGINATOR'S REPORT NUMBER(S) Semi-Annual Technical Report No. 2		
8c. PROJECT NO.	9a. OTHER REPORT NO(S) (Any other numbers that may be assigned this report)		
10. DISTRIBUTION STATEMENT			
11. SUPPLEMENTARY NOTES		12. SPONSORING MILITARY ACTIVITY Advanced Research Projects Agency Arlington, Va. 22209	
13. ABSTRACT			

14.

KEY WORDS

LINK A

LINK B

LINK C

ROLE

WT

ROLE

WT

ROLE

WT

spin waves
ferrimagnets
microwaves
yttrium iron garnet (YIG)
chemical vapor deposition
top seeded solution growth
crystals
thin films
magnons
magnetostatic